



UNIVERSIDAD DE CHILE  
FACULTAD DE CIENCIAS FÍSICAS Y MATEMÁTICAS  
DEPARTAMENTO DE INGENIERÍA MECÁNICA

ENRICHED ISOGEOMETRIC COLLOCATION FOR TWO-DIMENSIONAL  
TIME-HARMONIC ACOUSTICS

TESIS PARA OPTAR AL GRADO DE  
MAGÍSTER EN CIENCIAS DE LA INGENIERÍA, MENCIÓN MECÁNICA  
MEMORIA PARA OPTAR AL TÍTULO DE INGENIERO CIVIL MECÁNICO

TOMÁS BENJAMÍN AYALA LÓPEZ

PROFESORA GUÍA:  
ELENA ATROSHCHENKO

MIEMBROS DE LA COMISIÓN:  
WILLIAMS CALDERÓN MUÑOZ  
VIVIANA MERUANE NARANJO

SANTIAGO DE CHILE  
2020

RESUMEN DE LA MEMORIA PARA OPTAR  
AL TÍTULO DE MAGÍSTER EN CIENCIAS DE LA INGENIERÍA, MENCIÓN MECÁNICA  
POR: TOMÁS BENJAMÍN AYALA LÓPEZ  
FECHA: 2020  
PROF. GUÍA: ELENA ATROSHCHENKO

## ENRICHED ISOGEOMETRIC COLLOCATION FOR TWO-DIMENSIONAL TIME-HARMONIC ACOUSTICS

Nowadays, CAD and FEM softwares have a substantial impact on engineering. Both of them are powerful tools for design and analysis. The main drawback is that FEM models and CAD geometries do not match, which means that the generated CAD file needs to be translated into a suitable geometry, meshed and input into a large scale FEM code. This task takes most of the overall analysis time, and engineering designs are becoming increasingly more complex. Isogeometric Analysis (IGA) was proposed to build a direct link between CAD design and FEM analysis. The main idea of IGA is to substitute the shape functions used in FEM by the shape functions used in the CAD.

Compared to the standard IGA, a much simpler method for approximating solutions to differential equations is called isogeometric collocation (IGA-C). Its simplicity follows from the fact that the differential equation (strong form) is only enforced at a discrete set of points called collocation points, thus the evaluation and assembly is much faster since there is no need of numerical integration.

In this work, the IGA-C is paired with two types of enrichment to in order to solve 2D-problems for the Helmholtz equation: Plane Wave (PW-) and Generalized Harmonic Polynomial (GHP-) functions. A parametric study is conducted, and a detailed assessment of the performance of the method in a number of benchmark problems is provided. Three different collocation methods are tested for the non-enriched formulation, namely Greville abscissae (GA), Approximated Cauchy Galerkin (ACG) and Superconvergent (SC) points, showing that the CG scheme is the best choice in terms of overall error, convergence rate and ease of solving the linear system. Then, the influence of the number of shape functions in the original and enriched basis, location and number of collocation points and wave-number over both the convergence rate as well as the condition number of the stiffness matrix are studied.

The numerical results show that: 1) there is an improvement over the non-enriched formulation, 2) the improvement depends on the choice of the number and type of enrichment, and 3) The pollution error is not completely alleviated with the enriched formulations.



RESUMEN DE LA MEMORIA PARA OPTAR  
AL TÍTULO DE MAGÍSTER EN CIENCIAS DE LA INGENIERÍA, MENCIÓN MECÁNICA  
POR: TOMÁS BENJAMÍN AYALA LÓPEZ  
FECHA: 2020  
PROF. GUÍA: ELENA ATROSHCHENKO

## ENRICHED ISOGEOMETRIC COLLOCATION FOR TWO-DIMENSIONAL TIME-HARMONIC ACOUSTICS

En el día de hoy, softwares de CAD y FEM tienen un impacto sustantivo en la ingeniería. Ambos son herramientas altamente efectivas para el diseño y análisis. La principal desventaja es que los modelos FEM y las geometrías CAD no coinciden, lo que implica que el archivo CAD generado debe ser adaptado a una geometría adecuada, mallado y cargado en un complejo código FEM. Esta tarea consume la mayor parte del tiempo total de análisis, y la ingeniería de diseño se vuelve cada vez más complejo. El Análisis Isogeométrico (IGA) fue propuesto con el fin de establecer un vínculo entre el diseño CAD y el análisis FEM. La idea general del IGA es sustituir las funciones de forma utilizadas en FEM por las funciones de forma usadas en CAD.

En comparación con el IGA estándar, un método más simple para aproximar soluciones de ecuaciones diferenciales es el método isogeométrico de colocación (IGA-C). Su simplicidad radica en el hecho de que la ecuación diferencial (forma fuerte) es solamente impuesta en un conjunto discreto de puntos llamados puntos de colocación, así la evaluación y el ensamblaje es bastante más veloz ya que no hay necesidad de integrar numericamente.

En el presente trabajo, el IGA-C es combinado con dos tipos de enriquecimiento con el objetivo de resolver problemas asociados a la ecuación de Helmholtz: Ondas Planas (PW-) y Polinómios Harmónicos Generalizados (GHP-). Se realizó un estudio paramétrico y una evaluación detallada de la efectividad del método en varios problemas referenciales. Tres esquemas de colocación diferentes son probados sin enriquecer, Greville abscissae (GA), Cauchy Galerkin (CG) y Puntos Superconvergent (SC), de modo que el esquema CG muestra ser la mejor opción en términos de error, convergencia y facilidad al momento de resolver el sistema lineal de ecuaciones. De esta forma, la influencia del número de funciones de forma en la base original y enriquecida, posición y cantidad de puntos de colocación y número de onda sobre, tanto la tasa de convergencia como el número de condicionamiento de la matriz de rigidez son estudiados.

Los resultados numéricos muestran: 1) hay mejora con respecto a la formulación no enriquecida, 2) dicha mejora depende de la cantidad y tipo de enriquecimiento seleccionado, y 3) el error de contaminación no es completamente eliminado con la formulación enriquecida.



*Para ti, en algún lugar, en algún momento.*



# Agradecimientos

Me gustaría comenzar agradeciendo a mi guía, Prof. Elena Atroshchenko por todo el apoyo, ayuda, orientación y paciencia que me brindó tan amablemente durante este proceso. Su alto grado de dedicación, efectividad y conocimiento profesional han sido un ejemplo para mí. Trabajar con ella ha sido todo un privilegio.

También quisiera agradecer a Prof. Cosmin Anitescu por su aporte en el presente trabajo. Su experiencia fue de gran ayuda en los momentos de estancamiento y sus constructivas críticas solo agregaron valor a este proyecto.

Por otro lado quisiera expresar mis más sinceros agradecimientos a mis amigos de la sala de magister de la Universidad de Chile que estuvieron a mi lado durante este periodo: Andrés, Cristián H., Cristián S., Danilo, Gabriel, Iván, Javier, Joaquín, José, Mohammad y Patricio. Todos hicieron de esa sala un lugar muy ameno y cada día daba gusto compartirlo con ustedes. Muchas gracias por el cariño y la alegría que nunca pedí pero que tanto bien me hizo.

Finalmente, agradecer a mis padres por su amor incondicional, siempre me han apoyado en todas mis decisiones y proyectos. No creo poder dimensionar todo el esfuerzo por darnos a mis hermanas y a mí la mejor vida posible en todo aspecto. Nada sería igual sin el amor, calor y preocupación que han entregado, prometo no olvidarlo jamás.





# Contents

<b>1. Introduction</b>	<b>1</b>
1.1. Isogeometric Analysis: Galerkin (IGAFEM) and Collocation (IGA-C)	2
1.2. Partition of Unity and Generalized methods	3
1.3. Contribution	5
1.3.1. Outline of the paper	5
<b>2. Objectives</b>	<b>6</b>
2.1. General Objectives	6
2.1.1. Specific Objectives	6
2.2. Scope	6
<b>3. Methodology</b>	<b>7</b>
3.1. Literature review	7
3.2. Enriched isogeometric collocation code	7
3.3. Collocation points distribution strategies	7
3.4. Applications on wave propagation problems	8
<b>4. Theoretical background</b>	<b>9</b>
4.1. Exterior time harmonic acoustic wave propagation	9
4.2. Isogeometric Collocation	10
4.2.1. Non-Uniform Rotational B-Splines (NURBS)	10
4.2.2. Collocation Method	14
4.2.3. Collocation points and superconvergent points	15
4.3. Enriched Isogeometric Collocation for the Helmholtz Equation	17
4.3.1. Plane-Wave (PW-) enrichment	18
4.3.2. Generalized Harmonic Polynomial (GHP-) enrichment	18
4.3.3. Collocation points scheme	19
4.3.4. Enriched IGA-C on multi-patch boundary problems	19
4.3.5. Linear system solvers	19
<b>5. Numerical Results</b>	<b>21</b>
5.1. One-dimensional scattering	21
5.2. Plane-wave scattered in a square domain	24
5.3. The duct problem	27
5.4. Spinning wave propagation	52
5.5. Plane wave scattered by cylinder	58

5.6. Star geometry . . . . .	62
<b>6. Conclusion</b>	<b>64</b>
<b>Bibliography</b>	<b>64</b>
<b>Appendix</b>	<b>73</b>
<b>Appendix A. Geometry Parameterization employed in the Numerical Examples</b>	<b>73</b>

# List of Tables

4.1. NURBS curve: Control points and their respective weights . . . . .	11
4.2. NURBS surface: Polynomial orders and knot vectors for the surface shown in Figure 4.4 . . . . .	12
4.3. NURBS surface: Control points and their respective weights for the surface shown in Figure 4.4 . . . . .	13
4.4. Location of superconvergent points [2] for the second derivative on a reference element $[-1, 1]$ . . . . .	16
5.1. Duct example: Expected and observed convergence rates ( $L^2$ error norm vs DOF) for the IGA Galerkin, IGA-C GA, SC and ACG methods from Figure 5.11 . . . . .	30
A.1. Geometry Information for the duct domain . . . . .	73
A.2. Geometry Information for the duct domain . . . . .	73
A.3. Geometry Information for the annular geometry . . . . .	74
A.4. Geometry Information for the Star-shaped problem . . . . .	75

# List of Figures

4.1.	Schematic of a general acoustic problem. $\Omega$ represents the problem domain, $\Gamma_D$ , $\Gamma_N$ and $\Gamma_R$ are the Dirichlet, Neumann and Robin boundaries respectively. $\mathbf{n}$ denotes the normal vector, outer to $\Omega$ . . . . .	10
4.2.	NURBS curve in 2D: curve (blue line) and control points (red dots) . . . . .	11
4.3.	NURBS basis functions of Figure 4.2 . . . . .	12
4.4.	NURBS surface in 2D: curve (blue line) and control points (red dots) . . . . .	13
4.5.	Collocation points and knot vector: Distribution of A) Greville Abcissae, B) Approximated Cauchy-Galerkin and C) Superconvergent points for B-splines of degree $p = 2, \dots, 5$ using five elements. The blue squares represent the position of the knots and the red points represent the collocation points. . . . .	16
4.6.	Real part of plane wave enrichment functions, with $q = 3$ and $k = 10$ on a $[-1, 1] \times [-1, 1]$ domain. . . . .	18
4.7.	Real part of generalized harmonic polynomial enrichment function, with $q = 3$ and $k = 10$ on a $[-1, 1] \times [-1, 1]$ domain. . . . .	19
4.8.	Upper patches of a multi-patch mesh of a complete annulus. The blue and the green mesh represent different patches, $(\Omega^+)$ and $(\Omega^-)$ respectively, and $\alpha$ is a collocation point located at the interface between two patches. The red, blue and black dots represent the interface collocation points, the internal points and the external boundary points, respectively. . . . .	20
5.1.	One dimensional example: PW-enriched IGA-C. Relative $L^2$ error for $p = 3$ versus the number of collocation points for different wave number $k$ . . . . .	22
5.2.	One dimensional example: GHP-enriched IGA-C. Relative $L^2$ error for $k = 10$ and $p = 3$ versus the number of collocation points for different number of enrichment functions ( $q$ ). Fixed mesh of 8 elements . . . . .	23
5.3.	One dimensional example: GHP-enriched IGA-C. Relative $L^2$ error norm and condition number versus wave number $k$ for $p = 3$ , fixed mesh of 8 elements and increasing $q$ . . . . .	23
5.4.	Analytical solution of the plane-wave scattered in a square domain problem with $k = 40$ . . . . .	24
5.5.	Square scattered patch test: Relative $L^2$ error and condition number versus the number of collocation points for $p = 3$ and $k = 10$ . Fixed mesh of 1 element. Plane wave enrichment was employed in all the simulations. . . . .	25
5.6.	Square scattered patch test: Relative $L^2$ error and condition number versus the number of collocation points for $p = 3$ and $k = 50$ . Fixed mesh of 1 element. Plane wave enrichment was employed in all the simulations. . . . .	25

5.7. Square scattered patch test: Relative $L^2$ error and condition number versus the number of collocation points for $p = 3$ and $k = 100$ . Fixed mesh of 1 element. Plane wave enrichment was employed in all the simulations. . . . .	26
5.8. The duct problem: domain. . . . .	27
5.9. Analytical solution . . . . .	28
5.10. Duct patch test: PW-enriched IGA-C. Relative $L^2$ error for $p = 2$ versus the number of collocation points for different number of enrichment functions, $m = 0$ , one element in the mesh. . . . .	29
5.11. Duct example: Comparison between IGA-C using GA, SC and ACG points, and Galerkin IGA for the Relative $L^2$ error norm for B-splines of degree $p = 3, 4$ and $5$ , versus the number of degrees of freedom. $k = 10$ and $m = 2$ . . . . .	30
5.12. Duct example: Comparison between IGA-C using GA, SC and ACG points, and Galerkin IGA for the Condition number for B-splines of degree $p = 3, 4$ and $5$ , versus the number of degrees of freedom. $k = 10$ and $m = 2$ . . . . .	31
5.13. Duct example: Absolute error for a fixed mesh of 4225 elements. Comparison between Galerkin IGA, SC, GA and ACG IGA-C methods. $p = 3, k = 10$ and $m = 2$ . . . . .	32
5.14. Duct example: Comparison between IGA-C using GA, SC and ACG points, and Galerkin IGA for the Relative $L^2$ error norm for B-splines of degree $p = 3, 4$ and $5$ , versus the number of degrees of freedom. $k = 100$ and $m = 2$ . . . . .	33
5.15. Duct example: Comparison between IGA-C using GA, SC and ACG points, and Galerkin IGA for the Condition number for B-splines of degree $p = 3, 4$ and $5$ , versus the number of degrees of freedom. $k = 100$ and $m = 2$ . . . . .	33
5.16. Duct example: Comparison between IGA-C using GA, SC and ACG points, and Galerkin IGA for the Relative $L^2$ error norm for B-splines of degree $p = 3, 4$ and $5$ , versus the number of degrees of freedom. $k = 10$ and $m = 2$ . . . . .	34
5.17. Relative $L^2$ error and condition number using $p = 3$ and plane-wave enrichment for $k = 10$ and $m = 2$ . Fixed mesh of 64 elements. . . . .	35
5.18. Relative $L^2$ error and condition number using $p = 3$ and generalized harmonic polynomial enrichment (half span) for $k = 10$ and $m = 2$ . Fixed mesh of 64 elements. . . . .	35
5.19. The duct example: Relative $L^2$ error norm and Condition number study for $p = 3, k = 10$ and $m = 2$ . . . . .	36
5.20. The duct example: Relative $L^2$ error norm and Condition number study for $p = 4, k = 10$ and $m = 2$ . . . . .	36
5.21. The duct example: Relative $L^2$ error norm and Condition number study for $p = 5, k = 10$ and $m = 2$ . . . . .	37
5.22. The duct example: Relative $L^2$ error norm and Condition number study for $p = 3, k = 40$ and $m = 12$ . . . . .	38
5.23. The duct example: Relative $L^2$ error norm and Condition number study for $p = 4, k = 40$ and $m = 12$ . . . . .	38
5.24. The duct example: Relative $L^2$ error norm and Condition number study for $p = 5, k = 40$ and $m = 12$ . . . . .	39
5.25. The duct example: Relative $L^2$ error norm and Condition number study for $p = 3, k = 80$ and $m = 25$ . . . . .	40
5.26. The duct example: Relative $L^2$ error norm and Condition number study for $p = 4, k = 80$ and $m = 25$ . . . . .	40

5.27. The duct example: Relative $L^2$ error norm and Condition number study for $p = 5$ , $k = 80$ and $m = 25$ . . . . .	41
5.28. The duct example: Relative $L^2$ error norm and Condition number study for $p = 3$ , $k = 120$ and $m = 38$ . . . . .	42
5.29. The duct example: Relative $L^2$ error norm and Condition number study for $p = 4$ , $k = 120$ and $m = 38$ . . . . .	43
5.30. The duct example: Relative $L^2$ error norm and Condition number study for $p = 5$ , $k = 120$ and $m = 38$ . . . . .	43
5.31. Duct example: Wave study for a fixed mesh. Comparison between plane-wave enriched and non-enriched collocation methods. The mesh has 64 elements. $p = 3$ . . . . .	44
5.32. Duct example: Wave study for a fixed mesh. Comparison between plane-wave enriched and non-enriched collocation methods. The mesh has 64 elements. $p = 4$ . . . . .	44
5.33. Duct example: Wave study for a fixed mesh. Comparison between plane-wave enriched and non-enriched collocation methods. The mesh has 64 elements. $p = 5$ . . . . .	45
5.34. Duct example: Relative $L^2$ error norm versus the DOF density $N_\lambda$ for $k = 10$ and $k = 120$ , using $p = 4$ and different numbers of enrichment functions. . .	45
5.35. The duct example: Relative $L^2$ error norm and Condition number study for $p = 3$ , $k = 10$ and $m = 2$ and varying number of GHP-enrichment functions. . .	46
5.36. The duct example: Relative $L^2$ error norm and Condition number study for $p = 4$ , $k = 10$ and $m = 2$ and varying number of GHP-enrichment functions. . .	47
5.37. The duct example: Relative $L^2$ error norm and Condition number study for $p = 5$ , $k = 10$ and $m = 2$ and varying number of GHP-enrichment functions. . .	47
5.38. The duct example: Relative $L^2$ error norm and Condition number study for $p = 3$ , $k = 40$ and $m = 12$ , varying number of GHP-enrichment functions. . .	48
5.39. The duct example: Relative $L^2$ error norm and Condition number study for $p = 4$ , $k = 40$ and $m = 12$ , varying number of GHP-enrichment functions. . .	48
5.40. The duct example: Relative $L^2$ error norm and Condition number study for $p = 5$ , $k = 40$ and $m = 12$ , varying number of GHP-enrichment functions. . .	49
5.41. Duct example: GHP-study for a fixed mesh. Comparison between GHP-enriched and non-enriched collocation methods. The mesh has 64 elements. $p = 3$ . .	50
5.42. Duct example: GHP-study for a fixed mesh. Comparison between GHP-enriched and non-enriched collocation methods. The mesh has 64 elements. $p = 4$ . .	51
5.43. Duct example: GHP-study for a fixed mesh. Comparison between GHP-enriched and non-enriched collocation methods. The mesh has 64 elements. $p = 5$ . .	51
5.44. Spinning wave example: (a) Schematic of the exterior acoustic spinning wave propagation problem. $\Omega$ represent the problem domain, $\Gamma_1$ and $\Gamma_2$ are the Robin boundaries. The normal is denoted by $\mathbf{n}$ . (b) Multipatch mesh in physical space built with NURBS. . . . .	52
5.45. Analytical solution of the spinning wave propagation problem with $k = 40$ and $m = 30$ . . . . .	53
5.46. Spinning wave example: Relative $L^2$ error norm and condition number study for $p = 3$ , $k = 20$ and $m = 10$ for various number of PW enrichment functions. . .	53
5.47. Spinning wave example: Relative $L^2$ error norm and condition number study for $p = 3$ , $k = 20$ and $m = 22$ for various number of PW enrichment functions. . .	54

5.48. Spinning wave example: Relative $L^2$ error norm and condition number study for $p = 3$ , $k = 40$ and $m = 30$ , varying number of PW-enrichment functions.	54
5.49. Spinning wave example: Relative $L^2$ error norm and condition number study for $p = 3$ , $k = 40$ and $m = 42$ , varying number of PW-enrichment functions.	55
5.50. Spinning wave example: Relative $L^2$ error norm and condition number study for $p = 3$ , $k = 20$ and $m = 10$ . Comparison between collocation and GHP enriched collocation.	55
5.51. Spinning wave example: Relative $L^2$ error norm and condition number study for $p = 3$ , $k = 20$ and $m = 22$ . Comparison between collocation and GHP enriched collocation.	56
5.52. Spinning wave example: Relative $L^2$ error norm and condition number study for $p = 3$ , $k = 40$ and $m = 30$ , varying number of GHP-enrichment functions.	56
5.53. Spinning wave example: Relative $L^2$ error norm and condition number study for $p = 3$ , $k = 40$ and $m = 42$ , varying number of GHP-enrichment functions.	57
5.54. Analytical solution of wave scattered by a cylinder problem with $k = 40$ .	59
5.55. Cylinder scattered example: Relative $L^2$ error norm and condition number study for $p = 3$ , $k = 20$ . Comparison between collocation and PW enriched collocation.	59
5.56. Cylinder scattered example: Relative $L^2$ error norm and condition number study for $p = 3$ , $k = 40$ . Comparison between collocation and PW enriched collocation.	60
5.57. Cylinder scattered example: Relative $L^2$ error norm and condition number study for $p = 3$ , $k = 40$ . Comparison between collocation and GHP enriched collocation.	60
5.58. Cylinder scattered example: Relative $L^2$ error norm and condition number study for $p = 3$ , $k = 40$ . Comparison between collocation and GHP enriched collocation.	61
5.59. Analytical solution of sound hard star problem with $k = 20$ .	62
5.60. Star shape example, PW-enrichment: Relative $L^2$ error norm and condition number study for $p = 3$ , $k = 20$ , varying number of enrichment functions.	63
5.61. Star shape example, GHP-enrichment: Relative $L^2$ error norm and condition number study for $p = 3$ , $k = 20$ , varying number of enrichment functions.	63





# Chapter 1

## Introduction

Boundary value problems for the Helmholtz equation appear in a wide range of applications, concerned with analysis of wave propagation (e.g. time-harmonic acoustics identification of kidney stones by medical imaging [35], optimization of micro-acoustic devices ranging from hearing aids to meta-materials [1], or radar cross section reduction [10], etc). The Helmholtz equation is given by:

$$\Delta u + k^2 u = 0, \tag{1.1}$$

Nowadays, various advanced numerical methods have been developed for the Helmholtz equation, aiming to minimize numerical error at optimal computational cost. The following three main sources of numerical error can be identified:

- Discretization error, occurring when the solution (and the computational domain in finite elements methods) are approximated with shape functions
- The pollution or numerical dispersion error [7, 43, 44], associated with high wave numbers
- Boundary truncation error for problems in unbounded domains

The first two aspects will be discussed in detail in the following sections. The boundary truncation error appears in finite element and other domain-type methods in unbounded domains, when the infinite domain is truncated by a fictitious boundary, which encloses the area of interest (usually, a circle or a sphere of radius  $R$ , large enough in comparison with the characteristic size of the system,  $a$ ). Then the asymptotic behaviour of the solution is converted into the so-called Absorbing Boundary Condition (ABC) [55], [11], [70] on the fictitious boundary. Accuracy of the ABCs depends on the frequency and the size of the truncation domain (ratio  $R/a$ ). In this work, we are interested in the performance of isogeometric collocation. Therefore in all numerical examples, we excluded the boundary truncation error on the fictitious boundary by prescribing Robin boundary condition with the right-hand side derived from the exact analytical solution in the unbounded domain.

## 1.1. Isogeometric Analysis: Galerkin (IGAFEM) and Collocation (IGA-C)

While Finite Element Method (FEM) remains the most commonly used numerical method in engineering applications, isogeometric analysis (IGA) has gathered a considerable amount of attention in the computational mechanics community over the last decade. IGA was proposed by Hughes et al. [42, 26] as a next generation of FEM (IGAFEM), that aims to conciliate the gap between the Computer-Aided Design (CAD) model and the numerical analysis. With the main idea of preserving the original geometry, usually given by a Non-Uniform Rational B-Spline (NURBS) parameterization, the NURBS basis function are used instead of Lagrange polynomials in the FEM discretization. IGA has been successfully implemented in several fields, such as structural mechanics [83], shape optimization [80, 71, 39], fluid-structure interaction [13, 12, 14], shell analysis [50, 17, 40], vibrations [27, 66, 72], fracture mechanics [29, 37, 36], hyper-elastic models [18, 34, 51], electromagnetic [20, 21], Helmholtz equation [25, 81, 48], among others. A complete review of IGA and its different implementation aspects can be found in [60, 15].

Atroshchenko et al. [3] proposed GIFT as a numerical method that aims to decouple the field space from the geometry space. The field-geometry decoupling is achieved by using a more suitable basis function for the field space while keeping the exact representation of the geometry by NURBS. This method aims to employ the best basis function according to any particular characteristic of the problem (such as complex geometries or numerical singularities in the solution). The method has been successfully applied in problems of linear elasticity [3], acoustics [78], fracture mechanics of Kirchhoff-Love plates [77], and vibration of Reissner-Mindlin plates [82] among many others.

Videla et al. [78] showed the advantages of pairing PHT-splines with NURBS by GIFT in the context of time-harmonic problems. In particular, problems with local gradients given by geometrical irregularities can take advantage of the adaptive refinement given by PHT-splines, and achieve optimal convergence rates in the error norm, while keeping a coarse geometry and therefore saving computational resources.

IGA is widely used in the framework of the boundary element method (IGABEM), particularly in time-harmonics acoustics [73]. Due to the fact that the Green's functions satisfy the Sommerfeld radiation condition exactly, boundary value problems in unbounded domains can be reduced to boundary integral equations on the inner boundaries without the need to truncate the domain and introduce a boundary truncation error [23]. Note, that in BEM, governing integral equations can be solved in the Galerkin framework or imposed at a set of points, an approach known as collocation. In the BEM,  $C^0$ -continuous shape functions could be sufficient for collocation. However, in the context of partial differential equations, global continuity of shape functions has a significant effect on convergence and stability of collocation. NURBS and other types of splines possess features of degree elevation with assuring desired global continuity within a patch, which makes them attractive for the so-called isogeometric collocation (IGA-C).

Recently, a discontinuous IGABEM method applied to 3D acoustics was proposed by Sun et al.[76]. They compare a continuous and a discontinuous 3D IGABEM, which is formu-

lated using discontinuous elements and a collocation scheme, showing the potential of the discontinuous method to model problems with complex geometries arising from CAD models.

IGA-C was initially proposed by Auricchio et al. [5, 4]. Lin et al. [53] studied the consistency and convergence properties of IGA-C for the 1-D formulation, while Schillinger et al. [69] compared isogeometric collocation with both Lagrange FEM and IGAFEM formulation, showing that while IGAFEM outperforms IGA-C in terms of accuracy per DOF, IGA-C is more efficient than IGAFEM in terms of accuracy per unit of computational time.

IGA-C has been employed in various applications, such as two-dimensional elastostatic and explicit dynamic problems [4], Timoshenko beams [28] and rods [6], Bernoulli-Euler beams and Kirchhoff-Love plates [67], and Reissner-Mindlin plates [49]. Moreover, De Lorenzis et al. [?] proposed a hybrid collocation-Galerkin formulation to treat Neumann and contact boundary conditions.

Schillinger et al. [68] proposed an hybrid collocation-Galerkin formulation for phase-field fracture models. This was further developed by Jia et al. [45], where an adaptive isogeometric collocation method using PHT-splines was proposed, leading to optimal convergence rates for both uniform and adaptive refinement and for different 2D and 3D elasticity benchmark problems. Nguyen-Thanh et al. [61] formulated an adaptive isogeometric meshfree collocation (IGAM-C) method for the two-dimensional (2D) elasticity and frictional contact problems, with better results compared to a uniform refinement.

A topic of particular interest in the IGA-C method is selection of the collocation points. The standard choice is the Greville abscissae points [46], but it is well known that the convergence rate reported with Greville abscissae is sub-optimal, i.e. of order  $p$  and  $p - 1$  in the  $L^2$  error norm for odd and even degree NURBS, respectively [69].

Different studies have been performed in order to improve the convergence rate of the IGA-C. Anitescu et al. [2] studied the use of superconvergent (SC) points, leading to convergence rates of  $p + 1$  and  $p$  in the  $L^2$  error norm for odd and even degrees, respectively, at the cost of solving an over-determined linear system resulting from a non-square stiffness matrix. Gomez and De Lorenzis [38] proposed a set of collocation points that are related to the Galerkin solution of the system, which in general is unknown. A numerical approximation of these points is in fact a subset of the superconvergent points from [2], achieving convergence rates of  $p$  in the  $L^2$  error norm for both even and odd degrees. In this work, we will refer to the collocation points from [38] as *Approximated Cauchy Galerkin (AGC)* points. Montardini et al. [58] proposed a different choice of subset of superconvergent points from [2] (called clustered superconvergent points (C-CSP), which correspond to two symmetric superconvergent points from [2] in every other element). This choice also leads to the same convergence rate as in [2] but avoids having more equations than the degrees of freedom. Note, that for even  $p$ , the collocation points from [38] and [58] coincide.

## 1.2. Partition of Unity and Generalized methods

In acoustics and wave propagation analysis, the error of the numerical solution consists of the discretization error and the pollution error (see a detailed discussion in [78]), and as the

wave number  $k$  grows, the pollution error becomes dominant.

Other approach to reduce the pollution error is to employ High-order Finite Element. High-order FE formulations applied to the Helmholtz equation [52, 22, 24, 47] have proved to be more accurate and effective in coping with the pollution error than low order methods, but at the expenses of increasing condition numbers and higher computation cost when the degree  $p$  increases.

Another approaches to overcome the pollution error consists in modifying the basis functions in a way that captures the highly oscillatory behaviour of the solutions.

The Partition of Unity (PU) enrichment, initially proposed by Melenk and Babuška [56, 8], consists in enhancing the original set of basis functions with a new set, derived from *a priori* knowledge of main features of the governing partial differential equation and its analytical solution. In the case of the Helmholtz equation, the general solution takes the form of either the Bessel functions or plane waves. The results of these initial studies show that the PU enrichment of FEM has advantages in terms of the error vs the number of Degrees of freedom (DOFs) in comparison with standard FEM. In these early studies, certain drawbacks of the PUFEM, such as high condition number of the stiffness matrix, were also documented. A detailed analysis of performance of the PUFEM in terms of the condition number, geometry description and presence of multiple scatters is given in [57].

Subsequently, the Generalized Finite element method (GFEM) [74, 75] was proposed. GFEM, PUFEM and XFEM refer to the same idea of enrichment and are often used interchangeably. However, some authors distinguish GFEM as the method that employs solution approximation consisting of both, the original and enriched bases, contrary to PUFEM, which only uses the enriched basis. The data in the literature show that the GFEM and PUFEM produce similar results in the context of the Helmholtz equation, namely, advantages in terms of the error vs the number of DOFs at the price of high condition number are reported. The optimal relation between the mesh size, degree of polynomial shape function and number of plane-wave functions is still an open question. A review of different enrichment methods applied to the Helmholtz equation can be found in [41].

Different choices of enrichment applied to the Helmholtz equation are available, such as the plane-wave functions, wave-band functions and the Generalized Harmonic Polynomial. For instance, Strouboulis et al. [75] studied the effect of the enrichment set employed in the GFEM applied to Helmholtz equation, showing that all of them deliver similar results in terms of error norm versus DOFs and that the selection of the local bases should thus be determined by other factors such as the ease of the implementation or the computational cost.

Those enriched formulations have been also implemented in conjunction with the BEM [19], IGABEM [62, 63] and IGAFEM [30, 31] (also refereed as eXtended BEM (X-BEM), eXtended IGABEM (X-IGABEM) and Partition of Unity IGAFEM (PUIGA) respectively), showing in all cases certain improvements over the non-enriched methods.

One particular drawback that enriched formulations have is related to numerical integration of the enriched functions. Enriched formulations require the numerical integration of

highly oscillatory functions, which is usually done using high-order Gauss quadrature. Still, as it has been reported by [33, 9], using high-order Gauss quadrature does not deliver accurate results for high wave numbers. For instance, Banerjee and Sukumar [9] proposed an exact integration scheme for linear plane-wave enriched FEM that delivers exact integration, and it is independent of the wave number.

Note, that in the case of the Helmholtz equation, the enrichment is applied globally. In other applications, such as for example, problems with fracture and inclusions, the enrichment of the solution is used only in the vicinity of the area of interest, i.e. X-FEM [59], X-BEM [19], and their isogeometric versions, as developed for example in X-IGAFEM [16], X-IGABEM [64]. Other wave-related areas, such as time-dependent problems of electromagnetic wave [32] and 3D elastic wave modelling [54], have been studied under the PUFEM formulation.

To the authors' knowledge, no articles are available which combine the IGA-C and the enrichment for the Helmholtz equation.

### 1.3. Contribution

In this work, we pair the isogeometric collocation (IGA-C) with the Generalized enrichment of two types, plane waves and harmonic functions, to solve 2D-problems for the Helmholtz equation. We conduct a parametric study and provide a detailed assessment of the performance of the method in a number of benchmark problems. We investigate the influence of the number of shape functions in the original and enriched bases and number and location of collocation points on the convergence rate and the condition number of the stiffness matrix.

The numerical results for the IGA-C and the enriched IGA-C are obtained under the formulation of the Geometry Independent Field approximation (GIFT) [3]. In our formulation, both the geometry and the field basis are given by NURBS, but we keep the geometry unchanged, while  $h$ - and  $p$ - refinement is only applied to the field basis.

#### 1.3.1. Outline of the paper

The outline of the paper is as follows: The mathematical formulation of the Helmholtz equation is given in Section 4.1. Section 4.2 is devoted to NURBS, the theoretical framework of collocation method and description of the collocation schemes, while Section 4.3 deals with enriched formulations for the Helmholtz equation in the context of isogeometric collocation. Numerical examples are presented in section 5, while the main results are summarized in section 6.

# Chapter 2

## Objectives

The objectives and scope for the thesis work are presented as follows.

### 2.1. General Objectives

Develop and implement an two-dimensional enriched isogeometric collocation method scheme to study its performance in time-harmonic acoustic equations.

#### 2.1.1. Specific Objectives

- Develop a standard IGA-C code for two-dimensional Helmholtz equation problems
- Develop an enriched IGA-C code for two-dimensional Helmholtz equation problems.
- Analyze and compare the numerical results in terms of convergence plots for the  $L^2$  error norm.

### 2.2. Scope

This thesis work is intended to propose and validate an isogeometric collocation scheme using enriched NURBS basis functions. This proposed work will only be tested on benchmark problems, and the performance results are properly presented in convergence plots, figures and tables.

# Chapter 3

## Methodology

In order to successfully fulfill the objectives of the present thesis work, the following steps are implemented:

### 3.1. Literature review

Over the last twenty years, a vast volume of literature related to both FEM and XFEM has been published. Moreover, since Hughes and its team proposed IGA, several ideas and techniques from FEM have been revisited to study the gains and drawbacks of its applications on IGA like collocation schemes. Therefore, a literature review of the principal topics that cover this thesis must be performed, which should include: Isogeometric Analysis, Collocation Methods, Partition of Unity Finite Element Methods among other subjects.

### 3.2. Enriched isogeometric collocation code

According to the literature review, and based on the open-source codes available online, a Matlab® routine capable of performing IGA-C using enriched NURBS basis will be implemented. This implementation will be oriented to wave propagation and two different enrichments will be used, plane wave functions and generalized harmonic polynomials. The numerical implementation will be based on the open-source package IGAPACK, available at <https://github.com/canitesc/IGAPack>.

### 3.3. Collocation points distribution strategies

A specific distribution of collocation points needs to be defined in order to implement the IGA-C and then applied the enriched basis. Three different types of points distribution will be compared using the standard IGA-C: Greville Abcissae, Cauchy-Galerkin and Superconvergent. Thus the most suitable will be selected for the enriched IGA-C implementation.

Since the enriched method requires more degrees of freedom than the standard method, new points will be inserted in the previously selected distribution. In order to define these



new collocation points, several configuration for both types of enrichments will be compared in terms of  $L^2$  error norm.

### 3.4. Applications on wave propagation problems

The area of application of the proposed formulation will be two dimensional time-harmonic wave propagation. It is well known that this kind of problem present challenges to any numerical domain method, such as the pollution error that occurs when solving the equation with a high wave-number  $k$ , or the correct treatment of boundary conditions when moving from unbounded domain to bounded domains. Hence, enriched IGA-C will be studied in this kind of problems in order to know if it can improve the solution.

# Chapter 4

## Theoretical background

### 4.1. Exterior time harmonic acoustic wave propagation

We consider the exterior acoustic problem shown in Figure 4.1. The acoustic domain is filled with a compressible ideal fluid of sound speed  $c$  and density  $\rho$ . The acoustic pressure in a homogeneous media is modelled by the wave equation

$$\Delta P - \frac{1}{c^2} \frac{\partial^2 P}{\partial t^2} = 0. \quad (4.1)$$

where  $P = P(\mathbf{x}, t)$  is the acoustic pressure,  $\mathbf{x} \in \Omega$  is the physical space and  $t \in [0, \infty]$  is the time. Since we are interested in the time harmonic case and, assuming that all waves are steady-state with circular frequency  $\omega$ , the pressure field  $P(\mathbf{x}, t)$  can be written as

$$P(\mathbf{x}, t) = u(\mathbf{x}) \exp(-i\omega t). \quad (4.2)$$

Substituting eqn.(4.2) into eqn.(4.1), we obtain the Helmholtz equation

$$\Delta u + k^2 u = 0, \quad (4.3)$$

where  $k = \omega/c$  is the wave number.

The general acoustic problem in domain  $\Omega$  with boundary  $\Gamma = \partial\Omega$  (see Figure 4.1) can be stated as

*Find  $u$  such that*

$$\Delta u + k^2 u = 0 \quad \text{in } \Omega \quad (4.4)$$

$$u = g, \quad \text{on } \Gamma_D \quad (4.5)$$

$$\nabla u \cdot \mathbf{n} = h \quad \text{on } \Gamma_N \quad (4.6)$$

$$\frac{\partial u}{\partial n} - iku = f \quad \text{on } \Gamma_R, \quad (4.7)$$

where  $g$ ,  $h$ ,  $f$  are the prescribed Dirichlet, Neumann and Robin boundary conditions on their corresponding parts of the boundary, i.e.  $\Gamma_D$ ,  $\Gamma_N$  and  $\Gamma_R$  respectively. Note, that  $\Gamma_D \cup \Gamma_N \cup \Gamma_R = \Gamma$  and  $\Gamma_D \cap \Gamma_N \cap \Gamma_R = \emptyset$ .

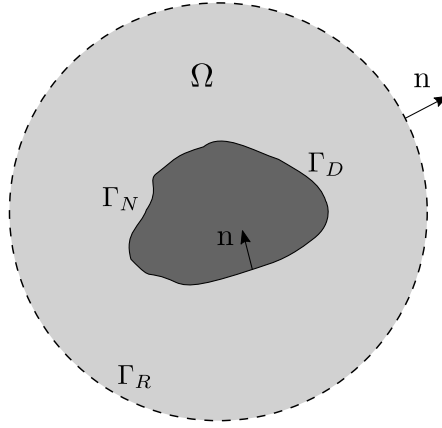


Figure 4.1: Schematic of a general acoustic problem.  $\Omega$  represents the problem domain,  $\Gamma_D$ ,  $\Gamma_N$  and  $\Gamma_R$  are the Dirichlet, Neumann and Robin boundaries respectively.  $\mathbf{n}$  denotes the normal vector, outer to  $\Omega$ .

In the case of an unbounded domain, we assume that there is no reflection from infinity. This condition is given by eqn 4.8, and is known as the Sommerfeld radiation condition:

$$\frac{\partial u}{\partial n} - iku = o(r^{1/2}) \text{ as } r \rightarrow \infty \quad (4.8)$$

When truncation boundary is introduced, this condition is approximated by an operator:

$$\frac{\partial u}{\partial n} - iku = f, \text{ on } \Gamma_R \quad (4.9)$$

where  $f$  is unknown, but can be calculated with the analytical solution.

In this work, first and second-order absorbing boundary conditions, as proposed by Bayliss et al., are employed to take into account the aforementioned Sommerfeld radiation condition.

## 4.2. Isogeometric Collocation

### 4.2.1. Non-Uniform Rotational B-Splines (NURBS)

A knot vector is a set of non-decreasing real numbers that represent the coordinates in the parametric space, i.e.

$$\Xi = \{\xi_1, \xi_2, \dots, \xi_{n+p+1}\}, \quad (4.10)$$

where  $p$  is the order of the spline and  $n$  is the number of basis functions.

B-Splines basis functions for  $p = 0$  are defined as piecewise constants:

$$N_{i,0}(\xi) = \begin{cases} 1, & \text{if } \xi_i \leq \xi < \xi_{i+1} \\ 0, & \text{otherwise} \end{cases} \quad (4.11)$$

then, for  $p \geq 1$  B-Splines are defined recursively by the following formula

$$N_{i,p}(\xi) = \frac{\xi - \xi_i}{\xi_{i+p} - \xi_i} N_{i,p-1}(\xi) + \frac{\xi_{i+p+1} - \xi}{\xi_{i+p+1} - \xi_{i+1}} N_{i+1,p-1}(\xi), \quad (4.12)$$

Non-Uniform Rational B-Splines (NURBS) are subsequently defined as

$$R_i^p(\xi) = \frac{N_{i,p}(\xi)w_i}{\sum_{i=1}^n N_{i,p}(\xi)w_i}, \quad (4.13)$$

where  $w_i$  is the weight corresponding to the  $i$ -th B-spline function.

Figure 4.2 shows an example of a 2D cubic NURBS curve with their control points. This curve is created with the following knot vector:  $\Xi = \{0, 0, 0, 0, 0, 4, 0, 5, 0, 6, 1, 1, 1, 1\}$ . The control points are given on Table 4.1, and the respective basis functions are shown on Figure 4.3

Control Points $P_i$		
$x$	$y$	$w$
-4	-4	1
-4	0	$\sqrt{2}/2$
0	0	1
0	4	$\sqrt{2}/2$
4	4	1
4	0	1
2	-4	1

Table 4.1: NURBS curve: Control points and their respective weights

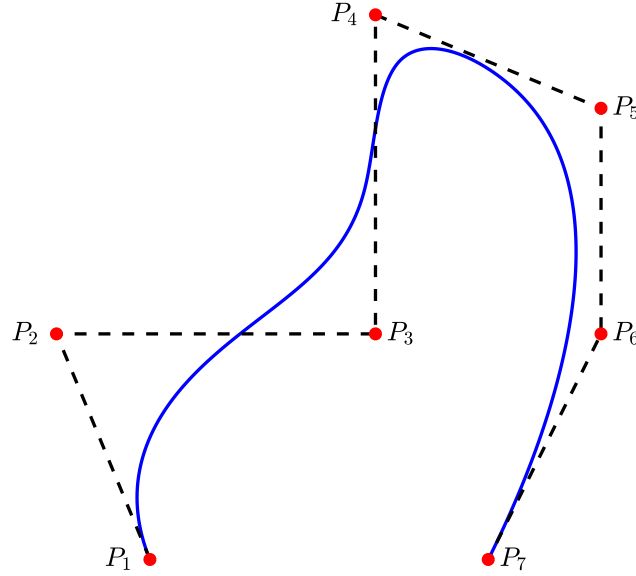


Figure 4.2: NURBS curve in 2D: curve (blue line) and control points (red dots)

In 2D, NURBS are defined as the tensor product between two one-dimensional NURBS, i.e.

$$R_{i,j}^{p,q}(\xi, \eta) = \frac{N_{i,p}(\xi)M_{j,q}(\eta)w_{i,j}}{\sum_{i=1}^n \sum_{j=1}^m N_{i,p}(\xi)M_{j,q}(\eta)w_{i,j}}, \quad (4.14)$$

where the second set of B-Splines  $M_{j,q}(\eta)$  of degree  $q$  is defined on knot vector  $\Xi_2 = \{\eta_1, \eta_2, \dots, \eta_{m+q+1}\}$  (with  $m$  being the number of basis functions  $M_{j,q}(\eta)$ ).

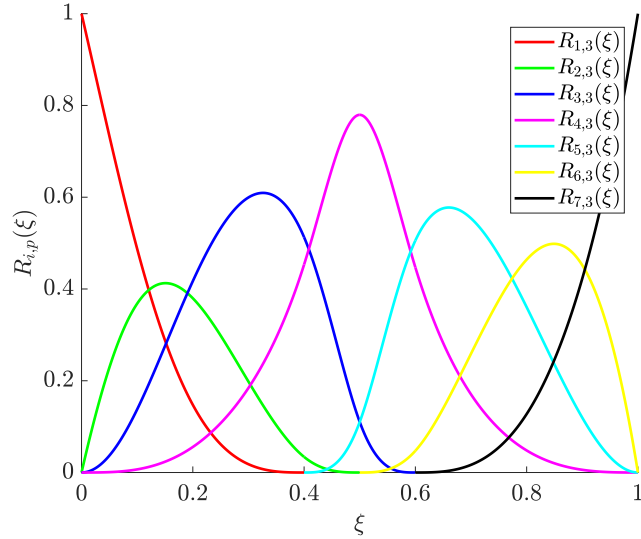


Figure 4.3: NURBS basis functions of Figure 4.2

The mapping between the parametric space  $\hat{\Omega} = [\xi_1, \xi_{n+p+1}] \times [\eta_1, \eta_{m+q+1}]$  and the physical space  $\Omega$  is given by

$$\mathbf{F}(\xi, \eta) = \sum_{i=1}^n \sum_{j=1}^m R_{i,j}^{p,q}(\xi, \eta) \mathbf{B}_{i,j} = [x, y]^T, \quad (4.15)$$

where  $\mathbf{B}_{i,j}$  are the control points defined in the physical space. In what follows we use the following notation

$$R_I(\xi, \eta) = R_{i,j}^{p,q}(\xi, \eta) \quad (4.16)$$

with multi-index  $I$ , that combines  $(i, j)$  and takes values  $I = 1, \dots, n \times m$ .

Figure 4.4 shows an example of a 2D linear-quadratic NURBS surface. The polynomial order and knot vectors are given on Table 4.2, while the control points are shown on Table 4.3.

Direction	Order	Knot Vector
$\xi$	$p = 1$	$\Xi = \{0, 0, 1, 1\}$ .
$\eta$	$q = 2$	$\Xi = \{0, 0, 0, 1, 1, 1\}$

Table 4.2: NURBS surface: Polynomial orders and knot vectors for the surface shown in Figure 4.4

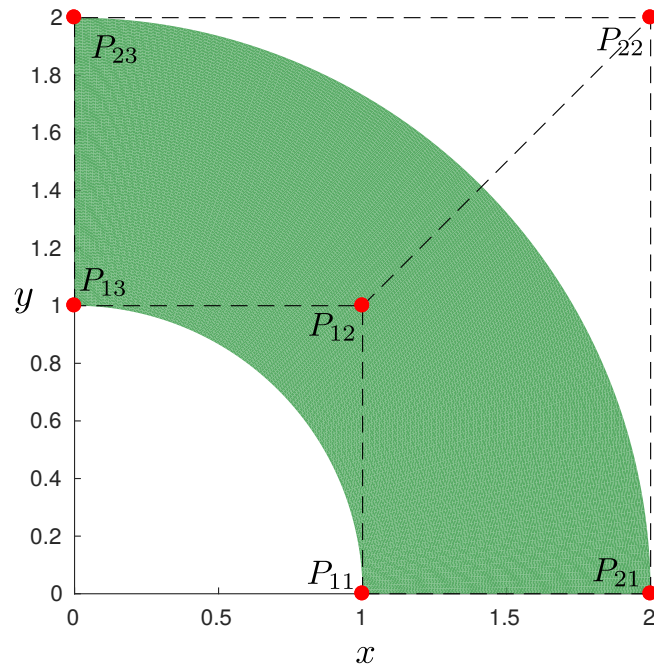


Figure 4.4: NURBS surface in 2D: curve (blue line) and control points (red dots)

Control Points $P_{ij}$		
$x$	$y$	$w$
1	0	1
$\sqrt{2}/2$	$\sqrt{2}/2$	$\sqrt{2}/2$
0	1	1
2	0	1
$\sqrt{2}$	$\sqrt{2}$	$\sqrt{2}/2$
0	2	1

Table 4.3: NURBS surface: Control points and their respective weights for the surface shown in Figure 4.4

The B-spline basis functions have the following properties:

- Linear independence.
- Partition of unity.
- Compact support for each  $N_{i,p}$  in the interval  $[u_i, u_{i+p+1}]$ .
- Non-negative basis functions.

Since NURBS are transformations of the B-spline basis functions they inherit their main properties and obtain more. Some of them include:

- Partition of unity.
- Continuity and support of B-spline.
- Affine transformations in a physical space are achieved by applying them to the control points. This means NURBS have the property of affine covariance.
- If the weights of all control points are equal, NURBS become B-splines.

For computational details regarding B-splines and NURBS, the reader is referred to [65].

#### 4.2.2. Collocation Method

We consider the strong form of a boundary value problem, which is written as

$$\mathcal{L}u = f, \quad \text{in } \Omega \quad (4.17)$$

$$\mathcal{G}u = g, \quad \text{on } \Gamma \quad (4.18)$$

where  $\mathcal{L}u = \Delta u + k^2 u$  and  $\mathcal{G}u$  corresponds to a combination of Dirichlet, Neumann and Robin boundary conditions. The solution  $u^h$  is approximated as

$$u^h(x, y) = \sum_{I=1}^{n \times m} \phi_I (R_I \circ \mathbf{F}^{-1})(x, y), \quad (4.19)$$

where  $\phi_I$  are unknown control variables, and  $R_I \circ \mathbf{F}^{-1}$  denotes a function composition between the inverse mapping of the geometry  $\mathbf{F}^{-1}$ , and the NURBS basis functions  $R_I$ .

The main idea of collocation is to select a set of points  $\boldsymbol{\alpha}_J \in \Omega \cup \Gamma$ , where the differential equation and the boundary conditions are satisfied by an approximate solution  $u^h$ . In IGA-C, collocation points are first defined in the parametric space ( $\hat{\boldsymbol{\alpha}}_J \in \hat{\Omega}$ ) and then mapped to physical space by

$$\boldsymbol{\alpha}_J = \mathbf{F}(\hat{\boldsymbol{\alpha}}_J). \quad (4.20)$$

Therefore, the collocation solution  $u^h$  is required to satisfy:

$$\mathcal{L}u^h(\boldsymbol{\alpha}_J) = f(\boldsymbol{\alpha}_J), \quad \text{in } \Omega \quad (4.21)$$

$$\mathcal{G}u^h(\boldsymbol{\alpha}_J) = g(\boldsymbol{\alpha}_J), \quad \text{on } \Gamma \quad (4.22)$$

Equations (4.29) and (4.30) are subsequently converted into a linear system

$$\mathbf{M}\mathbf{X} = \mathbf{F}, \quad (4.23)$$

which is solved for the vector of unknown control variables  $\mathbf{X} = \{\phi_1, \phi_2, \dots, \phi_{n \times m}\}$ .

### 4.2.3. Collocation points and superconvergent points

The choice of the collocation points is fundamental to ensure the convergence of the IGA-C. The most common choice is the Greville abscissae points  $\hat{\alpha}_{GA}$ , which are computed based on the knot vector. The formula for the Greville abscissae (GA points) points for a NURBS curve is given by [46]

$$\hat{\alpha}_{GA_i} = \frac{1}{p} \sum_{j=i}^{i+p+1} \xi_j, \quad (4.24)$$

where  $p$  is the degree of the B-spline and  $\xi_i$  are the knots.

The GA points lead to convergence rates of  $p - 1$  and  $p$  for odd and even degrees of B-splines, respectively, in the  $L^2$  error norm. Despite the sub-optimal convergence rate, GA points are the most popular choice of collocation points in the literature on IGA-C.

Various studies aimed to improve the convergence rate of the IGA-C method. For instance, Anitescu et al. [2] proposed the use of the superconvergent points (SC points). Superconvergent points arise from the works of Zienkiewicz and Zhu [84, 85], based on the idea that, in the context of FEM, there exist some points  $x^*$  in domain  $\Omega$  in which the numerical solution  $u_h$  is more accurate in comparison with any other set of points in  $\Omega$ . Following the same idea, in [2] these superconvergent points were computed for B-splines of  $C^{p-1}$  continuity in a reference element  $[-1, 1]$  and subsequently mapped to each knot span (Table 4.4). These superconvergent points lead to convergence rates of  $p + 1$  and  $p$  for odd and even B-splines degrees in the  $L^2$  error norm. However, the main drawback of the method is that the number of SC points exceeds the number of DOFs, therefore this formulation leads to a non-square system of equations that must be solved in the least-square sense. As we show in our numerical examples, this is particularly detrimental to the precision and its ability to overcome the pollution error.

As shown in Gomez and De Lorenzis [38], there exists a set of collocation points that produces exactly the Galerkin solution when they are evaluated in eq.(4.27). These points,  $\boldsymbol{\tau}_j$  are called Cauchy-Galerkin points (CG points), and they depend on the unknown solution. In their work, Gomez and De Lorenzis derived a numerical approximation of these points that coincides with the SC points proposed by Anitescu et al. [2], and selected a subset of these points that matches the number of B-splines basis functions and contains at least one point per basis support (referred as Approximated Cauchy-Galerkin (ACG) points in this work). ACG points deliver a convergence rate of  $p$  for both odd and even B-splines in the  $L^2$  error norm. The main advantage of the ACG set of collocation points is that it improves the convergence rate compared to the GA set while keeping a ratio one to one with the number of collocation points and the number of control points (or DOFs), which makes the solving



Table 4.4: Location of superconvergent points [2] for the second derivative on a reference element  $[-1, 1]$ .

Degree	SC points - second derivative
$p = 2$	0
$p = 3$	$\pm 1/\sqrt{3}$
$p = 4$	$-1, 0, 1$
$p = 5$	$\pm\sqrt{225 - 30\sqrt{30}}/15$
$p = 6$	$-1, 0, 1$
$p = 7$	$\pm 0,5049185675126533$

process faster and less expensive. See Listing 1 in [38] for a Matlab<sup>®</sup> code that produces the ACG points.

Recently, Montardini et al. [58] proposed a set of collocation points that combines both the ideas of [2] and [38]. This set, called Collocation on clustered superconvergent points (C-CSP) takes two symmetric superconvergent points from [2] in every other element. This approach achieves the same convergence rates as [2], but the ratio between collocation points and DOF is one to one, yielding a square system of equations.

Figure 4.5 shows the position of the different collocation point sets discussed for B-splines of degree  $p = 2, 3, 4, 5$  using open knots vector of five elements.

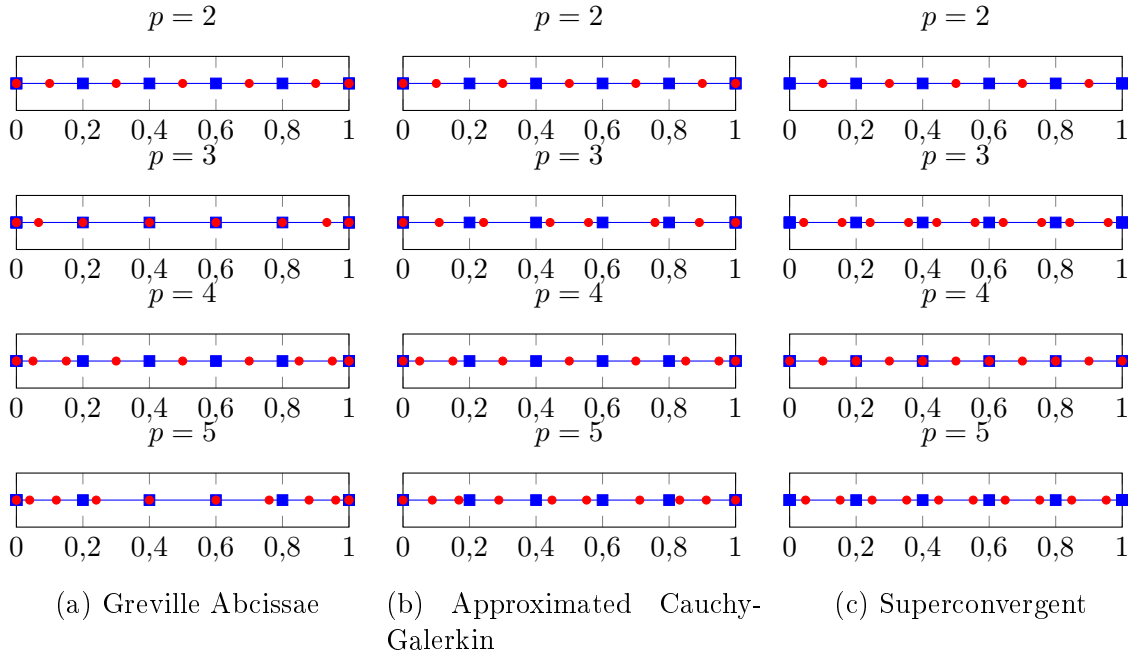


Figure 4.5: Collocation points and knot vector: Distribution of A) Greville Abcissae, B) Approximated Cauchy-Galerkin and C) Superconvergent points for B-splines of degree  $p = 2, \dots, 5$  using five elements. The blue squares represent the position of the knots and the red points represent the collocation points.

In this work, GA, SC and ACG collocation points have been tested for both the IGA-C

and the enriched IGA-C methods. As we will discuss in the results section, the numerical simulations show that IGA-C with SC points is superior in terms of the convergence rate, but seems to start achieving its asymptotic behaviour later than GA and ACG (in terms of DOFs), which makes it a sub-optimal choice for the Helmholtz equation with high  $k$ . We consider the strong form of a boundary value problem, which is written as

$$\mathcal{L}u = f, \quad \text{in } \Omega \quad (4.25)$$

$$\mathcal{G}u = g, \quad \text{on } \Gamma \quad (4.26)$$

where  $\mathcal{L}u = \Delta u + k^2 u$  and  $\mathcal{G}u$  correspond to a combination of Dirichlet, Neumann and Robin boundary conditions. The solution  $u^h$  is approximated as

$$u^h(x, y) = \sum_{I=1}^{n \times m} \phi_I (R_I \circ \mathbf{F}^{-1})(x, y), \quad (4.27)$$

where  $\phi_I$  are unknown control variables.

The main idea of collocation is to select a set of points  $\boldsymbol{\alpha}_J \in \Omega \cup \Gamma$ , where the differential equation and the boundary conditions are satisfied by an approximate solution  $u^h$ . In IGA-C, collocation points are first defined in the parametric space ( $\hat{\boldsymbol{\alpha}}_J \in \hat{\Omega}$ ) and then mapped to physical space by

$$\boldsymbol{\alpha}_J = \mathbf{F}(\hat{\boldsymbol{\alpha}}_J). \quad (4.28)$$

Therefore, the collocation solution  $u^h$  is required to satisfy:

$$\mathcal{L}u^h(\boldsymbol{\alpha}_J) = f(\boldsymbol{\alpha}_J), \quad \text{in } \Omega \quad (4.29)$$

$$\mathcal{G}u^h(\boldsymbol{\alpha}_J) = g(\boldsymbol{\alpha}_J), \quad \text{on } \Gamma \quad (4.30)$$

Equations (4.29) and (4.30) are subsequently converted into a linear system

$$\mathbf{M}\mathbf{X} = \mathbf{F}, \quad (4.31)$$

which is solved for the vector of unknown control variables  $\mathbf{X} = \{\phi_1, \phi_2, \dots, \phi_{n \times m}\}$ .

### 4.3. Enriched Isogeometric Collocation for the Helmholtz Equation

In eq.(4.27), we stated that for a standard isogeometric collocation method, the solution is approximated as a linear combination of the NURBS basis function. In the enriched IGA-C method, a new set of basis functions is employed, which consist in a combination between the NURBS basis functions  $\{R_I\}_{I=1, \dots, n \times m}$  and a set  $\{\Psi_j\}_{j=1, \dots, q}$  of enrichment functions. Thus, the numerical solution can be approximated as

$$u^h(\xi, \eta) = \sum_{I=1}^{n \times m} R_I \phi_I + \sum_{K=1}^{n \times m} \sum_{j=1}^q R_K \Psi_j \psi_{Kj}, \quad (4.32)$$

where  $R_I$  is the standard NURBS basis function associated with the control variable  $\phi_I$ ,  $\Psi_j$  is the enrichment function,  $q$  is the total number of enrichment functions, and  $\psi_{Kj}$  are additional degrees of freedom corresponding to the enriched basis function  $R_K\Psi_j$ .

In this study two sets of enrichment functions are considered, namely the plane-wave (PW-) and the Generalized Harmonic Polynomial (GHP-) enrichment:

### 4.3.1. Plane-Wave (PW-) enrichment

The first set of enrichment functions is a system of plane-waves that propagate propagate in different directions. The corresponding span is given by:

$$W(q) = \text{span} \left\{ \exp(ik(x \cos \theta_j + y \sin \theta_j)) \mid \theta_j = 2\pi \frac{(j-1)}{q} + \theta_0, j = 1, \dots, q \right\}, \quad (4.33)$$

where  $q$  is the number of propagation angles and, therefore, the number of enrichment functions and  $\theta_0$  is the starting orientation angle. For simplicity, in this study, we have considered  $\theta_0 = 0$  unless otherwise stated. Figure 4.6 shows an example of the real part of the plane wave enrichment functions with  $q = 3$  and  $k = 10$ .

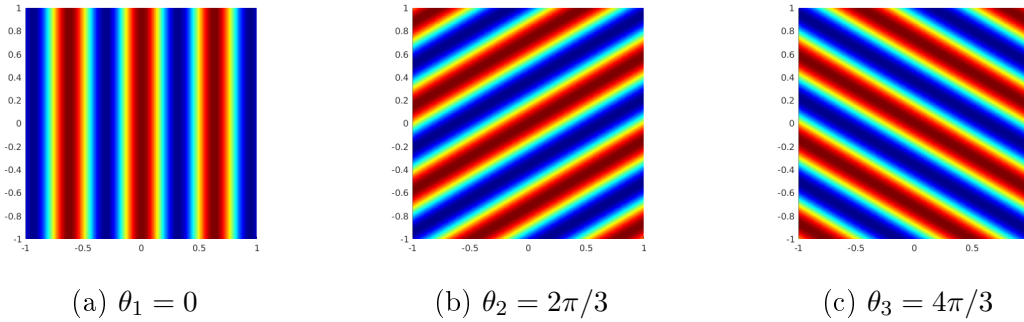


Figure 4.6: Real part of plane wave enrichment functions, with  $q = 3$  and  $k = 10$  on a  $[-1, 1] \times [-1, 1]$  domain.

### 4.3.2. Generalized Harmonic Polynomial (GHP-) enrichment

The second set of enrichment functions, first presented in [74], corresponds to the Vekua functions, also known as the generalized harmonic polynomials. The corresponding span is given by:

$$V(q) = \text{span} \{ \exp(ij\theta k) J_j(kr) \mid j = 0, \dots, q-1 \}, \quad (4.34)$$

in polar coordinates

$$\theta = \arctan\left(\frac{y}{x}\right), \quad r = \sqrt{x^2 + y^2}. \quad (4.35)$$

The number of enrichment functions in this case is  $q = p + 1$ , where  $p$  is the degree of the NURBS basis. Figure 4.7 shows an example of the real part of the generalized harmonic polynomial enrichment functions with  $q = 3$  ( $p = 2$ ) and  $k = 10$ .

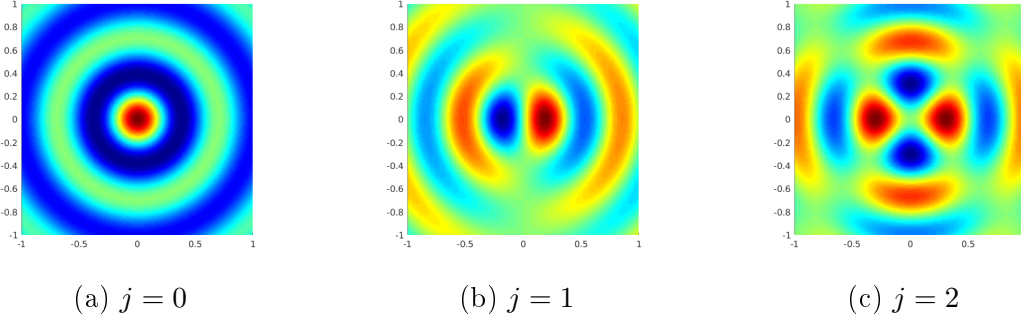


Figure 4.7: Real part of generalized harmonic polynomial enrichment function, with  $q = 3$  and  $k = 10$  on a  $[-1, 1] \times [-1, 1]$  domain.

### 4.3.3. Collocation points scheme

The enriched IGA-C requires more degrees of freedom compared to the standard IGA-C. Therefore additional collocation points need to be added in order to solve the new linear equation system. It is the purpose of this paper to find a suitable way to add these additional points. The strategy that we employed in this study is to progressively add collocation points equidistantly between the original set of collocation points, and find a suitable general configuration. In subsection 5.3, we employed a duct scattered by plane wave example in order to find the mentioned configuration.

### 4.3.4. Enriched IGA-C on multi-patch boundary problems

In the examples where multiple patches are employed, two conditions need to be satisfied on the patches interfaces in order to assure continuity of the numerical solution, namely

$$u_h|_{\Omega^+}(\alpha) = u_h|_{\Omega^-}(\alpha), \quad (4.36)$$

$$\frac{\partial u_h}{\partial n} \Big|_{\Omega^+}(\alpha) = - \frac{\partial u_h}{\partial n} \Big|_{\Omega^-}(\alpha), \quad (4.37)$$

In these equations,  $\alpha$  is a collocation point on the interface between  $\Omega^+$  and  $\Omega^-$  as shown in Figure 4.8. Note, that in this study we limited attention to conforming patches, with coincident collocation points on the interfaces. A more detailed analysis regarding patch coupling in the context of IGA-C is conducted in [4].

In the case of the enriched IGA-C, generally we use more collocation points than degrees of freedom, and therefore the continuity of the solution across the patches' boundaries was enforced by including a penalty factor in eqs. (4.36) and (4.37). The value of this penalty factor was empirically chosen as  $10^6$ .

### 4.3.5. Linear system solvers

In the context of computational acoustics it is worth mentioning that a high number of degrees of freedom per wavelength leads to a significantly high condition number of the stiffness matrix. The numerical implementation of this method was done in Matlab. We found

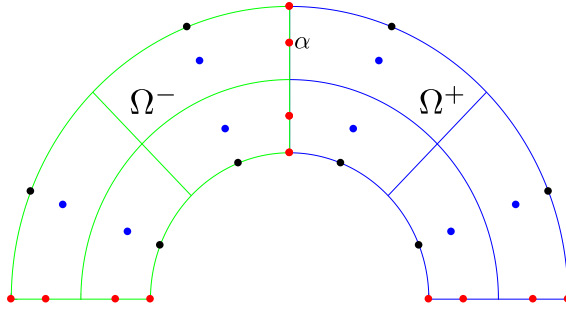


Figure 4.8: Upper patches of a multi-patch mesh of a complete annulus. The blue and the green mesh represent different patches,  $(\Omega^+)$  and  $(\Omega^-)$  respectively, and  $\alpha$  is a collocation point located at the interface between two patches. The red, blue and black dots represent the interface collocation points, the internal points and the external boundary points, respectively.

direct solver most efficient for the matrices in this study. The matrix inversion is carried out using the backslash operator `\` available in Matlab, and the condition number of a matrix is estimated by the square root of the function `cond` on  $K^T K$  (also available in Matlab).

For the case of enriched IGA-C, the system of equations is non-square. Despite this, the same backslash operator from Matlab proved to be the most efficient solver available.

# Chapter 5

## Numerical Results

In this section, we show different 1D and 2D numerical examples. For problems with known analytical solutions, we use the following relative  $L^2$  norm of the error:

$$\frac{\|u - u^h\|_{L^2}}{\|u\|_{L^2}} = \sqrt{\frac{\int_{\Omega} |u - u^h|^2 \, d\Omega}{\int_{\Omega} |u|^2 \, d\Omega}}. \quad (5.1)$$

### 5.1. One-dimensional scattering

In the first example we consider a 1-Dimensional wave propagating in a space  $x \in (0, 1)$ , given by the following boundary value problem:

$$\begin{aligned} \frac{\partial^2 u}{\partial x^2} + k^2 u &= 0 && \text{in } x \in (0, 1) \\ \frac{\partial u}{\partial x} &= ik && \text{on } x = 0 \\ \frac{\partial u}{\partial x} &= -iku && \text{on } x = 1 \end{aligned} \quad (5.2)$$

The analytical solution is given by

$$u^{\text{exact}}(x) = \exp(ikx). \quad (5.3)$$

The purpose of this example is to demonstrate the ability of the PW-enriched IGA-C to recover the exact solution for any value of  $k$  using the coarsest mesh (one element) and to study the influence of the number of collocation points on the accuracy of the solution. This example is analogue to the so-called patch-test in computational mechanics.

Figure 5.1 shows the results of the normalized  $L^2$  error norm versus the number of collocation points with  $p = 3$  and plane-wave enrichment function ( $q = 1$ ). One element was employed for all the simulations. The results show that plane-wave enriched IGA-C achieves machine precision for all values of  $k$  with the same optimal number of collocation points (about 19).

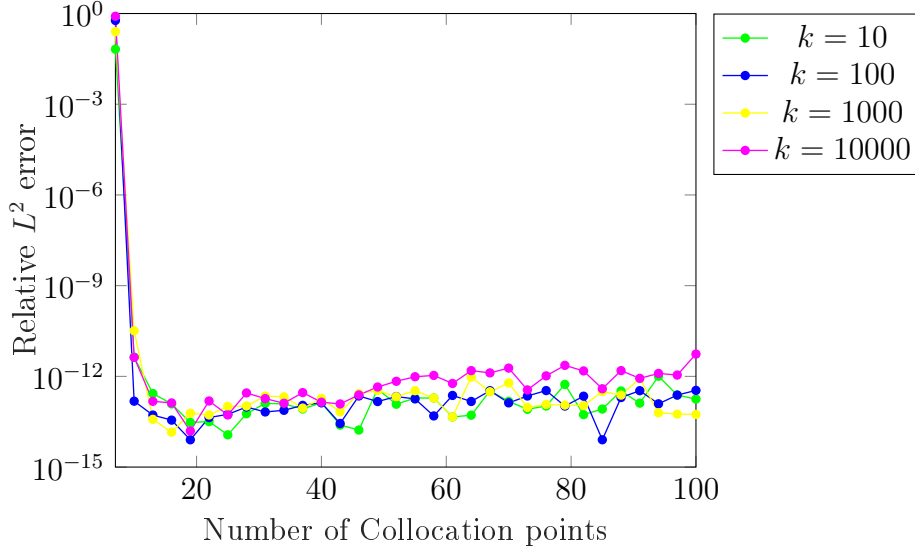


Figure 5.1: One dimensional example: PW-enriched IGA-C. Relative  $L^2$  error for  $p = 3$  versus the number of collocation points for different wave number  $k$ .

When using GHP-enrichment in this example, the solution is no longer exactly represented anymore, and the error depends on the mesh resolution and the number of enrichment functions. This happens because there is only one direction, and the Vekua functions are reduced to Bessel functions. The results are shown in Figure 5.2. Since we are interested in the behaviour of the enrichment, a mesh of 8 elements is fixed, and the error is plotted for an increasing number of enrichment functions. It can be seen that for  $q = 1, \dots, 4$  the error decreases drastically as more enrichment functions are added. If more than four enrichment functions are added, the error still decreases but much more slowly. Note, that the error in this case significantly depends on the number of collocation points. For example, for  $q = 2$  the system has 33 DOFs, but about 300 points are needed to obtain the minimum error, which cannot be improved by adding more collocation points. For  $q = 7$ , the optimal number of points is about 170 while the number of DOFs is 88, for  $q = 10$  about 280 points with 121 DOFs, etc. This behaviour indicates that the optimal number of collocation points significantly exceeds the number of DOFs and grows with the number of enrichment functions.

In Figures 5.3a and 5.3b, the error and condition number are plotted as function of wave number  $k$  for fixed mesh and increasing  $q$ . It can be seen that the condition number grows proportionally to  $k$  but does not depend on  $q$ . An interesting observation from Figure 5.3a is that on a fixed mesh, the efficiency of enrichment deteriorates as  $k$  grows. For example, for  $k = 10$  adding 3 enrichment functions improves accuracy from  $10^{-2}$  to  $10^{-8}$ , i.e. by six orders of magnitude, while for  $k = 100$  the same enrichment ( $q = 3$ ) has an improvement in

error from  $10^0$  to  $10^{-2}$ , and for  $k = 1000$  there is no improvement in the error for  $q$  up to 10. This behaviour indicates that enrichment alone cannot be used efficiently for large  $k$ , when the pollution error dominates, and increasing the mesh resolution is also required.

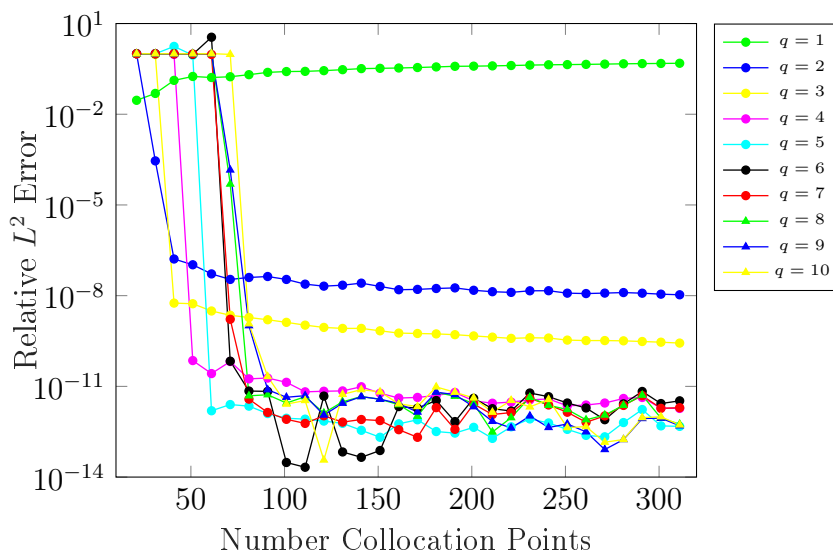
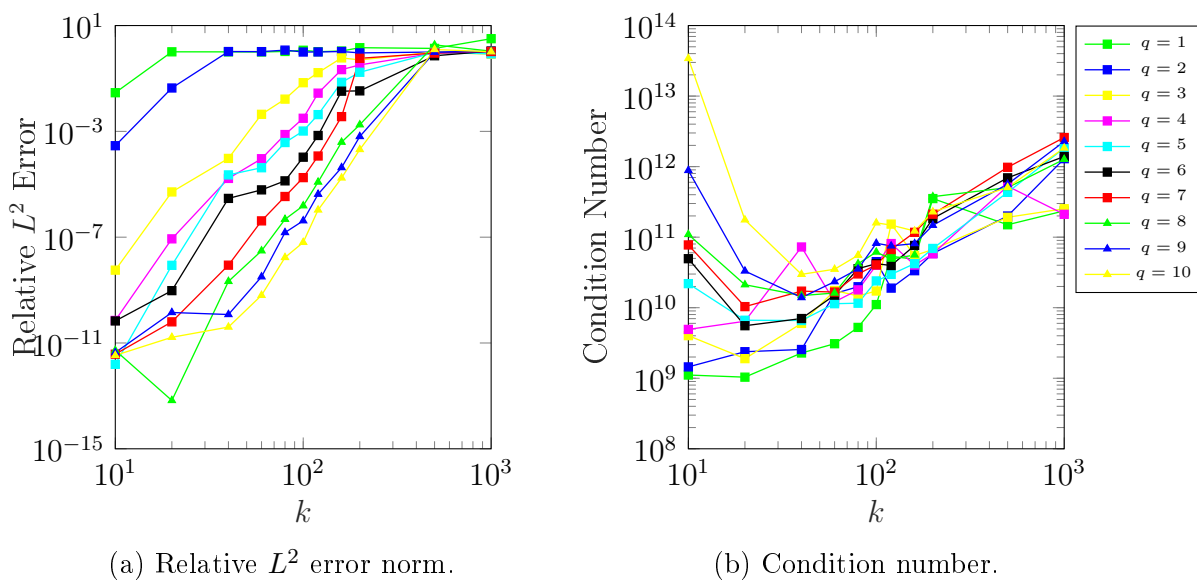


Figure 5.2: One dimensional example: GHP-enriched IGA-C. Relative  $L^2$  error for  $k = 10$  and  $p = 3$  versus the number of collocation points for different number of enrichment functions ( $q$ ). Fixed mesh of 8 elements



(a) Relative  $L^2$  error norm.

(b) Condition number.

Figure 5.3: One dimensional example: GHP-enriched IGA-C. Relative  $L^2$  error norm and condition number versus wave number  $k$  for  $p = 3$ , fixed mesh of 8 elements and increasing  $q$ .



## 5.2. Plane-wave scattered in a square domain

According to Figure 4.1 we consider a domain  $\Omega = [0, 1] \times [0, 1]$  with no obstacle, so the only boundary that exists is  $\Gamma_R$ . Therefore, the exterior acoustic number can be stated as: *Find  $u$  such that*

$$\Delta u + k^2 u = 0, \quad \text{in } \Omega \quad (5.4)$$

$$\frac{\partial u}{\partial n} - iku = f, \quad \text{on } \Gamma_R \quad (5.5)$$

The value of  $f$  is calculated using the analytical solution which is given by

$$u^{\text{exact}}(x, y) = e^{ik(x \cos \theta + y \sin \theta)}, \quad (5.6)$$

with  $\theta = \pi/4$ . The control points and the knot vectors are given in table A.1. The analytical solution of this example is shown in Figure 5.4

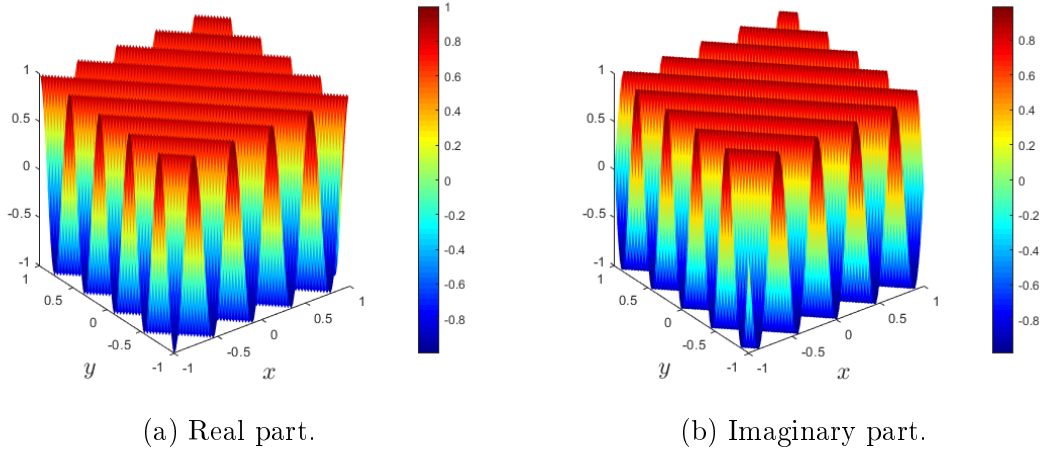


Figure 5.4: Analytical solution of the plane-wave scattered in a square domain problem with  $k = 40$ .

For the next results, the initial angle  $\theta_0$  of the plane wave enrichment system was shifted to  $\pi/4$ .

Figures 5.5, 5.6 and 5.7 shows the results of the  $L^2$  error norm and the condition number versus the number of collocation points, using a fixed mesh of 1 element and  $p = 3$ . As it can be seen in the results, the bigger the number of plane-waves  $q$ , the more collocation points are needed to solve the system of equation successfully. After reaching that optimal number, both the error norm and the condition number stagnates.

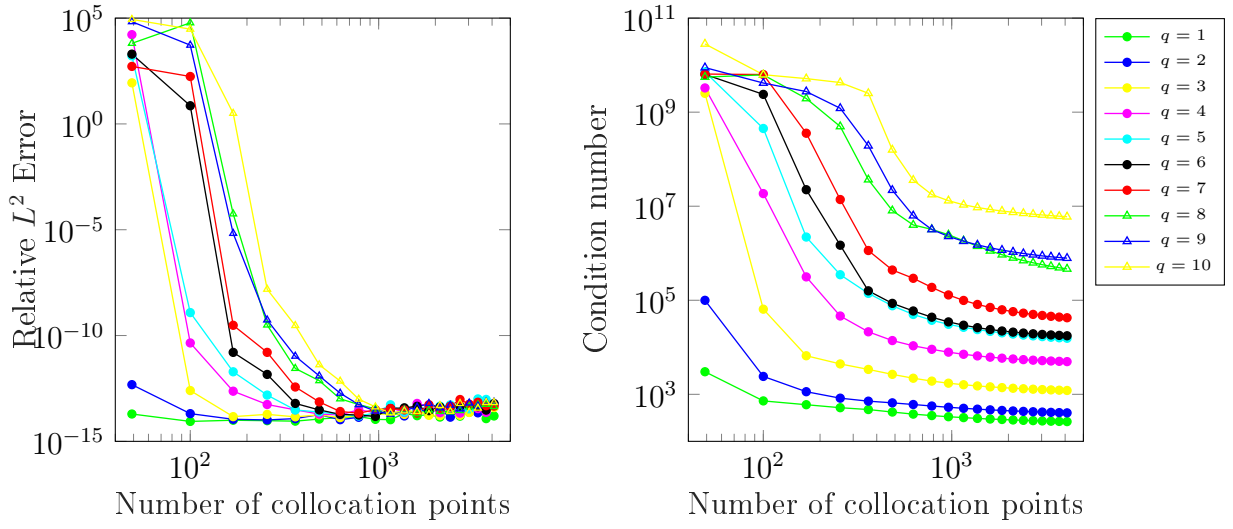


Figure 5.5: Square scattered patch test: Relative  $L^2$  error and condition number versus the number of collocation points for  $p = 3$  and  $k = 10$ . Fixed mesh of 1 element. Plane wave enrichment was employed in all the simulations.

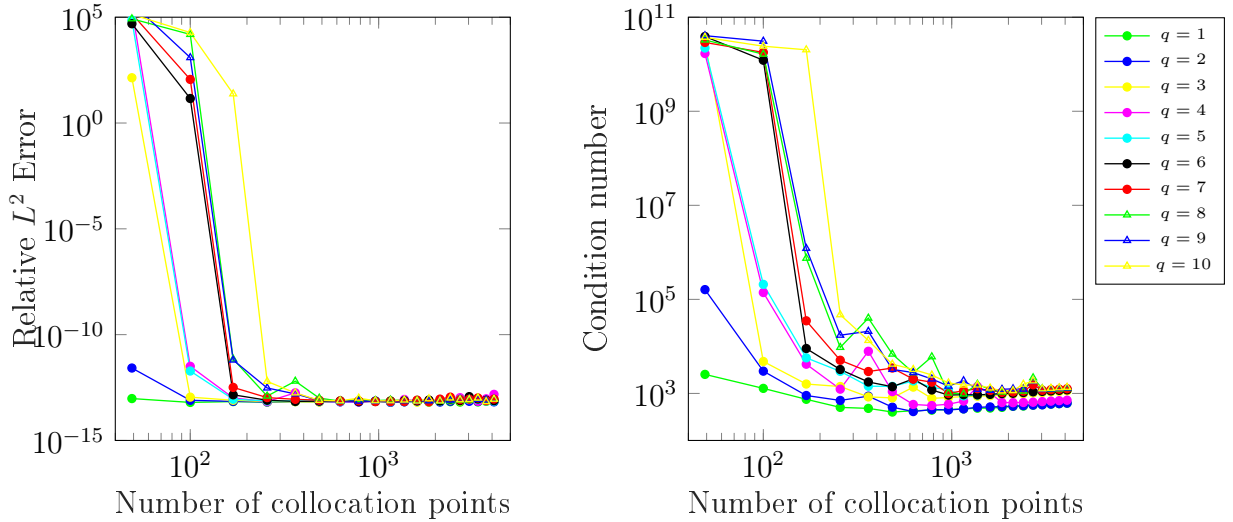


Figure 5.6: Square scattered patch test: Relative  $L^2$  error and condition number versus the number of collocation points for  $p = 3$  and  $k = 50$ . Fixed mesh of 1 element. Plane wave enrichment was employed in all the simulations.

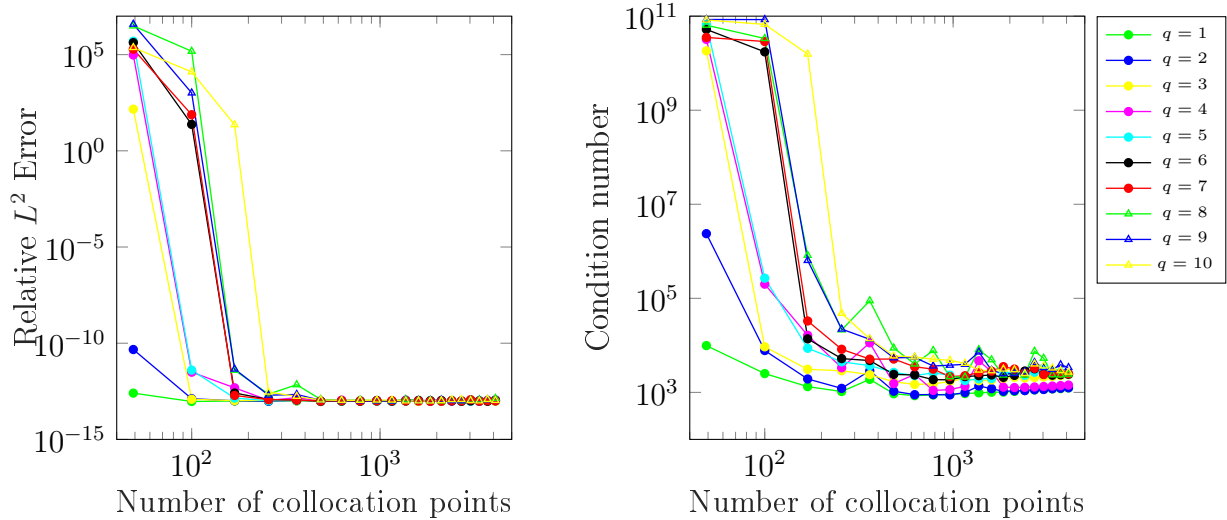


Figure 5.7: Square scattered patch test: Relative  $L^2$  error and condition number versus the number of collocation points for  $p = 3$  and  $k = 100$ . Fixed mesh of 1 element. Plane wave enrichment was employed in all the simulations.

### 5.3. The duct problem

In this example, we consider  $\Omega = [0, 2] \times [0, 1]$  as shown in Figure 5.8. We solve the following BVP:

$$\begin{aligned} \Delta u + k^2 u &= 0 && \text{in } \Omega \\ \frac{\partial u}{\partial n} &= \cos(m\pi y) && \text{on } x = 0 \\ \frac{\partial u}{\partial n} &= -iku && \text{on } x = 2 \\ \frac{\partial u}{\partial n} &= 0 && \text{on } y = 0, 1 \end{aligned} \tag{5.7}$$

In this problem,  $m \in \mathbb{N}$  is the mode number, which is related to the Neumann boundary condition on  $x = 0$ . The exact solution of this problem is as follows

$$u^{\text{exact}}(x, y) = \cos(m\pi y) (A_1 e^{-ik_x x} + A_2 e^{ik_x x}), \tag{5.8}$$

where  $k_x = \sqrt{k^2 - (m\pi)^2}$  and the coefficients  $A_1$  and  $A_2$  are obtained from the system:

$$\begin{pmatrix} ik_x x & -ik_x \\ i(k - k_x) e^{-2ik_x} & i(k + k_x) e^{2ik_x} \end{pmatrix} \begin{pmatrix} A_1 \\ A_2 \end{pmatrix} = \begin{pmatrix} 1 \\ 0 \end{pmatrix} \tag{5.9}$$

If  $k > m\pi$  the wave is propagating and if  $k < m\pi$  the wave is evanescent. In this paper, only the propagating modes are considered and for every value of  $k$  the highest propagating mode was chosen. This means that in all the results for this example, for every value of  $k$  we picked the highest natural value of  $m$ . The only exception for this rule is  $m = 0$  in section 5.3 and  $k = 10$ ,  $m = 2$  in section 5.3. The geometry is parameterized with linear NURBS and remains unchanged during the solution refinement process. The real and imaginary parts of the analytical solution with  $k = 10$  and  $m = 2$  are shown in Figure 5.9.

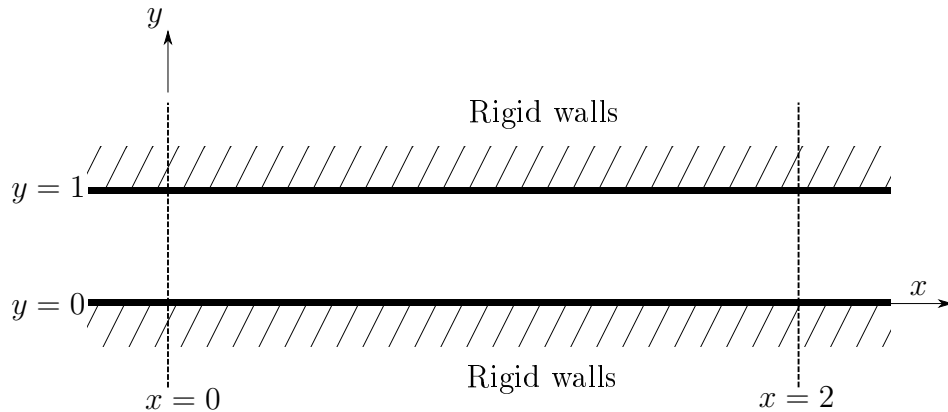


Figure 5.8: The duct problem: domain.

The control points and the knot vectors are given in table A.2

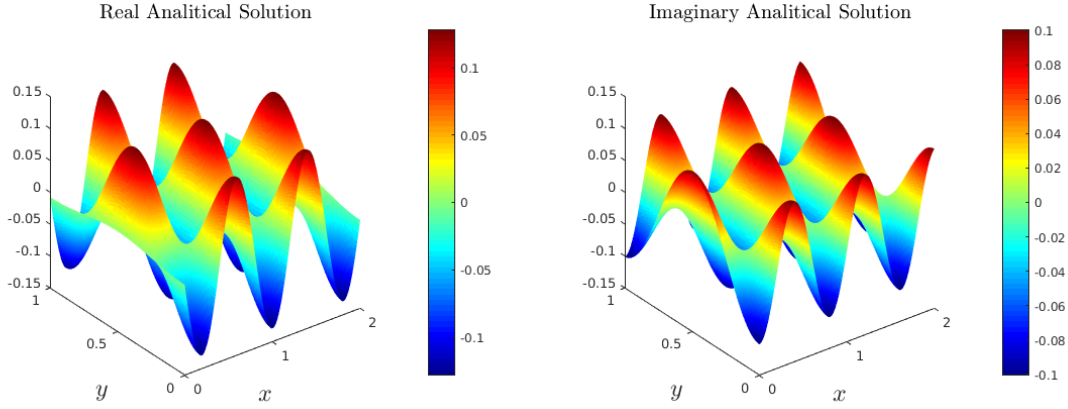


Figure 5.9: Analytical solution

### Duct example: Patch test for the PW-enriched IGA-C

We first start with a patch test to investigate the ability of the PW-enriched IGA-C to recover the exact solution. The exact solution is obtained from eq.(5.9) with  $m = 0$ . In this case, two plane waves propagating in the opposite directions along  $x$ -axis can exactly represent the analytical solution. It can be seen in Figures 5.10a and 5.10b, where the relative  $L^2$  error norm is plotted versus the number of collocation points, that for even numbers of enrichment functions nearly machine precision is achieved on one element while for odd numbers the error remains considerably large even if more enrichment functions are added. Still, the optimal number of collocation points also increases when  $q$  increases. The error seems to be independent on  $k$  (in Figures 5.10a and 5.10b, the same precision is achieved for  $k = 10$  and  $k = 100$ ), as was previously observed in the one-dimensional patch test (section 5.1). Despite this, the result again demonstrates that the pollution error cannot be overcome by increasing the enrichment space without increasing the mesh resolution (odd  $q$  and fixed one element mesh).

### Convergence study for different collocation schemes

In this study, we assess the performance of the Greville Abcissae, Approximated Cauchy-Galerkin and Superconvergent IGA-C in comparison with the Galerkin IGA. Figure 5.11 shows the convergence plots in terms of the Relative  $L^2$  error norm versus the DOFs for B-splines of degree  $p = 3, 4, 5$ , using  $k = 10$  and  $m = 2$ . The plots show that IGA-C with SC points outperforms both the ACG and GA points in terms of the convergence rate. In particular, Figure 5.11b shows that the IGA-C with ACG and IGA-C with GA lead to the same error, which is consistent with the fact that GA and ACG points for  $p = 4$  are the same. The expected and observed convergences rates are summarized in Table 5.1. It is interesting to notice that for both even and odd  $p$ , the IGA-C with SC points delivers convergence rates slightly higher than the theoretical rates reported in the literature.

Figure 5.12 shows the comparison between Greville Abcissae, Approximated Cauchy-Galerkin and Superconvergent IGA-C versus the Galerkin IGA in terms of the condition number versus the DOFs for B-splines of degree  $p = 3, 4, 5$  using  $k = 10$  and  $m = 2$ . For all the curves, the condition number increases when increasing the DOFs. Also, it can be noticed that for odd  $p$ , both the SC and the ACG collocation points leads to almost the

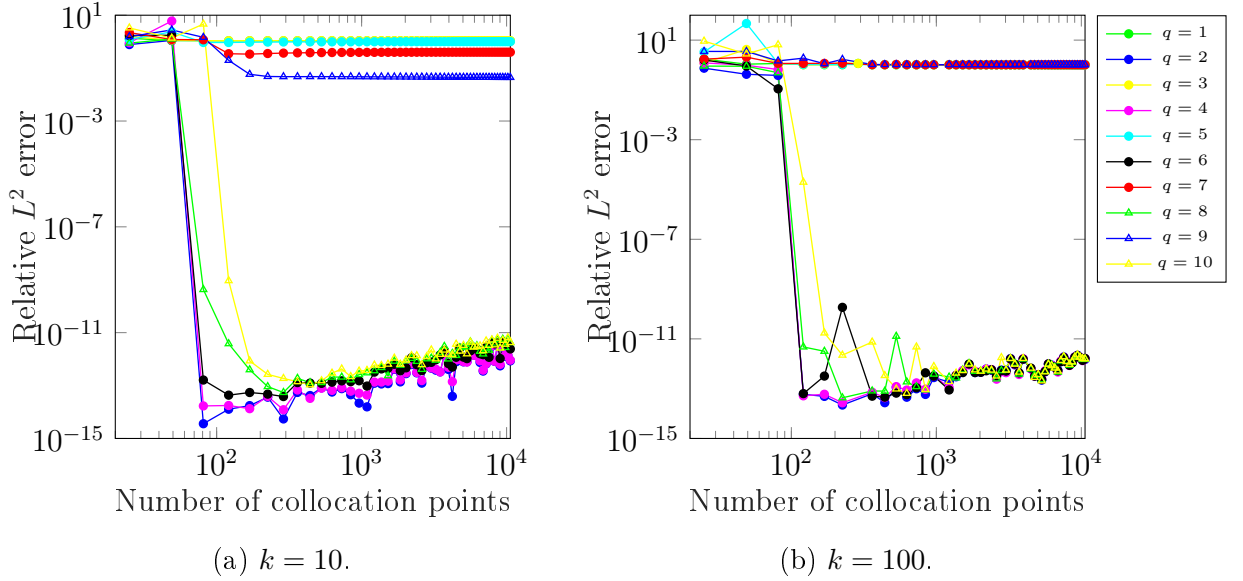


Figure 5.10: Duct patch test: PW-enriched IGA-C. Relative  $L^2$  error for  $p = 2$  versus the number of collocation points for different number of enrichment functions,  $m = 0$ , one element in the mesh.

same condition number, even though both the position and quantity of collocation points are not the same. In all the plots, the condition number reported for the Galerkin IGA is the smallest, while the condition number reported for the IGA-C with ACG points is the highest.

Figure 5.13 shows the absolute error map using a fixed mesh of 4225 elements, B-splines of degree  $p = 3$ , and the wave parameters  $k = 10$   $m = 2$  for Galerkin IGA (Figure 5.13a) and IGA-C with SC (Figure 5.13b), GA (Figure 5.13c) and ACG (Figure 5.13d) points. The absolute error map plot for the Galerkin IGA is both more symmetric and lower in terms of magnitude compared to the IGA-C methods.

Then, the wave number  $k$  is increased to 100 to study the pollution error in different methods. Figures 5.14 and 5.15 report both the  $L^2$  error norm and the condition number, respectively, for B-splines of degree  $p = 3, 4, 5$ . In this case, IGA-C for all collocation points schemes seem to be more sensitive to the pollution error in comparison with Galerkin IGA of the same degree (i.e. more DOFs are required to achieve asymptotic convergence range, and the difference between Galerkin and IGA-C error is much more significant in comparison to Figure 5.11 ). Comparing three collocation schemes, ACG seems to perform slightly better.

As can be seen in all plots, Galerkin IGA outperforms all IGA-C schemes tested. However, the advantages of IGA-C are more evident when one considers the number of function evaluations. Figure 5.16 shows the  $L^2$  error norm versus the total number of quadrature/collocation points. For the Galerkin IGA, we employed  $(p+1)^2$  quadrature points per elements, while for the IGA-C, the number of collocation points is given by the collocation scheme. In the plots of Figure 5.16, it can be seen that initially, for  $p = 3, 4$ , both the IGA-C with ACG and GA points are better in terms of error per collocation point, but after some  $10^4$  collocation/quadrature points, Galerkin IGA outperforms the other methods. For  $p = 5$ , it seems that IGA-C with SC and ACG points outperforms the Galerkin IGA.

For the remaining examples, IGA-C with ACG points will be employed, since it shows the best balance between the convergence rates, overall error and ratio of collocation points versus control points.

Table 5.1: Duct example: Expected and observed convergence rates ( $L^2$  error norm vs DOF) for the IGA Galerkin, IGA-C GA, SC and ACG methods from Figure 5.11

Method	Expected convergence rate	Observed convergence rate		
		$p = 3$	$p = 4$	$p = 5$
IGA Galerkin	$(p + 1)/2$	2	2.4	3
IGA-C GA	odd $(p - 1)/2$ ; even $p/2$	1.1	2.1	2.2
IGA-C SC	odd $(p + 1)/2$ ; even $p/2$	2.6	2.3	3.3
IGA-C ACG	$p/2$	1.5	2.1	2.5

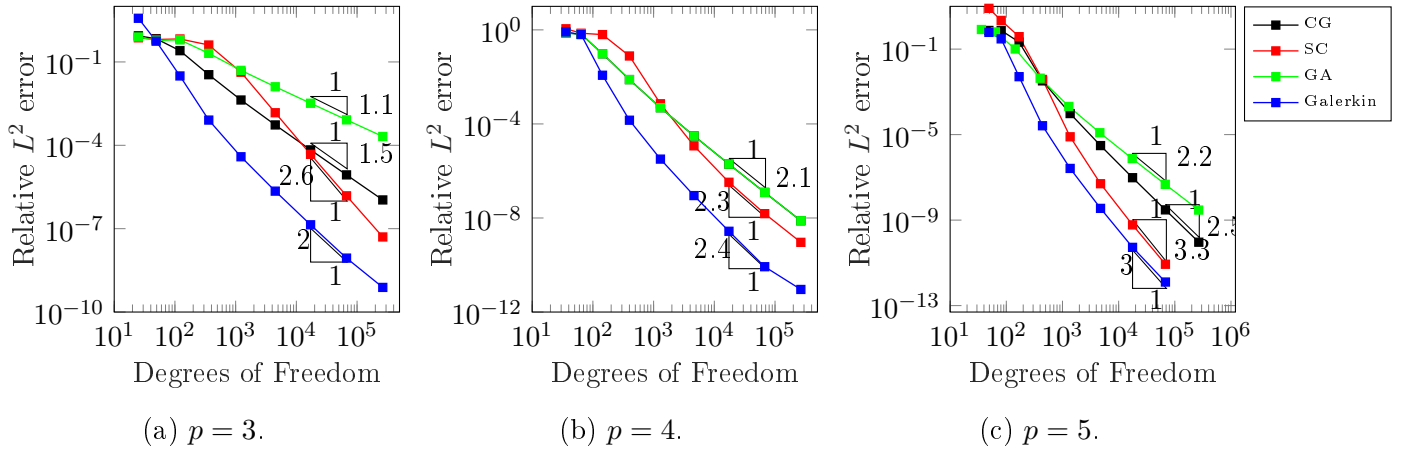


Figure 5.11: Duct example: Comparison between IGA-C using GA, SC and ACG points, and Galerkin IGA for the Relative  $L^2$  error norm for B-splines of degree  $p = 3, 4$  and  $5$ , versus the number of degrees of freedom.  $k = 10$  and  $m = 2$ .

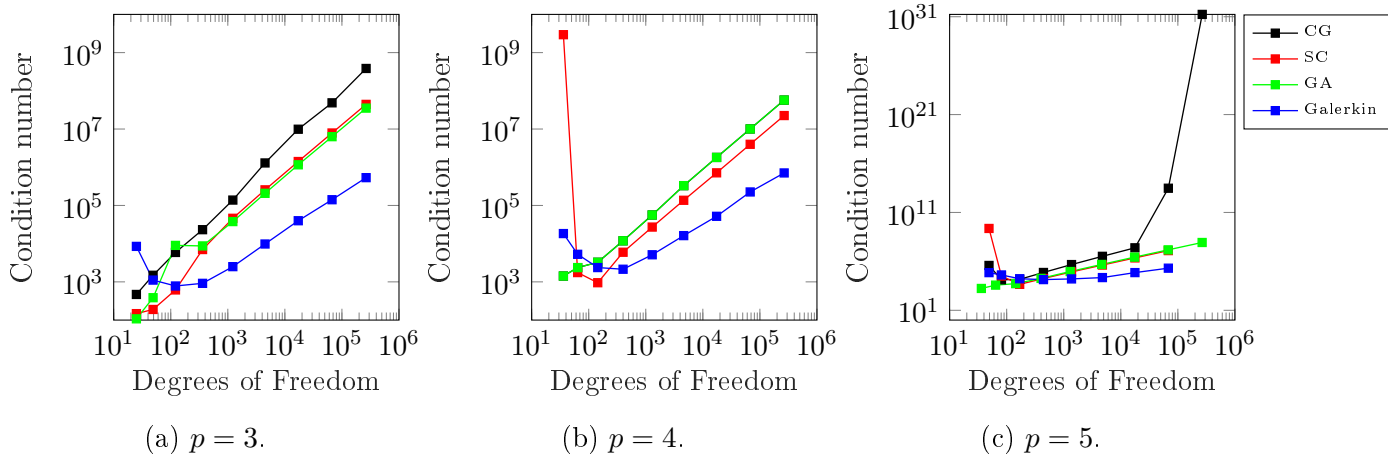


Figure 5.12: Duct example: Comparison between IGA-C using GA, SC and ACG points, and Galerkin IGA for the Condition number for B-splines of degree  $p = 3, 4$  and  $5$ , versus the number of degrees of freedom.  $k = 10$  and  $m = 2$ .



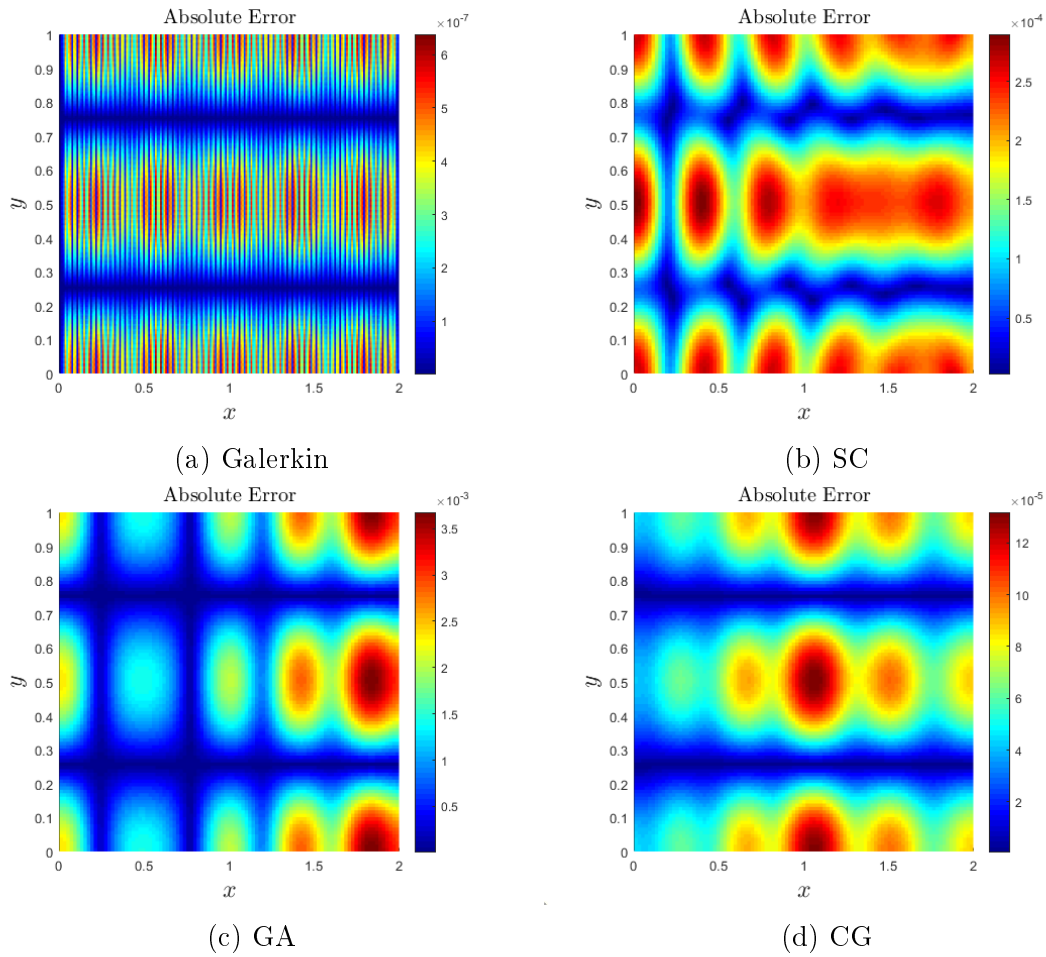


Figure 5.13: Duct example: Absolute error for a fixed mesh of 4225 elements. Comparison between Galerkin IGA, SC, GA and ACG IGA-C methods.  $p = 3$ ,  $k = 10$  and  $m = 2$ .

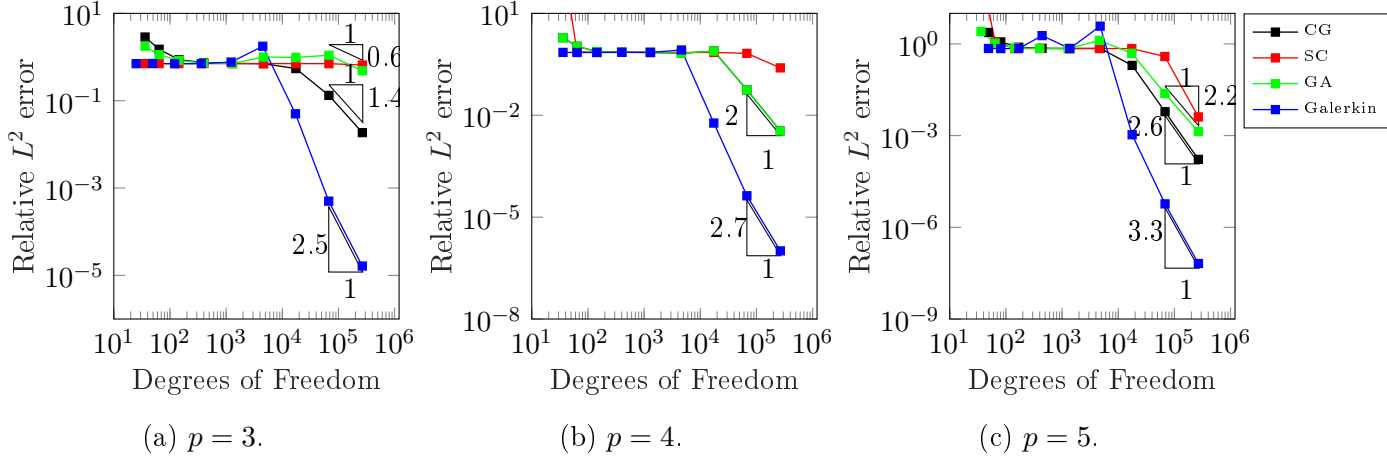


Figure 5.14: Duct example: Comparison between IGA-C using GA, SC and ACG points, and Galerkin IGA for the Relative  $L^2$  error norm for B-splines of degree  $p = 3, 4$  and  $5$ , versus the number of degrees of freedom.  $k = 100$  and  $m = 2$ .

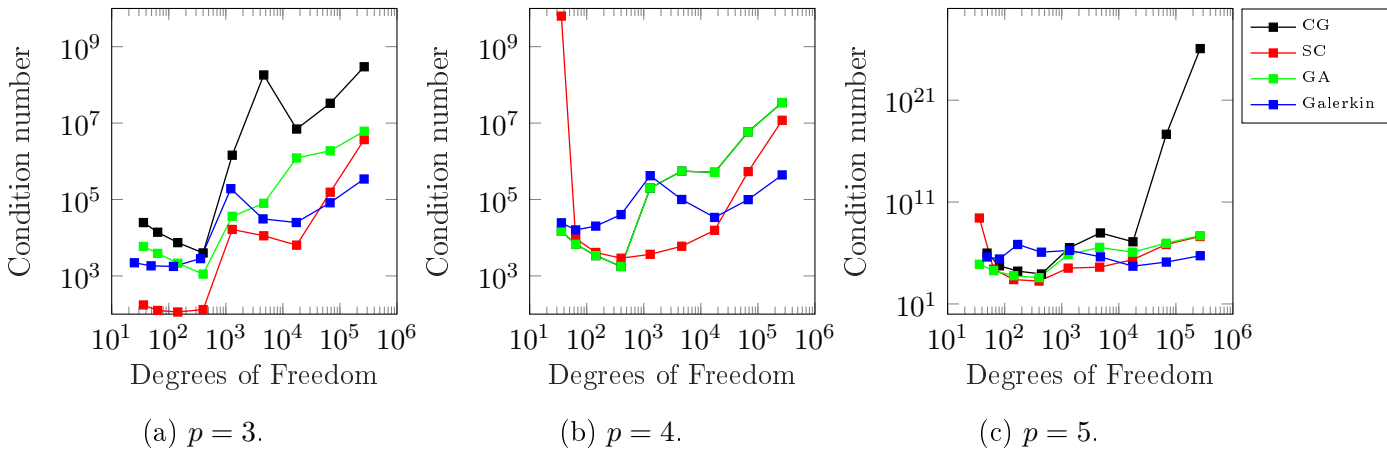


Figure 5.15: Duct example: Comparison between IGA-C using GA, SC and ACG points, and Galerkin IGA for the Condition number for B-splines of degree  $p = 3, 4$  and  $5$ , versus the number of degrees of freedom.  $k = 100$  and  $m = 2$ .

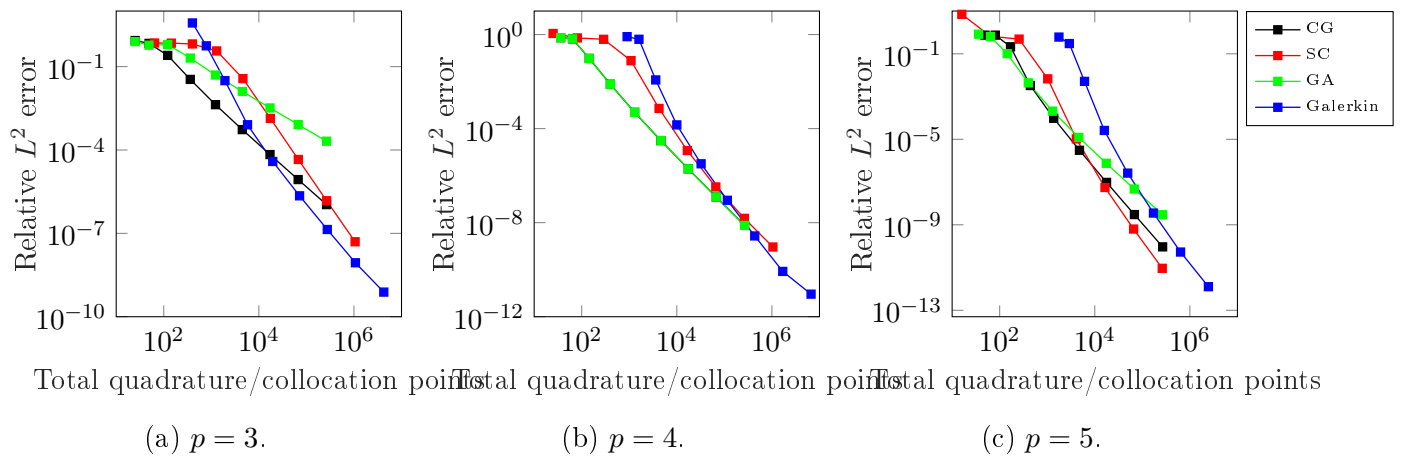


Figure 5.16: Duct example: Comparison between IGA-C using GA, SC and ACG points, and Galerkin IGA for the Relative  $L^2$  error norm for B-splines of degree  $p = 3, 4$  and  $5$ , versus the number of degrees of freedom.  $k = 10$  and  $m = 2$ .

## Collocation schemes for the enriched IGA-C

As mentioned in subsection 4.3.3, one of the goals of this paper is to find an efficient collocation scheme for the enriched basis that we are testing. To achieve this, we started with the ACG points and progressively added additional collocation points equidistantly in between them. Figures 5.17 and 5.18 show the convergence plots for the  $L^2$  error norm and the condition number versus the number of collocation points, for a fixed mesh of 64 elements using PW- and GHP- enrichment, respectively. From these studies, we conclude that the most suitable choice is to add  $q + 1$  and  $q$  additional equidistant collocation points between the initial ACG points, for PW- and GHP- enrichment, respectively. This number of collocation points is employed in all further studies.

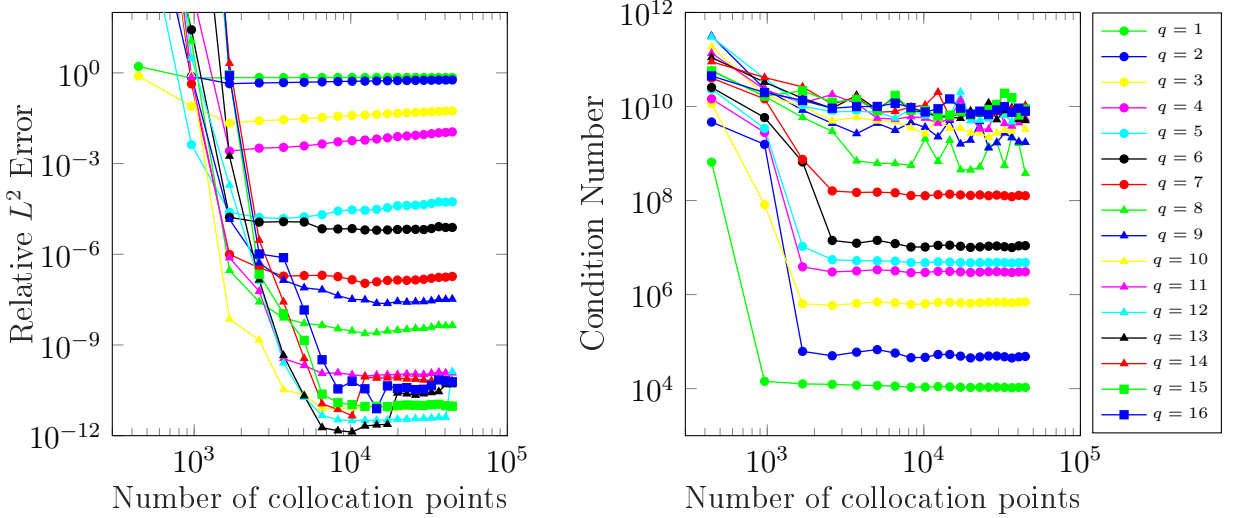


Figure 5.17: Relative  $L^2$  error and condition number using  $p = 3$  and plane-wave enrichment for  $k = 10$  and  $m = 2$ . Fixed mesh of 64 elements.

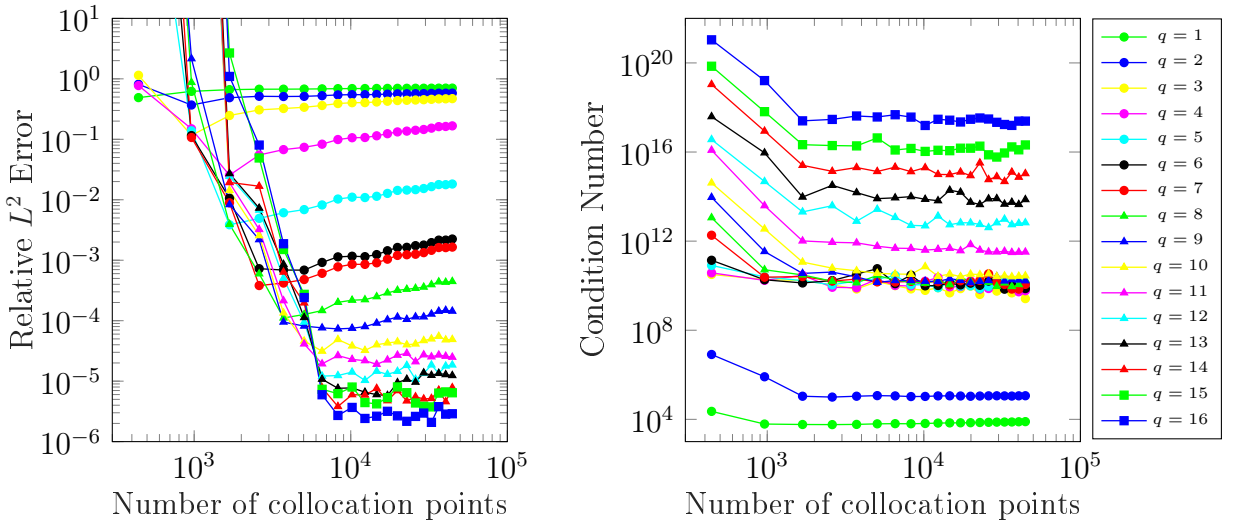


Figure 5.18: Relative  $L^2$  error and condition number using  $p = 3$  and generalized harmonic polynomial enrichment (half span) for  $k = 10$  and  $m = 2$ . Fixed mesh of 64 elements.

### PW-enrichment: convergence study for $k = 10$ and $m = 2$

Figures 5.19, 5.20 and 5.21 show the convergence study in terms of the DOF for both the  $L^2$  error norm and the condition number, using  $p = 3, 4$  and  $5$  with  $q$  from  $0$  to  $16$ ,  $k = 10$  and  $m = 2$ . In all simulations PW-enrichment is employed. Note, that in this case, for any fixed  $q$ , the number of DOF is increased by  $h$ -refining the mesh. The figures show that increasing the enrichment basis can significantly improve the overall error. However, for large numbers of enrichment function, the error seems to stay constant or even grow with  $h$ -refinement.

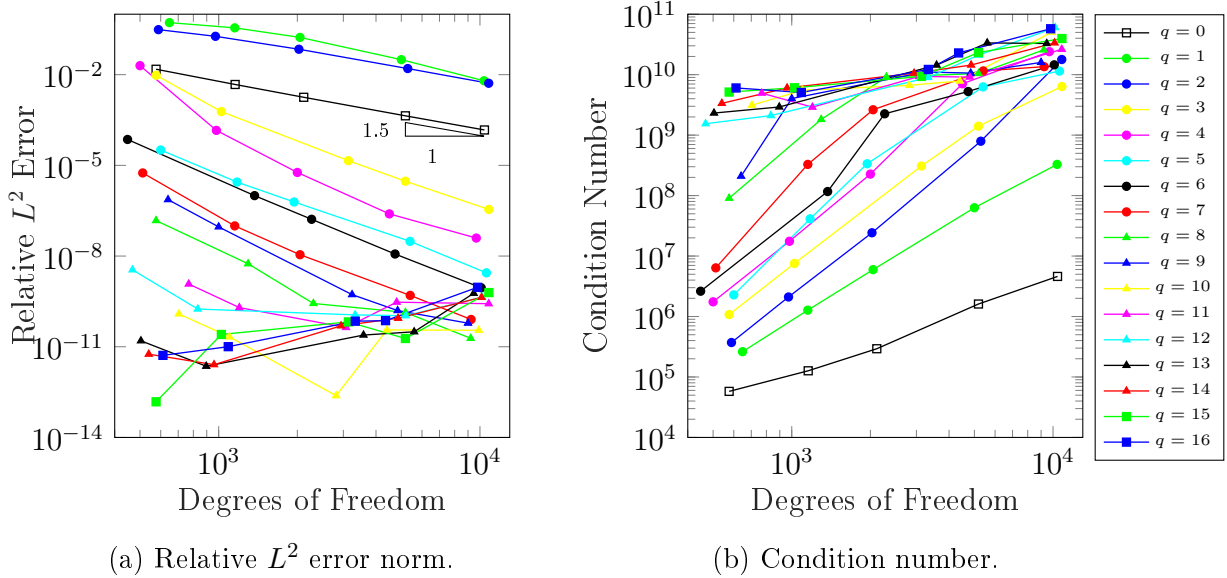


Figure 5.19: The duct example: Relative  $L^2$  error norm and Condition number study for  $p = 3$ ,  $k = 10$  and  $m = 2$ .

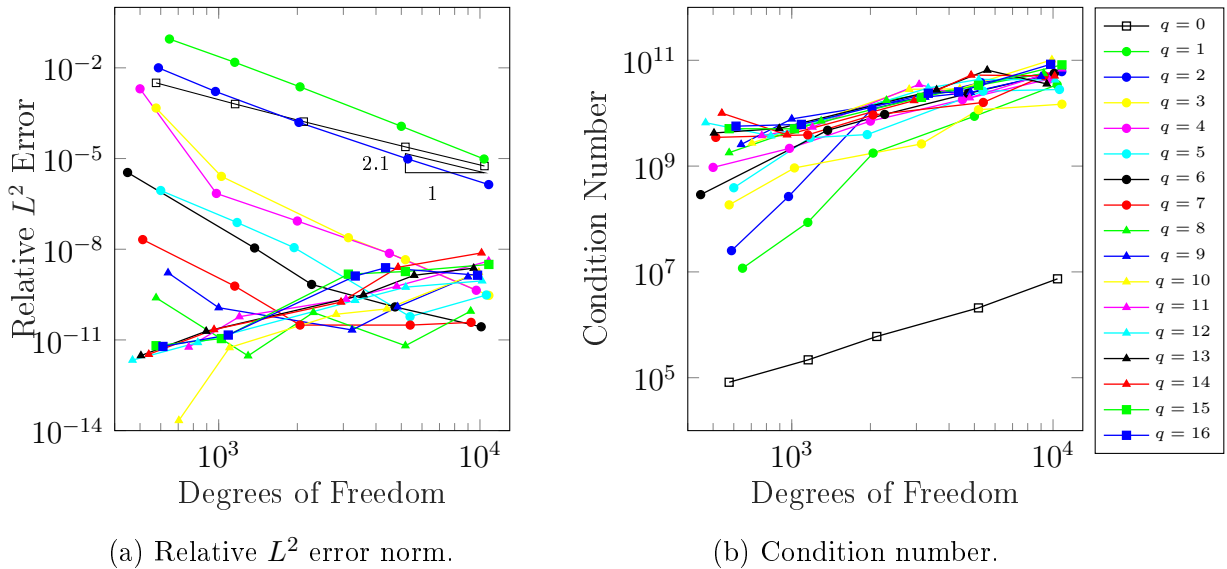
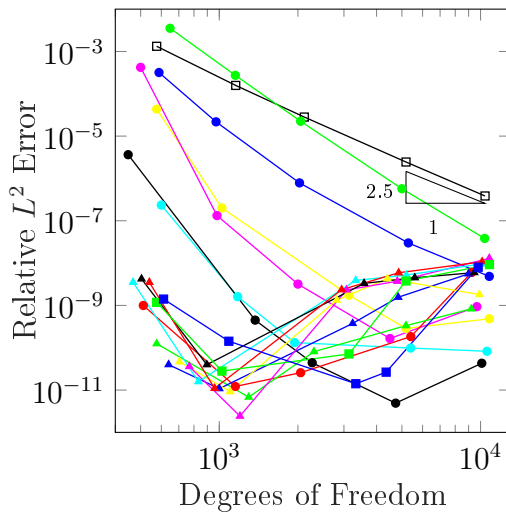
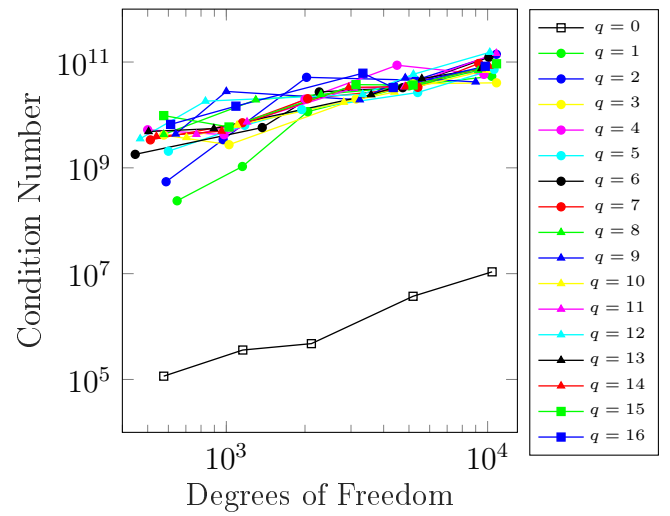


Figure 5.20: The duct example: Relative  $L^2$  error norm and Condition number study for  $p = 4$ ,  $k = 10$  and  $m = 2$ .



(a) Relative  $L^2$  error norm.



(b) Condition number.

Figure 5.21: The duct example: Relative  $L^2$  error norm and Condition number study for  $p = 5$ ,  $k = 10$  and  $m = 2$ .

### DOF convergence study for $k = 40$ and $m = 12$ using Plane wave enrichment

Figures 5.22, 5.23 and 5.24 show the convergence study in terms of the DOF for both the  $L^2$  error norm and the condition number, using  $p = 3, 4$  and  $5$  with  $q$  from  $0$  to  $16$ . In all the simulations plane-wave enrichment is employed. The wave number  $k$  is fixed to  $40$  and  $m = 12$ .

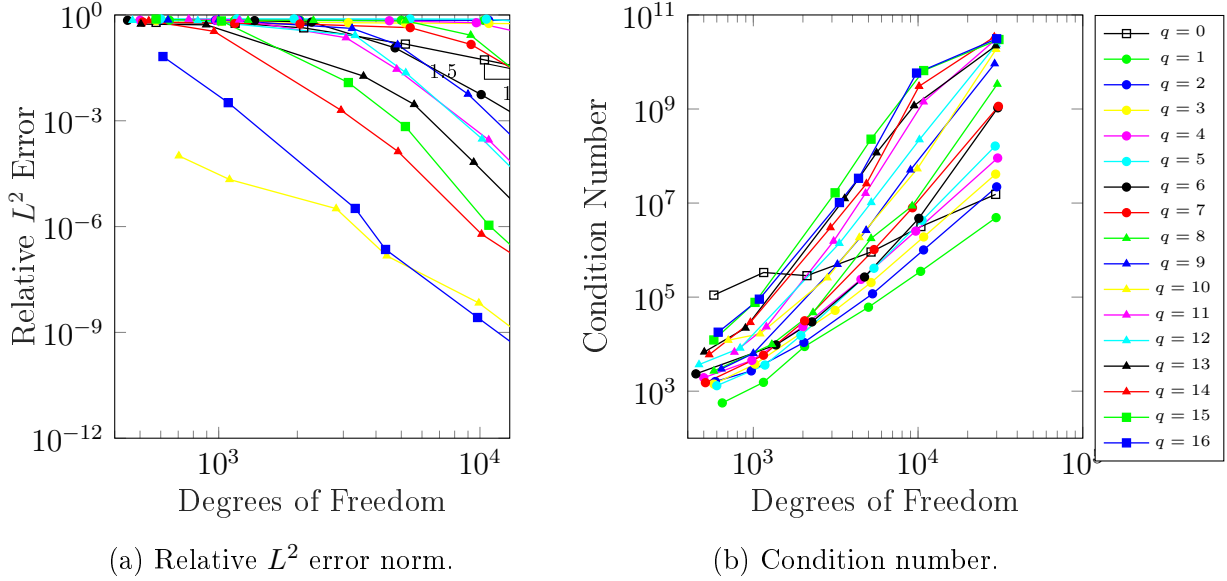


Figure 5.22: The duct example: Relative  $L^2$  error norm and Condition number study for  $p = 3$ ,  $k = 40$  and  $m = 12$ .

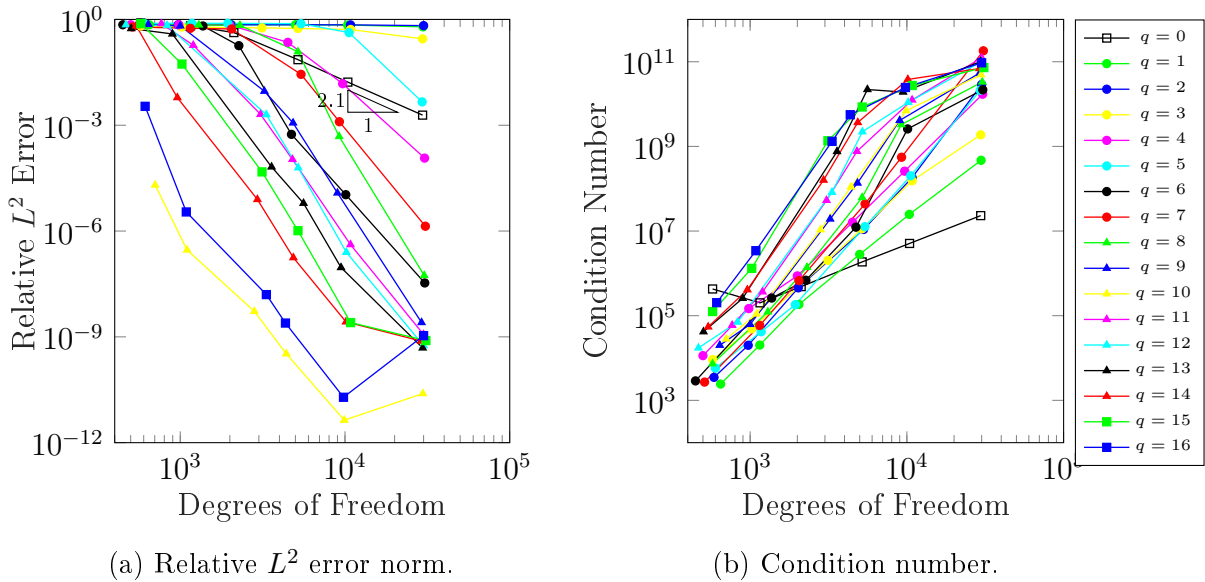
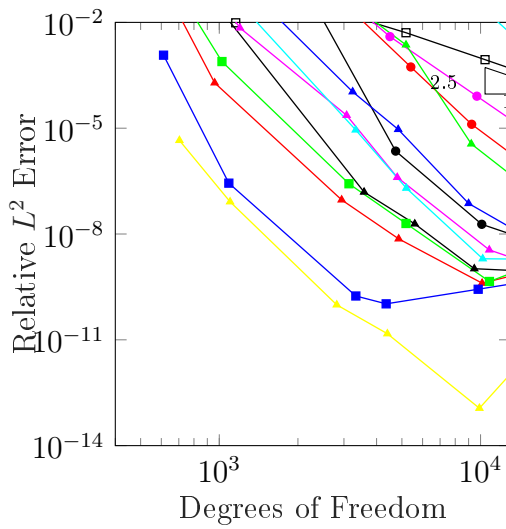
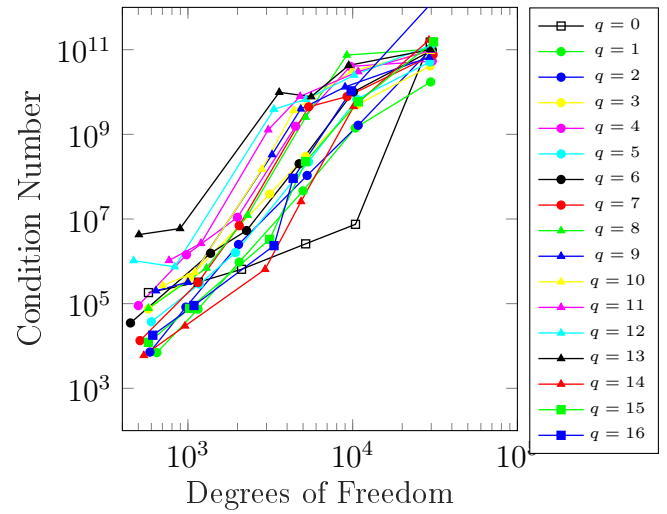


Figure 5.23: The duct example: Relative  $L^2$  error norm and Condition number study for  $p = 4$ ,  $k = 40$  and  $m = 12$ .



(a) Relative  $L^2$  error norm.



(b) Condition number.

Figure 5.24: The duct example: Relative  $L^2$  error norm and Condition number study for  $p = 5$ ,  $k = 40$  and  $m = 12$ .



### DOF convergence study for $k = 80$ and $m = 25$ using PW-enrichment

Figures 5.25, 5.26 and 5.27 show the convergence study in terms of the DOF for both the  $L^2$  error norm and the condition number, using  $p = 3, 4$  and  $5$  with  $q$  from  $0$  to  $16$ . In all the simulations plane-wave enrichment is employed. The wave number  $k$  is fixed to  $80$  and  $m = 25$ .

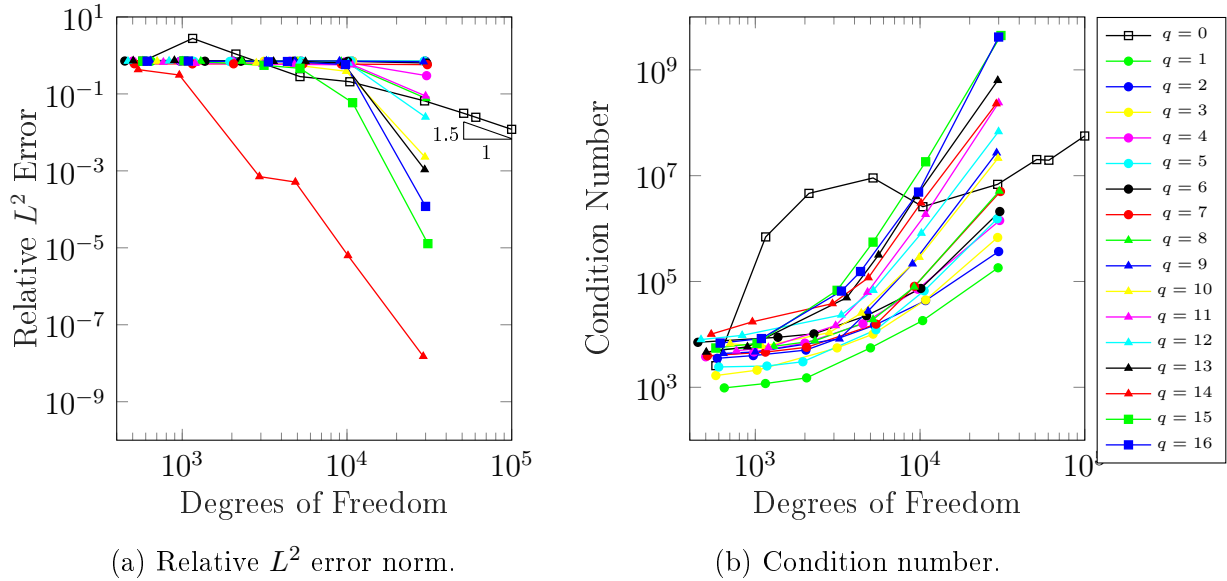


Figure 5.25: The duct example: Relative  $L^2$  error norm and Condition number study for  $p = 3$ ,  $k = 80$  and  $m = 25$ .

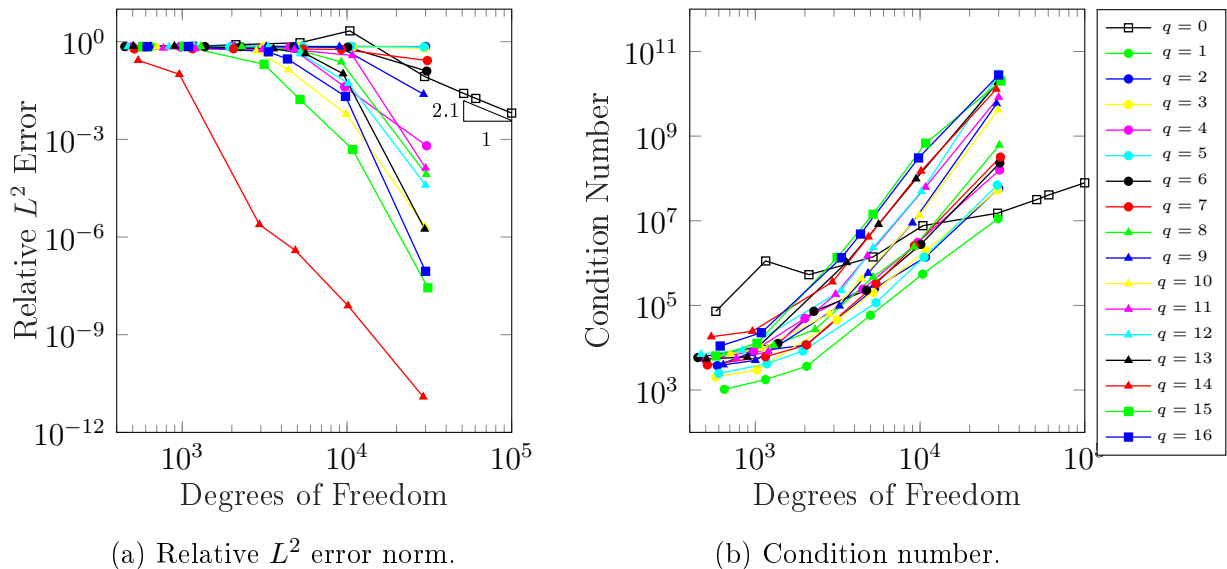
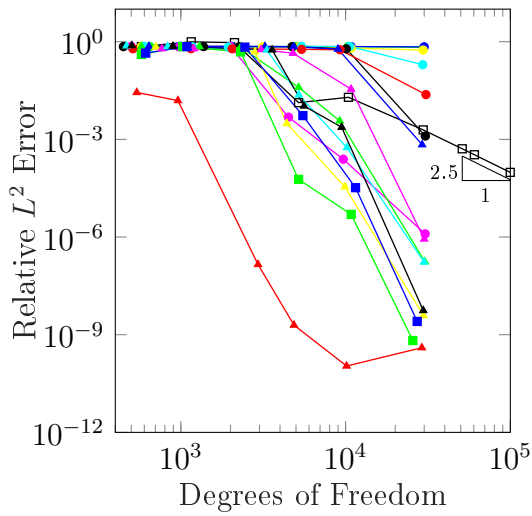
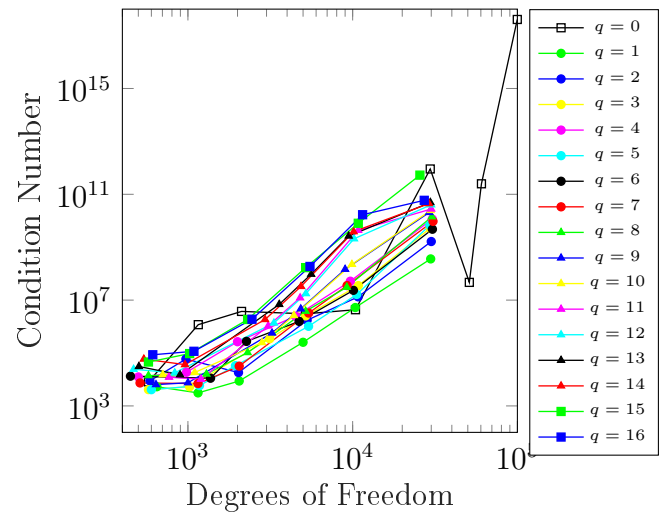


Figure 5.26: The duct example: Relative  $L^2$  error norm and Condition number study for  $p = 4$ ,  $k = 80$  and  $m = 25$ .



(a) Relative  $L^2$  error norm.



(b) Condition number.

Figure 5.27: The duct example: Relative  $L^2$  error norm and Condition number study for  $p = 5$ ,  $k = 80$  and  $m = 25$ .

### PW-enrichment: convergence study for $k = 120$ and $m = 38$

Figures 5.28, 5.29 and 5.30 show the convergence study in terms of the DOF for both the  $L^2$  error norm and the condition number, using  $p = 3, 4$  and  $5$  with  $q$  from  $0$  to  $16$ . In all the simulations, plane-wave enrichment is employed. The wave number  $k$  is fixed to  $120$  and  $m = 38$ .

In this study, it can be seen that as  $k$  grows, the efficiency of enriched IGA-C deteriorates significantly. On coarse meshes, when the pollution error prevails over discretization error, no improvement in accuracy is seen even if a large number of enrichment functions are added. In the asymptotic regime, a large number of PW can improve the solution. However, the behaviour of the method is sensitive to the choice of parameters and no clear dependence between the number of PW and the accuracy of the solution is seen.

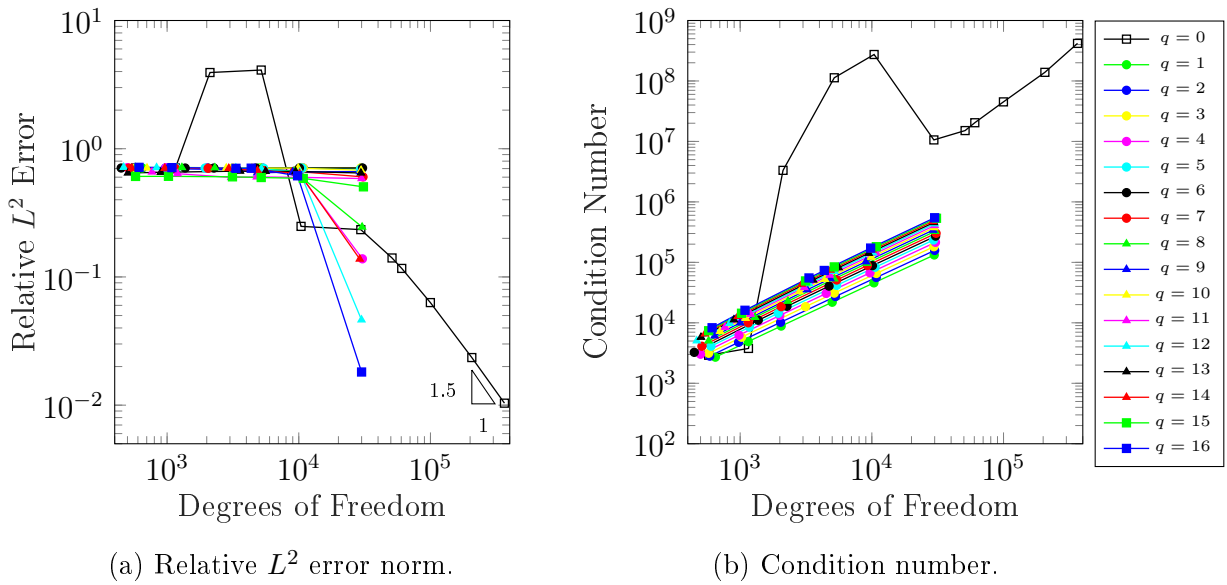
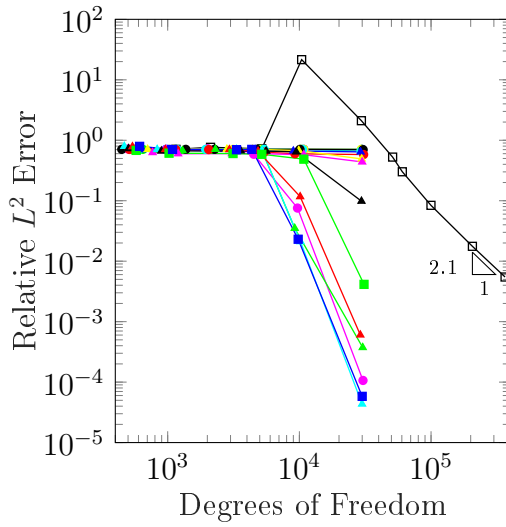
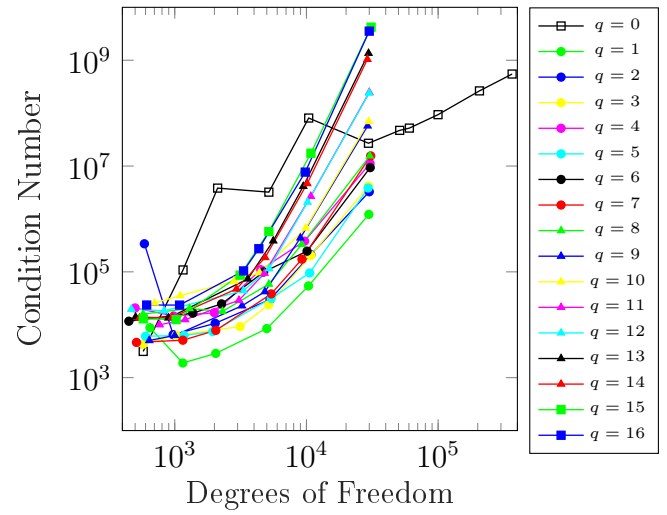


Figure 5.28: The duct example: Relative  $L^2$  error norm and Condition number study for  $p = 3$ ,  $k = 120$  and  $m = 38$ .

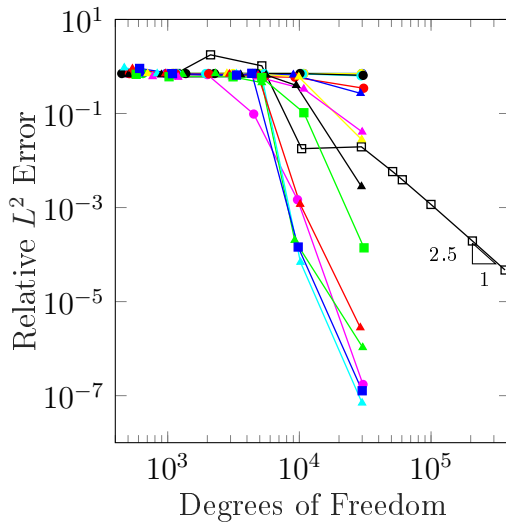


(a) Relative  $L^2$  error norm.

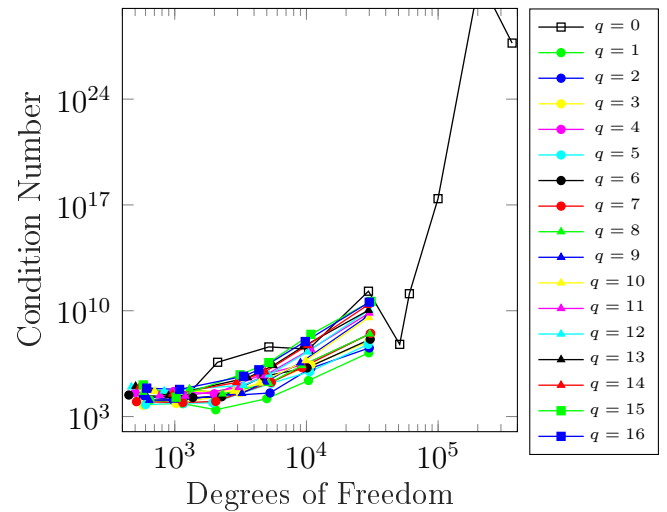


(b) Condition number.

Figure 5.29: The duct example: Relative  $L^2$  error norm and Condition number study for  $p = 4$ ,  $k = 120$  and  $m = 38$ .



(a) Relative  $L^2$  error norm.



(b) Condition number.

Figure 5.30: The duct example: Relative  $L^2$  error norm and Condition number study for  $p = 5$ ,  $k = 120$  and  $m = 38$ .

### PW-enrichment: wave number study

Figures 5.31, 5.31 and 5.33 shows the convergence study in terms of the wave number for both the  $L^2$  error norm and the condition number, using  $p = 3$ ,  $p = 4$  and  $p = 5$  with  $q$  from 0 to 16. In all the simulations, plane-wave enrichment is employed. As we mentioned at the beginning of subsection 5.3, the  $m$  value for every  $k$  is chosen to be the highest natural number that allows wave propagation. The mesh is fixed to  $8 \times 8$  elements. This study again shows that efficiency of PW-enrichment deteriorates as  $k$  grows, meaning that for the same accuracy, as  $k$  increases, more enrichment functions need to be added to the basis.

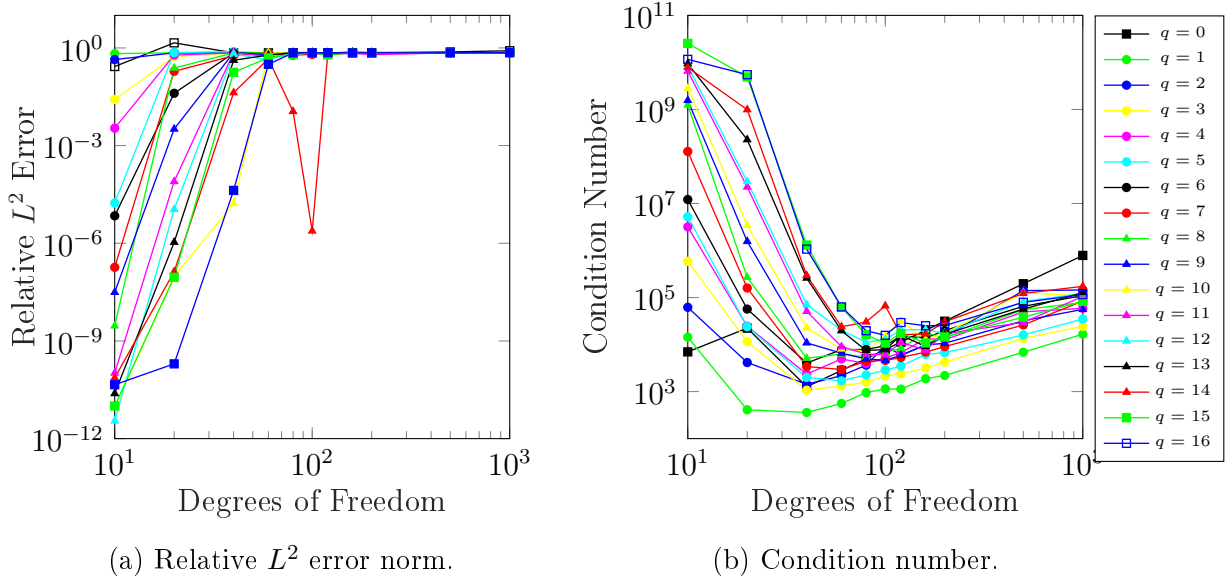


Figure 5.31: Duct example: Wave study for a fixed mesh. Comparison between plane-wave enriched and non-enriched collocation methods. The mesh has 64 elements.  $p = 3$

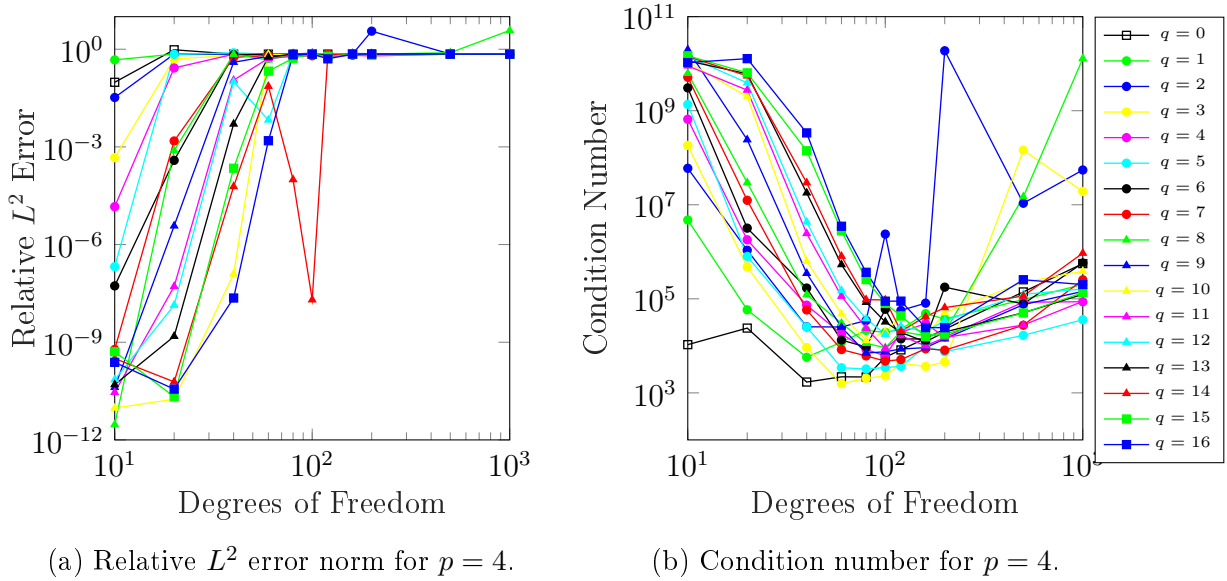


Figure 5.32: Duct example: Wave study for a fixed mesh. Comparison between plane-wave enriched and non-enriched collocation methods. The mesh has 64 elements.  $p = 4$

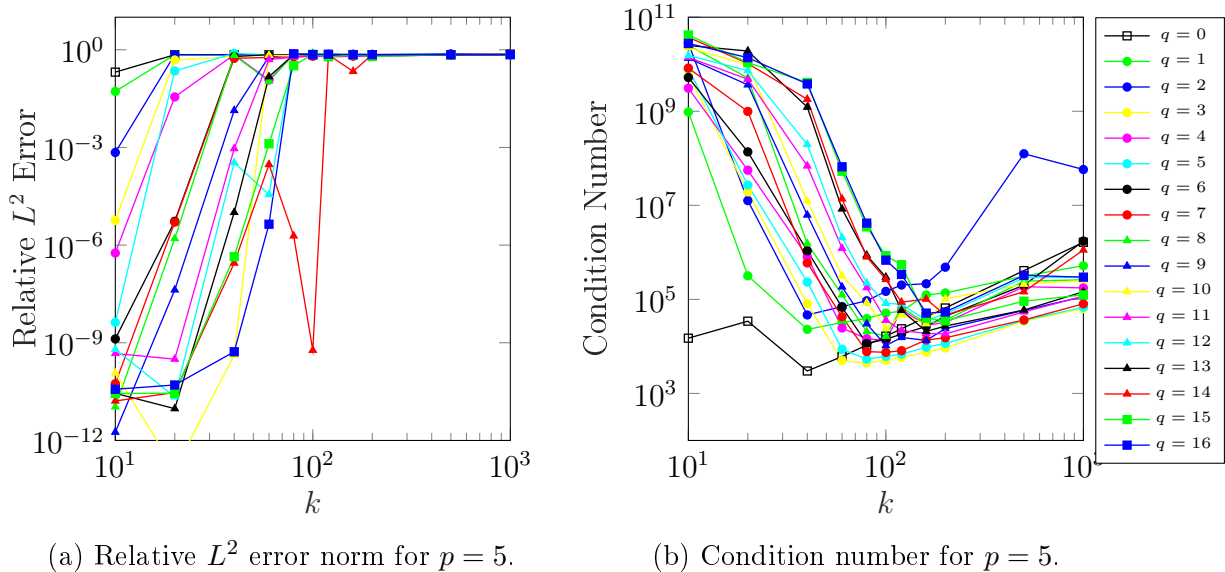


Figure 5.33: Duct example: Wave study for a fixed mesh. Comparison between plane-wave enriched and non-enriched collocation methods. The mesh has 64 elements.  $p = 5$

Finally, in Figure 5.34, we show the convergence study in terms of the  $L^2$  error norm vs. the Degree of Freedom density, i.e. the number of DOFs per wave length,  $N_\lambda = \frac{4\pi^2 DOF}{k^2}$  (with  $\sqrt{N_\lambda}$  being the DOF density in one direction). The results are given for  $p = 4$  and  $k = 10$  and 120. Both enriched and un-enriched schemes can be compared. It can be seen that for  $k = 120$  and  $N_\lambda \geq 6$ , for the same  $N_\lambda$ , a large number of enrichment functions need to be added ( $q \geq 12$ ) to see an improvement over the un-enriched scheme. For  $k = 10$  improvement in the range  $6 \leq N_\lambda \leq 10$  (typically used in acoustics analysis) is seen for  $q \geq 5$ .

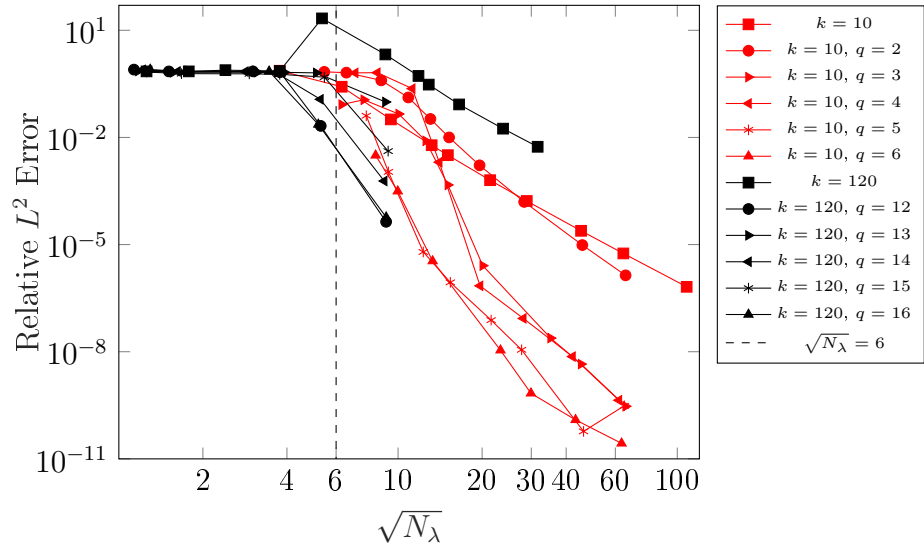


Figure 5.34: Duct example: Relative  $L^2$  error norm versus the DOF density  $N_\lambda$  for  $k = 10$  and  $k = 120$ , using  $p = 4$  and different numbers of enrichment functions.

### GHP-enrichment: convergence study for $k = 10$ and $m = 2$

Figures 5.35a, 5.36a and 5.37a show the convergence study in terms of the DOF for both the  $L^2$  error norm and the condition number, using  $p = 3, 4$  and  $5$  with  $q$  from  $0$  to  $16$ . In all the simulations, generalized harmonic polynomial enrichment is employed. The wave number  $k$  is fixed to  $10$  and  $m = 2$ . In all plots, a significant improvement between the enriched and non-enriched approach is seen. Interestingly, the error curves for  $q > 5$  are close to each other, meaning that adding more enrichment functions does not improve the overall error. Another important observation is that the condition number for GHP-enriched IGA-C is significantly higher than the condition number in PW-enriched IGA-C, as shown in Figures 5.35b, 5.36b and 5.37b.

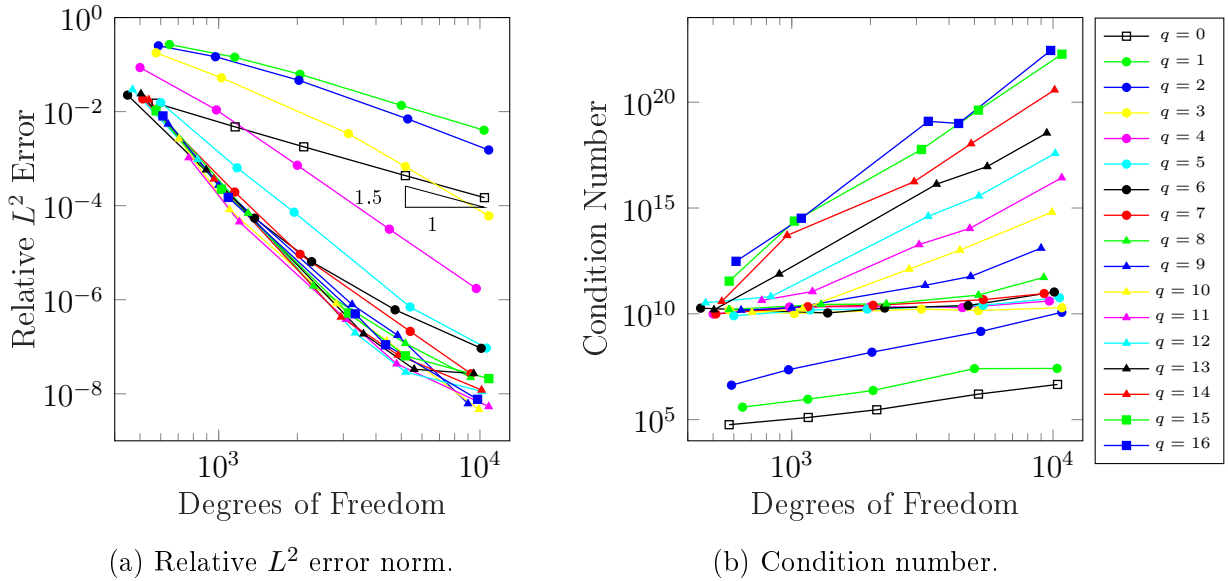
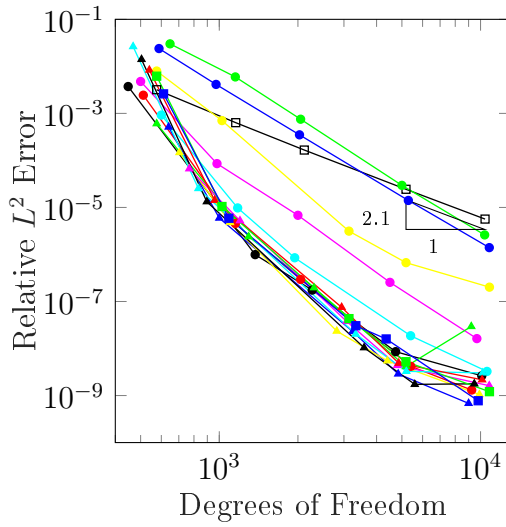


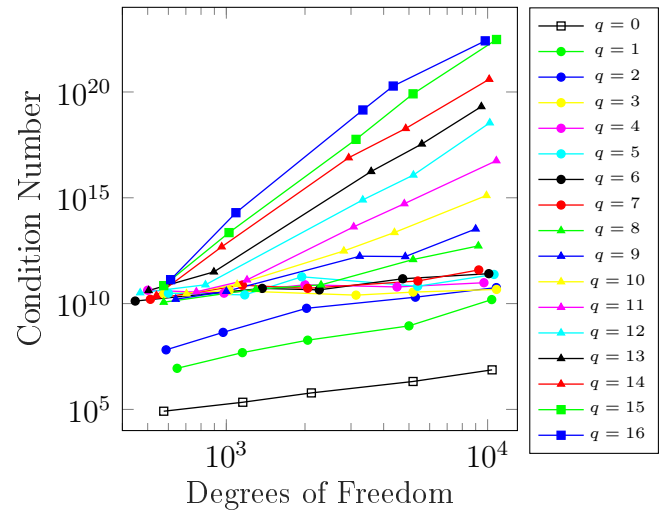
Figure 5.35: The duct example: Relative  $L^2$  error norm and Condition number study for  $p = 3$ ,  $k = 10$  and  $m = 2$  and varying number of GHP-enrichment functions.

### GHP-enrichment: convergence study for $k = 40$ and $m = 12$

Figures 5.38a, 5.39a and 5.40a show the convergence study in terms of the DOF for both the  $L^2$  error norm and the condition number, using  $p = 3, 4$  and  $5$  with  $q$  from  $0$  to  $16$ . In all the simulations, generalized harmonic polynomial enrichment is employed. The wave number  $k$  is fixed to  $40$  and  $m = 12$ . As it can be seen in the figures, for  $k = 40$ , the GHP-enrichment performs very poorly. In all three figures, the error in the non-enriched formulation is significantly lower compared to the GHP-enriched IGA-C, converging asymptotically in the entire range, while the enriched formulation requires much more degrees of freedom even to start converging.

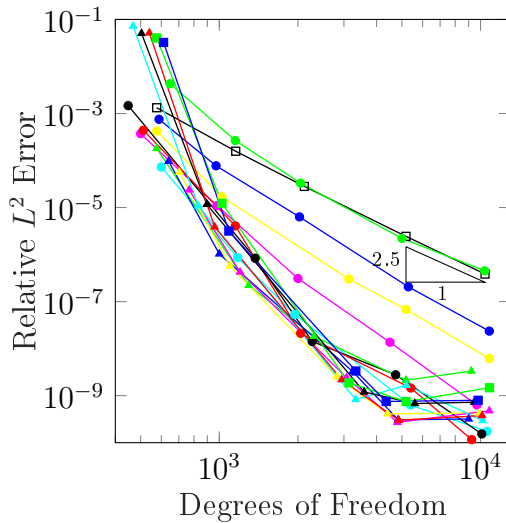


(a) Relative  $L^2$  error norm.

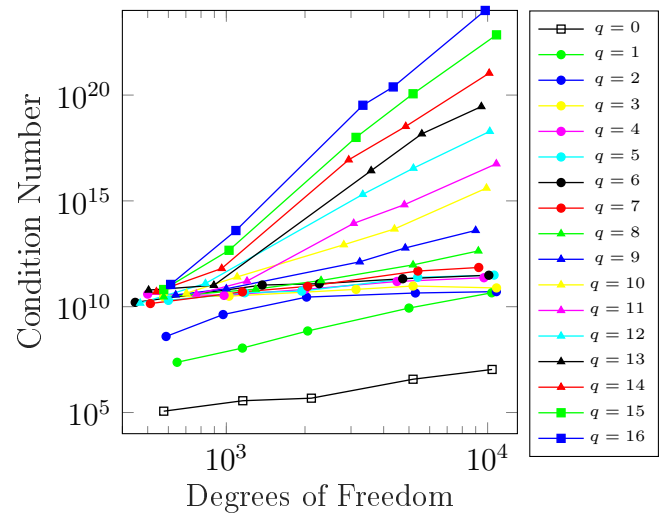


(b) Condition number.

Figure 5.36: The duct example: Relative  $L^2$  error norm and Condition number study for  $p = 4$ ,  $k = 10$  and  $m = 2$  and varying number of GHP-enrichment functions.



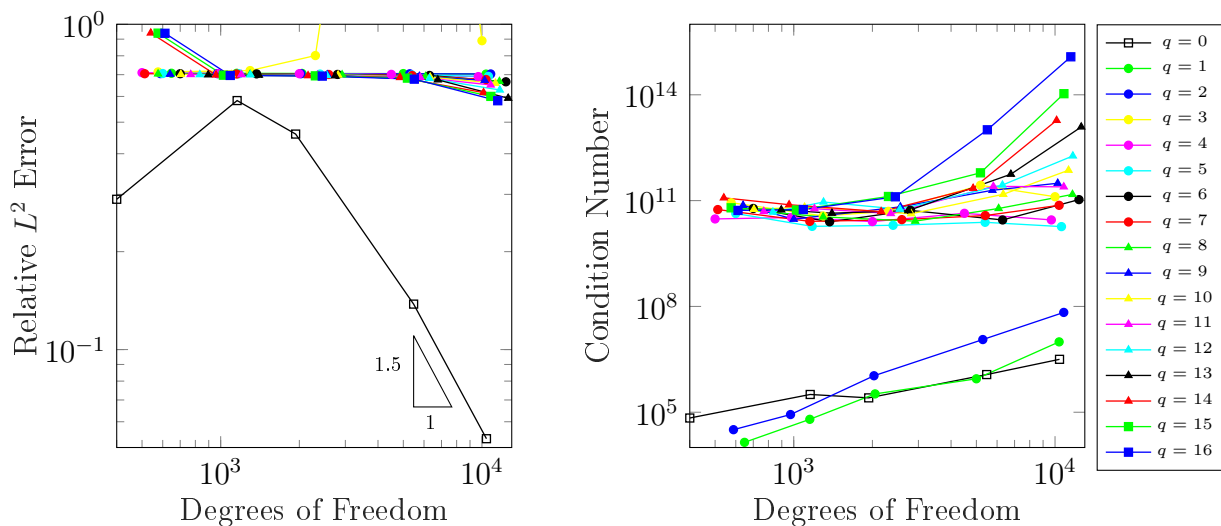
(a) Relative  $L^2$  error norm.



(b) Condition number.

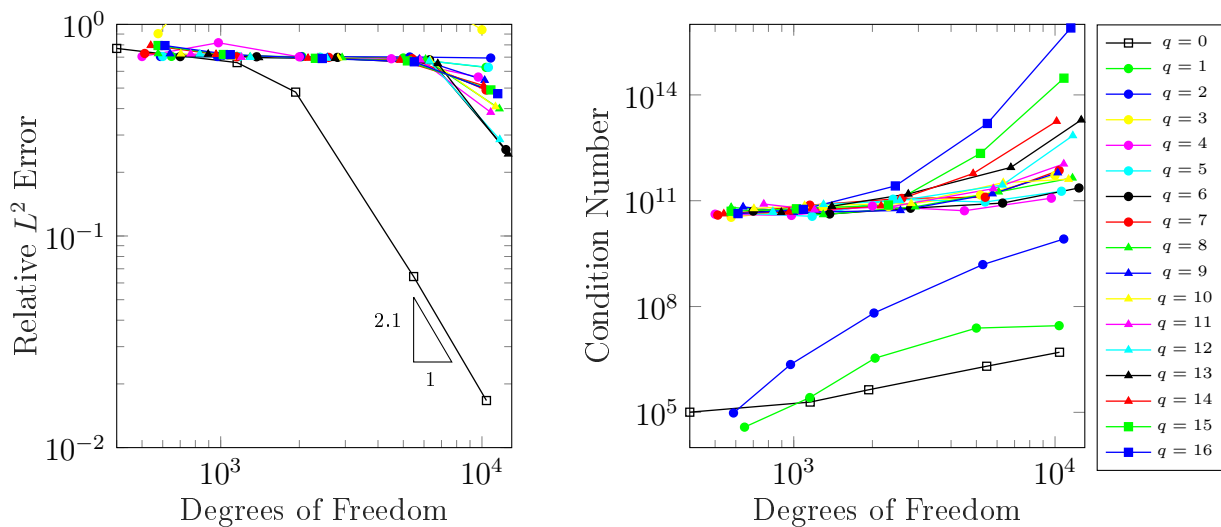
Figure 5.37: The duct example: Relative  $L^2$  error norm and Condition number study for  $p = 5$ ,  $k = 10$  and  $m = 2$  and varying number of GHP-enrichment functions.





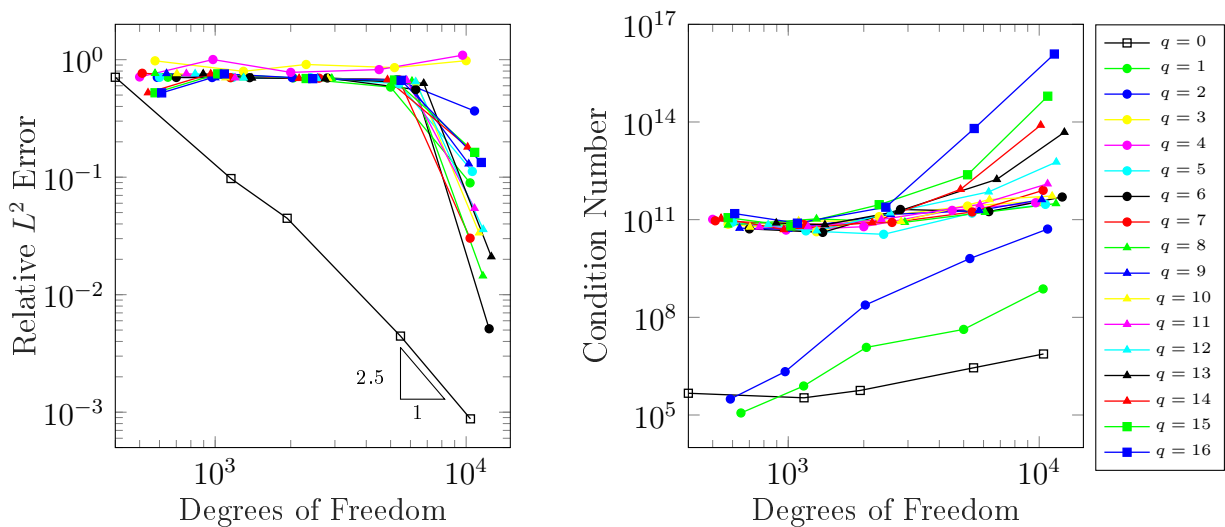
(a) Relative  $L^2$  error norm for  $p = 3$  and (b) Condition number for  $p = 3$  and  $k = 40$ .  $k = 40$ .

Figure 5.38: The duct example: Relative  $L^2$  error norm and Condition number study for  $p = 3$ ,  $k = 40$  and  $m = 12$ , varying number of GHP-enrichment functions.



(a) Relative  $L^2$  error norm for  $p = 4$  and (b) Condition number for  $p = 4$  and  $k = 40$ .  $k = 40$ .

Figure 5.39: The duct example: Relative  $L^2$  error norm and Condition number study for  $p = 4$ ,  $k = 40$  and  $m = 12$ , varying number of GHP-enrichment functions.



(a) Relative  $L^2$  error norm for  $p = 5$  and  $k = 40$ .  
 (b) Condition number for  $p = 5$  and  $k = 40$ .

Figure 5.40: The duct example: Relative  $L^2$  error norm and Condition number study for  $p = 5$ ,  $k = 40$  and  $m = 12$ , varying number of GHP-enrichment functions.

## GHP-enrichment: wave number study

Figures 5.43a and 5.43b show the convergence study in terms of the wave number for both the  $L^2$  error norm and the condition number, using  $p = 3$ ,  $p = 4$  and  $p = 5$  with  $q$  from 0 to 16. In all simulations, the generalized harmonic polynomial enrichment is employed. As before, the value chosen for  $m$  is the highest natural number that allows propagation. The mesh is fixed to  $8 \times 8$  elements. The behaviour of GHP-enrichment in figure 5.43 is similar to PW-enrichment shown in Figure 5.33. Interestingly, the range of  $k$  where GHP-enrichment improves the error is much smaller than the one in PW-enrichment, i.e. for  $k > 30$  there is no improvement in the error in GHP-enriched IGA-C, even when a large number of enrichment functions is added, while in Figure 5.33, the improvement in the error for PW-enriched IGA-C was observed for  $k$  up to 100. The condition number in GHP-enriched IGA-C is also higher in comparison with PW-enrichment.

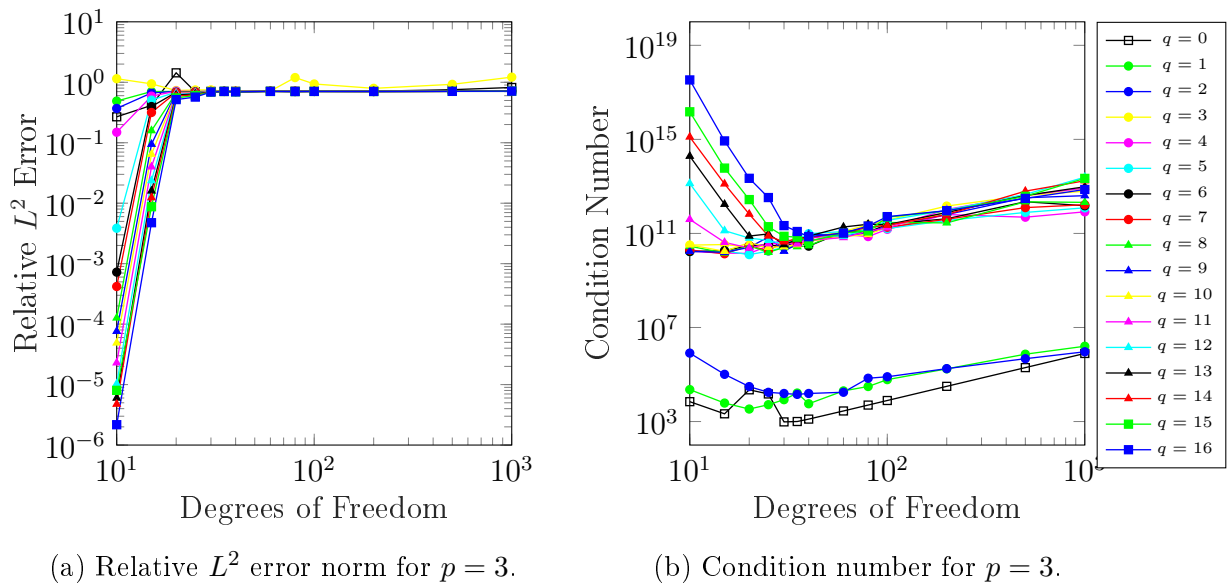
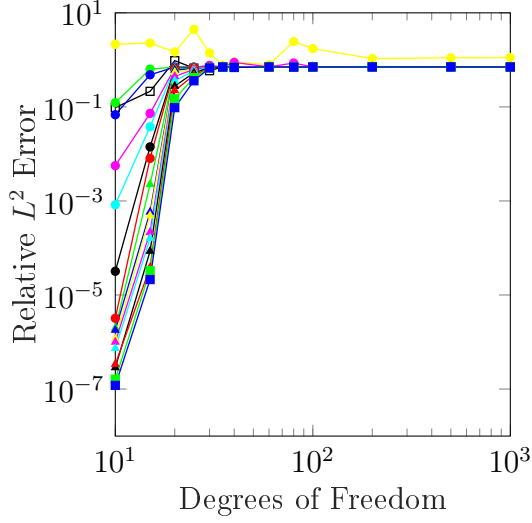
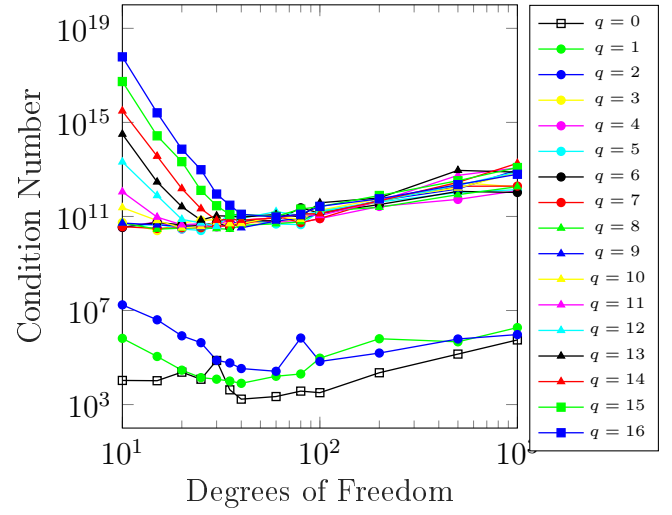


Figure 5.41: Duct example: GHP-study for a fixed mesh. Comparison between GHP-enriched and non-enriched collocation methods. The mesh has 64 elements.  $p = 3$

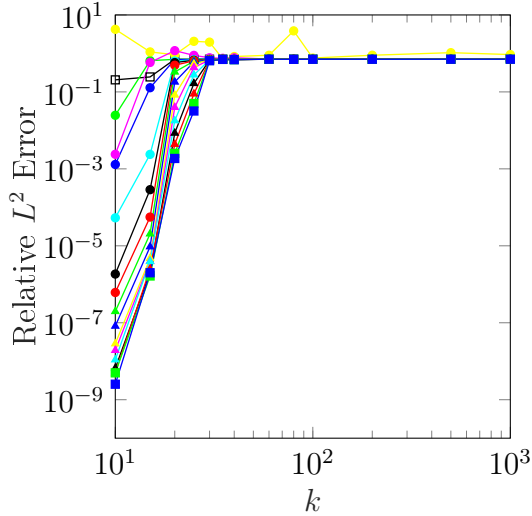


(a) Relative  $L^2$  error norm for  $p = 4$ .

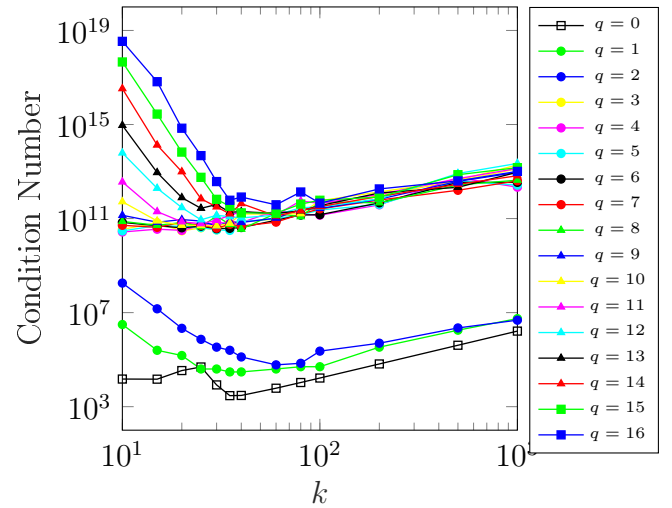


(b) Condition number for  $p = 4$ .

Figure 5.42: Duct example: GHP-study for a fixed mesh. Comparison between GHP-enriched and non-enriched collocation methods. The mesh has 64 elements.  $p = 4$



(a) Relative  $L^2$  error norm for  $p = 5$ .



(b) Condition number for  $p = 5$ .

Figure 5.43: Duct example: GHP-study for a fixed mesh. Comparison between GHP-enriched and non-enriched collocation methods. The mesh has 64 elements.  $p = 5$

## 5.4. Spinning wave propagation

In this example, we considered a spinning wave propagation problem. The geometry of computational domain consists of two circular cylinders of radii  $R_i$  (with boundary denoted as  $\Gamma_1$ ) and  $R_e$  (with boundary denoted as  $\Gamma_2$ ), centered at the origin, as shown in Figure 5.44a. The geometry consists of four NURBS patches (Figure 5.44b) with control points given by table A.3 taken from table A.9 of [77]. The inter-patch continuity of solution is imposed as described in subsection 4.3.4.

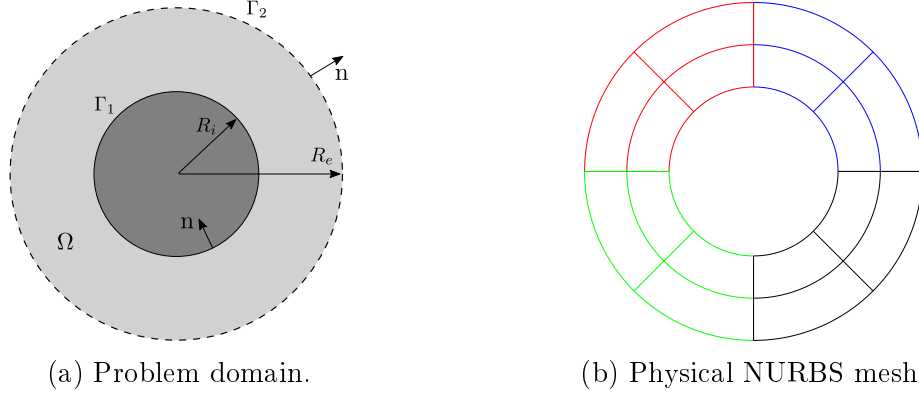


Figure 5.44: Spinning wave example: (a) Schematic of the exterior acoustic spinning wave propagation problem.  $\Omega$  represent the problem domain,  $\Gamma_1$  and  $\Gamma_2$  are the Robin boundaries. The normal is denoted by  $\mathbf{n}$ . (b) Multipatch mesh in physical space built with NURBS.

The exterior acoustic spinning wave propagation problem is stated as  
*Find  $u$  such that*

$$\Delta u + k^2 u = 0, \quad \text{in } \Omega \quad (5.10)$$

$$\frac{\partial u}{\partial \mathbf{n}} - iku = f_1, \quad \text{on } \Gamma_1 \quad (5.11)$$

$$\frac{\partial u}{\partial \mathbf{n}} - iku = f_2, \quad \text{on } \Gamma_2 \quad (5.12)$$

In the present study, we considered  $R_i = 1$  and  $R_e = 2$ , and Robin boundary condition on both boundaries ( $\Gamma_1$  and  $\Gamma_2$ ) with functions  $f_1$  and  $f_2$  calculated from the analytical solution. The analytical solution is presented in [30],

$$u^{\text{exact}}(r, \theta) = H_m^{(2)}(kr)^{-im\theta}, \quad (5.13)$$

where  $H_m^{(2)}$  is Hankel function of the second kind of order  $m$ , which is also the number of waves in the polar direction, and  $k$  is the wave number.

The wave will propagate with decay rate of order  $1/\sqrt{r}$ , where  $r \in [R_i, \infty)$ , if  $m < kR_i$ . On the other hand, if  $m > kR_i$ , the wave will be evanescent and it will decay with a higher rate. In this study, two wave numbers are considered,  $k = 20$  and  $k = 40$  with  $m = 10$  and  $m = 30$  for the propagating mode respectively, and  $m = 22$  and  $m = 42$  for the evanescent mode. The real and the imaginary parts of the solution for  $k = 40$  and  $m = 30$  are shown in Figure 5.45.

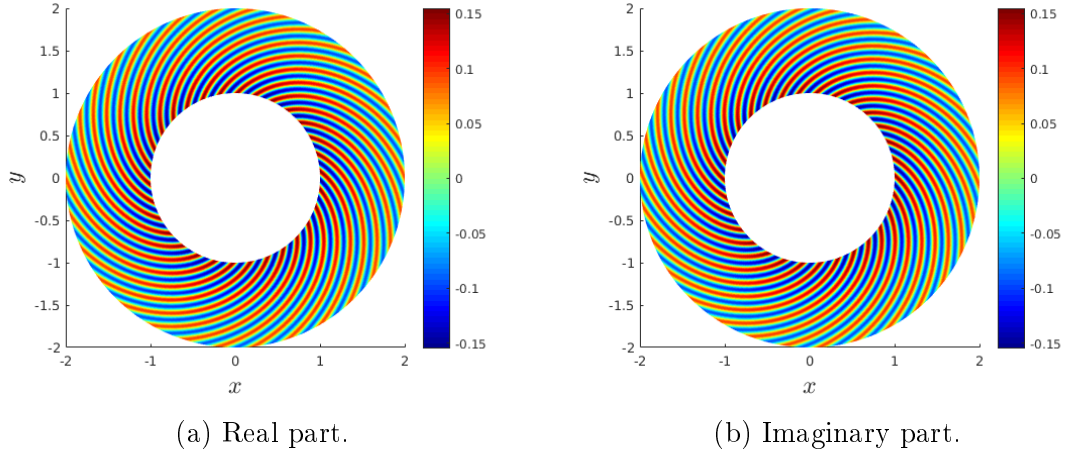


Figure 5.45: Analytical solution of the spinning wave propagation problem with  $k = 40$  and  $m = 30$ .

### Spinning wave propagation: PW-enrichment

Figures 5.46, 5.47, 5.48 and 5.49 show the convergence study for both the  $L^2$  error norm and the condition number vs DOFs, using  $p = 3$  and  $q$  from 8 to 16. In all simulations, PW-enrichment is employed. In Figure 5.46 and 5.48 the sound wave is in propagating mode since  $m < kR_i$ . In Figure 5.47 and 5.49 the sound wave is evanescent. In all plots, enriched solutions show lower error in comparison with non-enriched IGA-C, but interestingly, a significant advantage of enrichment is seen only on fine meshes.

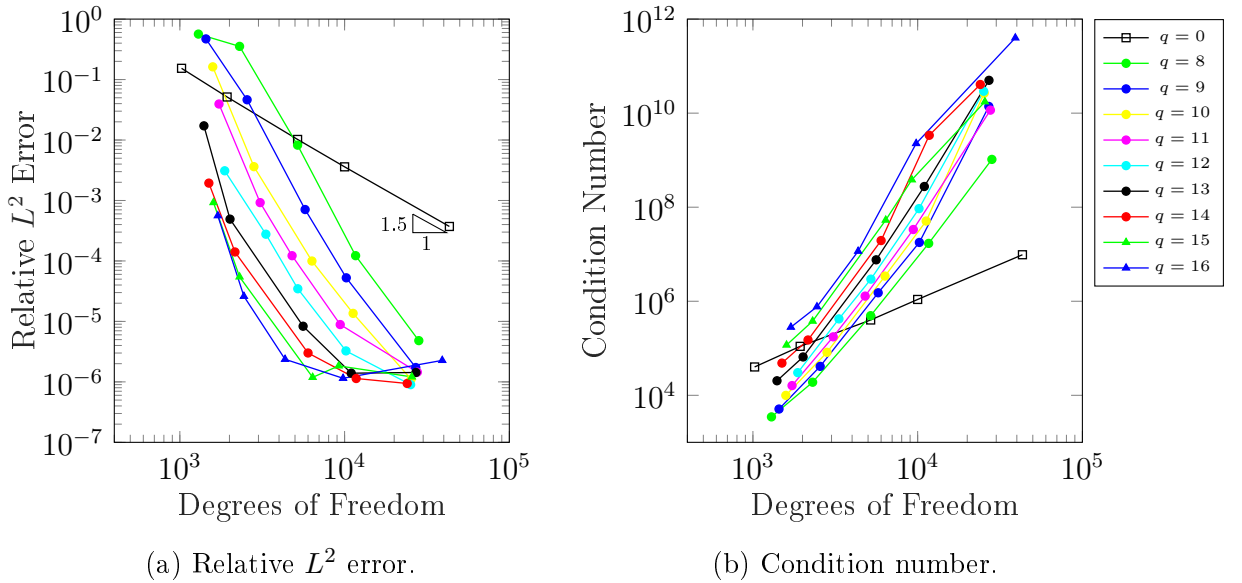


Figure 5.46: Spinning wave example: Relative  $L^2$  error norm and condition number study for  $p = 3$ ,  $k = 20$  and  $m = 10$  for various number of PW enrichment functions.

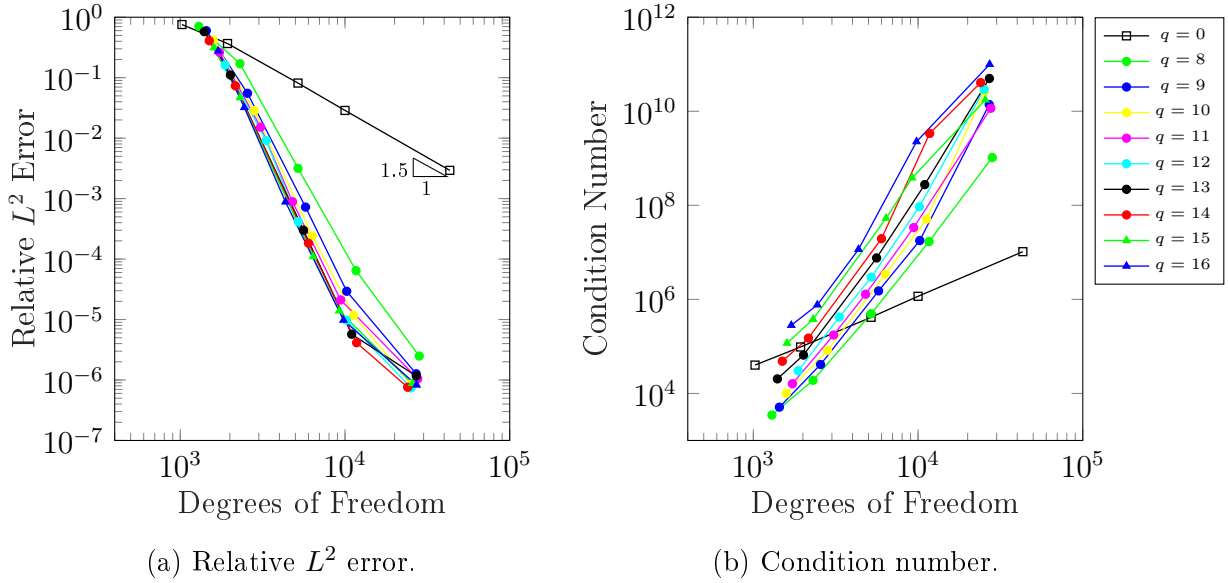


Figure 5.47: Spinning wave example: Relative  $L^2$  error norm and condition number study for  $p = 3$ ,  $k = 20$  and  $m = 22$  for various number of PW enrichment functions.

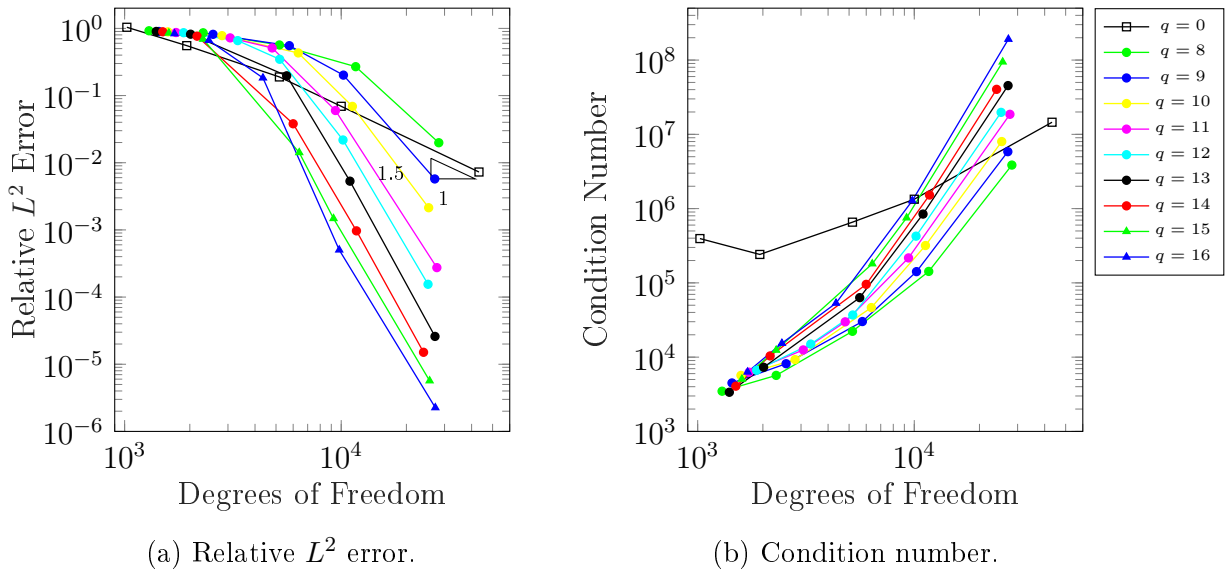
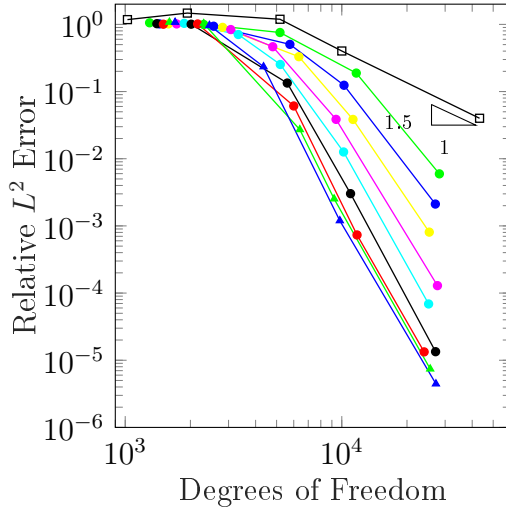


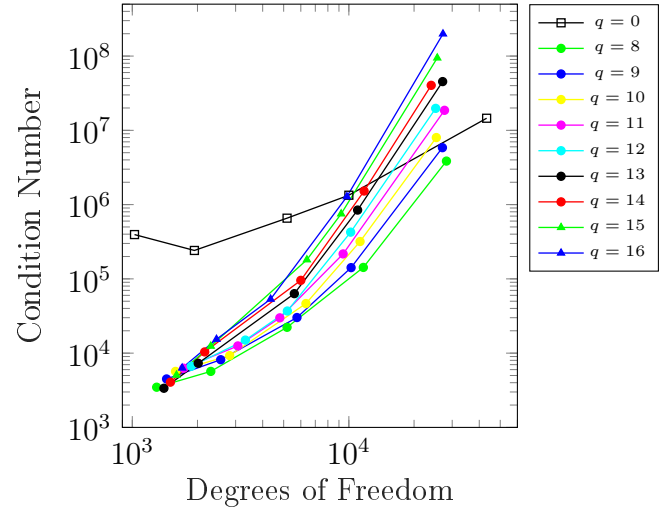
Figure 5.48: Spinning wave example: Relative  $L^2$  error norm and condition number study for  $p = 3$ ,  $k = 40$  and  $m = 30$ , varying number of PW-enrichment functions.

### Spinning wave propagation: GHP-enrichment

Figures 5.50, 5.51, 5.52 and 5.53 show the convergence study in terms of the DOF for both the  $L^2$  error norm and the condition number, using  $p = 3$  and  $q$  from 8 to 16. In all simulations, the generalized harmonic polynomial enrichment is employed. In all cases, the GHP-enrichment performs quite poorly. As it is seen in the figures, the GHP-enriched IGA-C not only does not bring any improvement in the error, but it requires much more DOFs in comparison with the non-enriched IGA-C to overcome the pollution error and begin to converge. Note, that in both last examples in this subsection  $k = 40$ , but the error of the GHP-enriched solutions for  $m = 42$  is up to one order of magnitude worse than for  $m = 30$ .

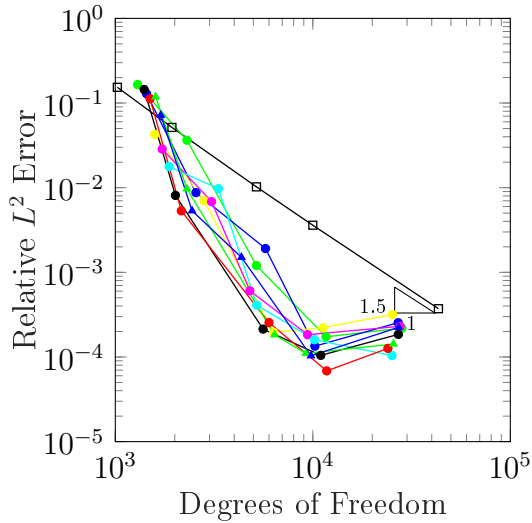


(a) Relative  $L^2$  error.

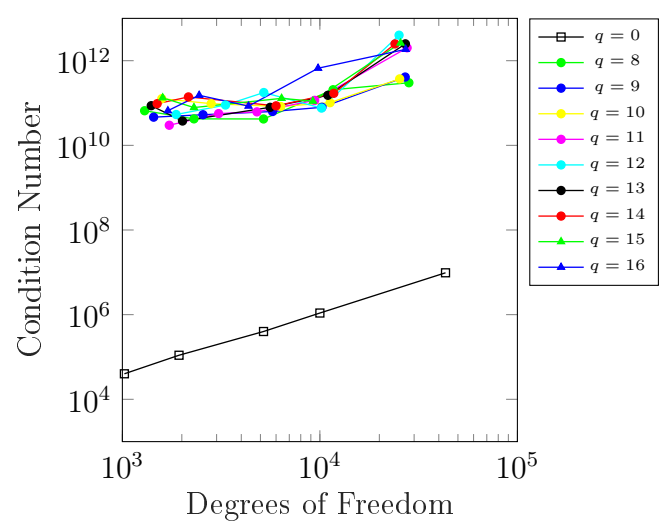


(b) Condition number.

Figure 5.49: Spinning wave example: Relative  $L^2$  error norm and condition number study for  $p = 3$ ,  $k = 40$  and  $m = 42$ , varying number of PW-enrichment functions.



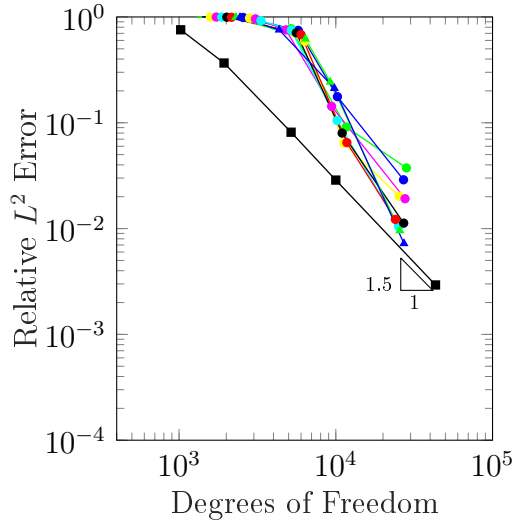
(a) Relative  $L^2$  error.



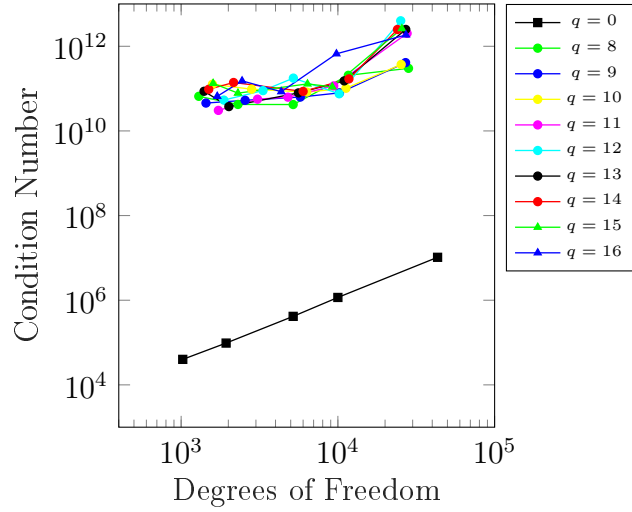
(b) Condition number.

Figure 5.50: Spinning wave example: Relative  $L^2$  error norm and condition number study for  $p = 3$ ,  $k = 20$  and  $m = 10$ . Comparison between collocation and GHP enriched collocation.



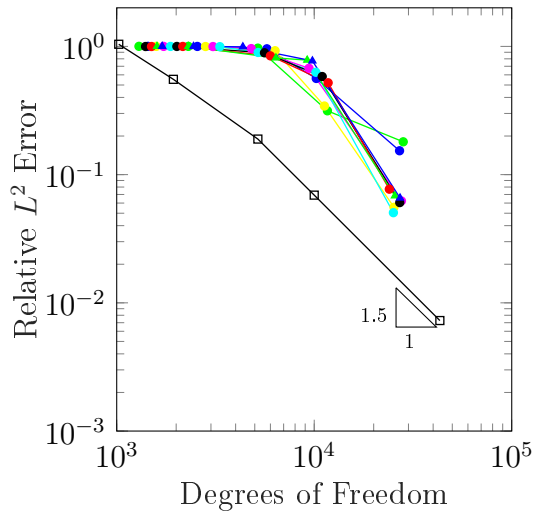


(a) Relative  $L^2$  error.

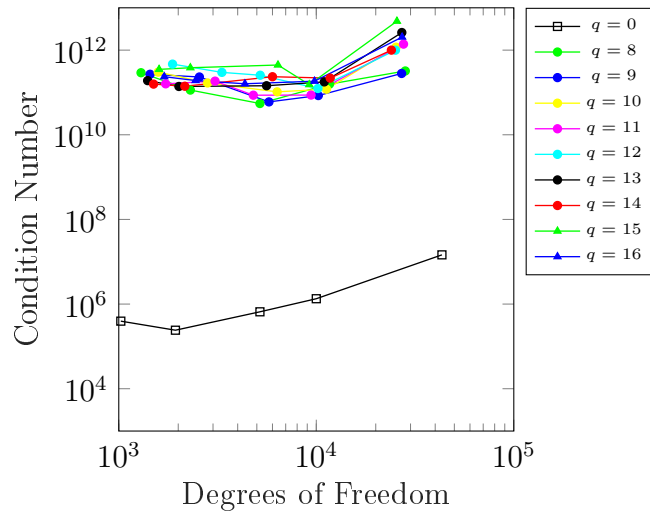


(b) Condition number.

Figure 5.51: Spinning wave example: Relative  $L^2$  error norm and condition number study for  $p = 3$ ,  $k = 20$  and  $m = 22$ . Comparison between collocation and GHP enriched collocation.

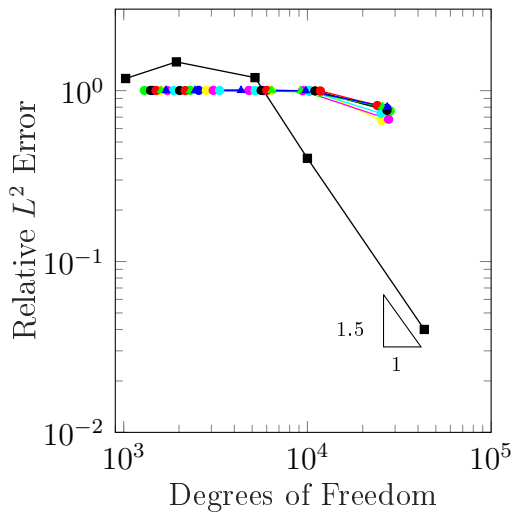


(a) Relative  $L^2$  error.

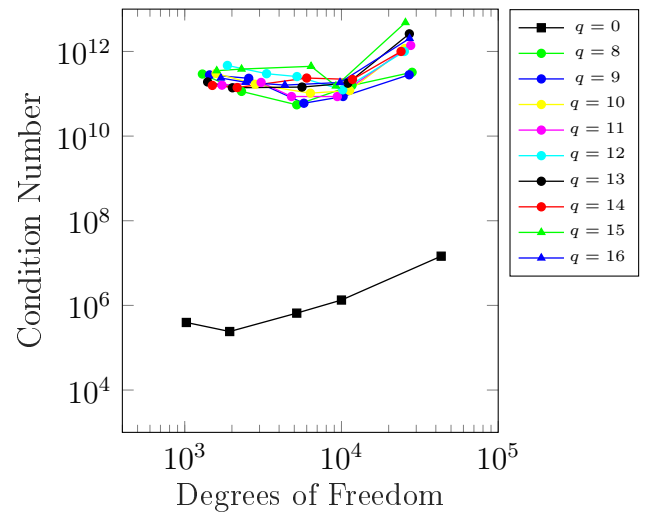


(b) Condition number.

Figure 5.52: Spinning wave example: Relative  $L^2$  error norm and condition number study for  $p = 3$ ,  $k = 40$  and  $m = 30$ , varying number of GHP-enrichment functions.



(a) Relative  $L^2$  error.



(b) Condition number.

Figure 5.53: Spinning wave example: Relative  $L^2$  error norm and condition number study for  $p = 3$ ,  $k = 40$  and  $m = 42$ , varying number of GHP-enrichment functions.

## 5.5. Plane wave scattered by cylinder

Another benchmark problem in the time-harmonic acoustic analysis is the problem corresponding to an incident harmonic plane-wave  $u^{inc}$  scattered by a sound-hard cylinder. Assuming that the incident plane-wave is travelling along the direction  $\mathbf{e}_1$ , it can be expressed in polar coordinates  $(r, \theta)$  as

$$u^{inc}(r, \theta) = u_0 \exp(ikr \cos \theta), \quad (5.14)$$

where  $u_0$  is the magnitude of the wave (for simplicity,  $u_0 = 1$ ), and  $k$  is the wave number. Then the analytical solution for the scattered wave is given by

$$u^{exact}(r, \theta) = - \sum_{n=0}^{\infty} i^n \varepsilon_n \frac{J'_n(kR_i)}{H'_n(kR_i)} H_n(kr) \cos(n\theta), \quad (5.15)$$

where  $R_i$  is the radius of the cylinder,  $H_n^{(1)}$  is the Hankel function of the first kind,  $J_n$  is the Bessel function of the first kind,  $k$  is the wave number, and the Jacobi symbol is defined as

$$\varepsilon_n = \begin{cases} 1, & n = 0 \\ 2, & n \neq 0 \end{cases} \quad (5.16)$$

Equation (5.15) was taken from [9] and is a well-known solution of a wave scattering in an infinite domain. In domain-type methods, the infinite domain is truncated by a fictitious surface (cylinder of radius  $R_e$ ), where Absorbing Boundary Condition is prescribed, and therefore the resulting solution contains an additional boundary truncation error. Since the focus of this paper is on enrichment and not the ABC error, we consider the following Boundary Value Problem:

*Find  $u$  such that*

$$\Delta u + k^2 u = 0, \quad \text{in } \Omega \quad (5.17)$$

$$\frac{\partial u}{\partial n} = f_1, \quad \text{on } \Gamma_1 \quad (5.18)$$

$$\frac{\partial u}{\partial n} - iku = f_2, \quad \text{on } \Gamma_2 \quad (5.19)$$

where functions  $f_1$  and  $f_2$  are derived from a series (eq. (5.15)) with 80 terms. The domain  $\Omega$  and its NURBS parameterization are shown in Figure 5.44. In such formulation, both the series truncation and the boundary truncation errors are excluded, and the numerical solution  $u^h$  of Problem (5.17)-(5.19) converges to its analytical solution. The real and the imaginary parts of the analytical solution for  $k = 40$  are shown in Figure 5.54.

Figures 5.55a, 5.57a, 5.56a, 5.58a show the convergent study in terms of relative  $L^2$  error norm vs the DOF, using  $p = 3$ ,  $k = 20$ ,  $k = 40$  and  $q$  from 8 to 16. It can be seen that the PW-enriched IGA-C performs significantly better than the GHP-enriched IGA-C, bringing up to four order of magnitude improvement in the error on fine meshes, while GHP-enrichment shows worse error than non-enriched IGA-C for all mesh sizes and values of  $q$ .

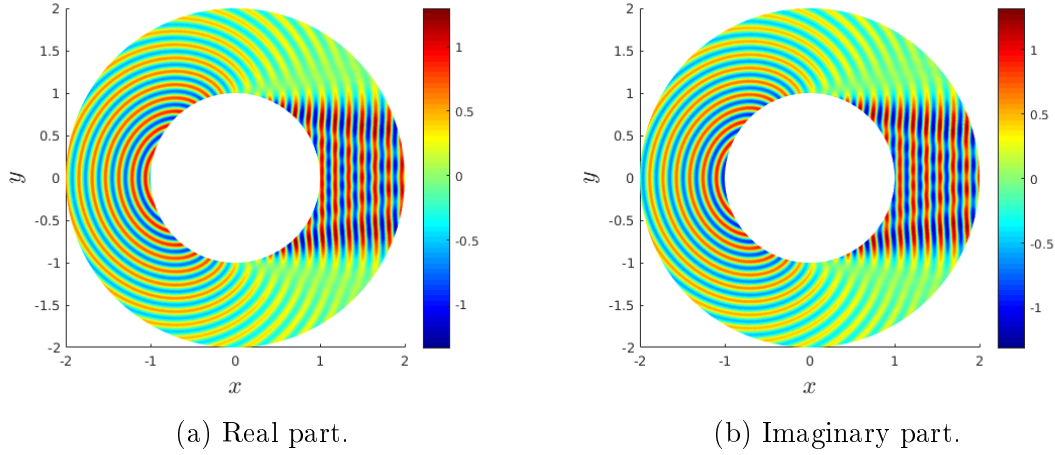


Figure 5.54: Analytical solution of wave scattered by a cylinder problem with  $k = 40$ .

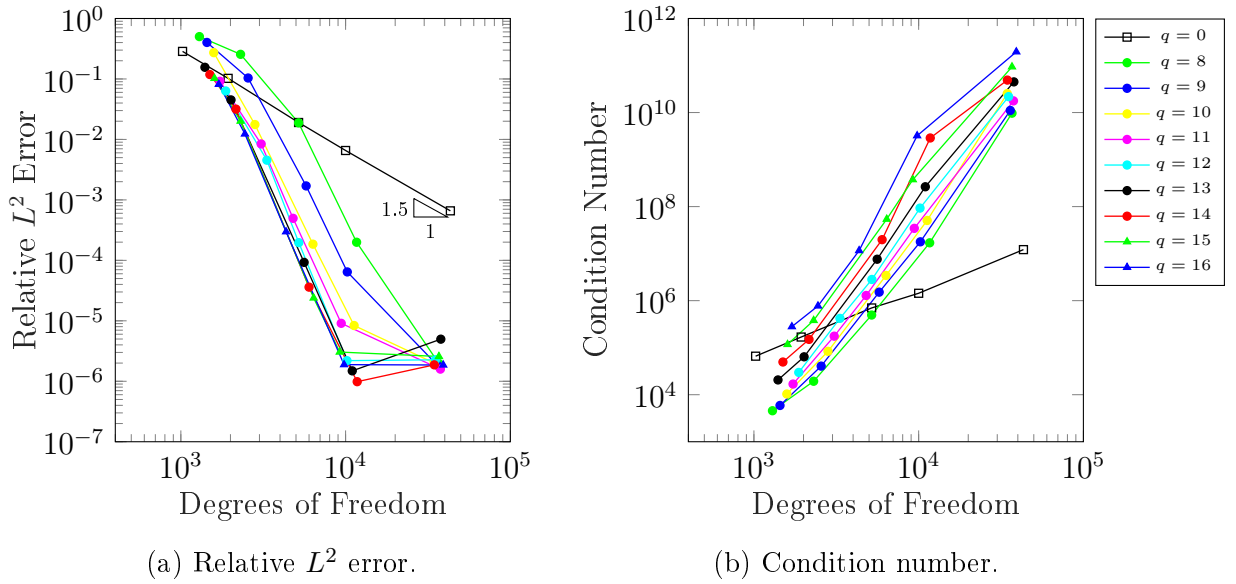


Figure 5.55: Cylinder scattered example: Relative  $L^2$  error norm and condition number study for  $p = 3$ ,  $k = 20$ . Comparison between collocation and PW enriched collocation.

### Plane wave scattered by a cylinder: PW-enrichment

### Plane wave scattered by a cylinder: GHP-enrichment

Figures 5.57 and 5.58 show the convergent study in terms of the DOF for both the  $L^2$  error norm and the condition number, using  $p = 3$  and  $q$  from 8 to 16. In all the simulations generalized harmonic polynomial enrichment is employed.

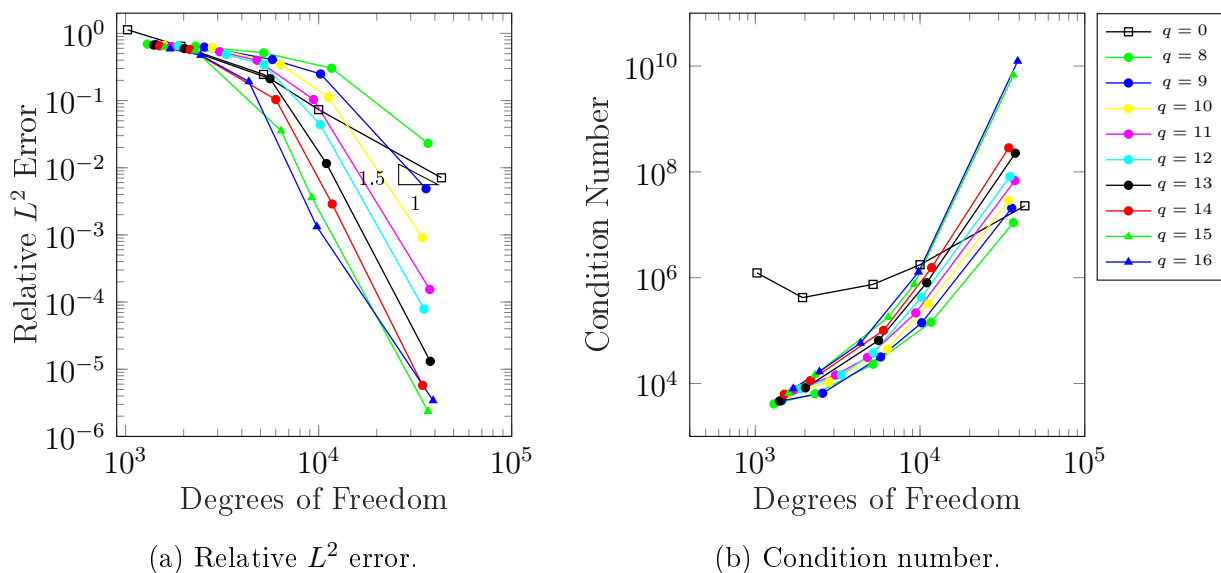


Figure 5.56: Cylinder scattered example: Relative  $L^2$  error norm and condition number study for  $p = 3$ ,  $k = 40$ . Comparison between collocation and PW enriched collocation.

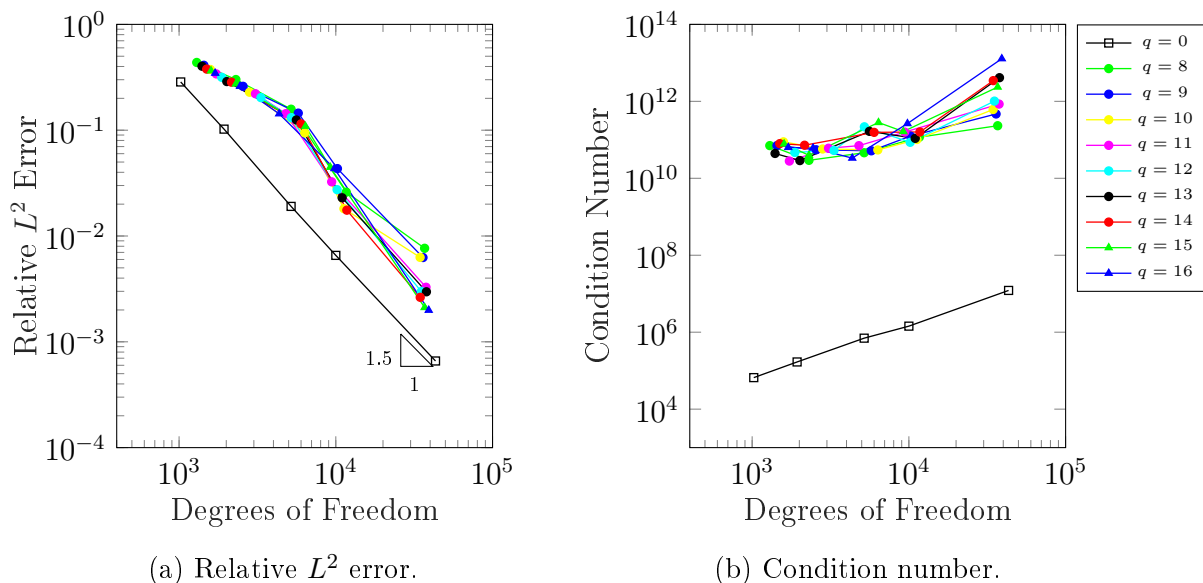


Figure 5.57: Cylinder scattered example: Relative  $L^2$  error norm and condition number study for  $p = 3$ ,  $k = 40$ . Comparison between collocation and GHP enriched collocation.

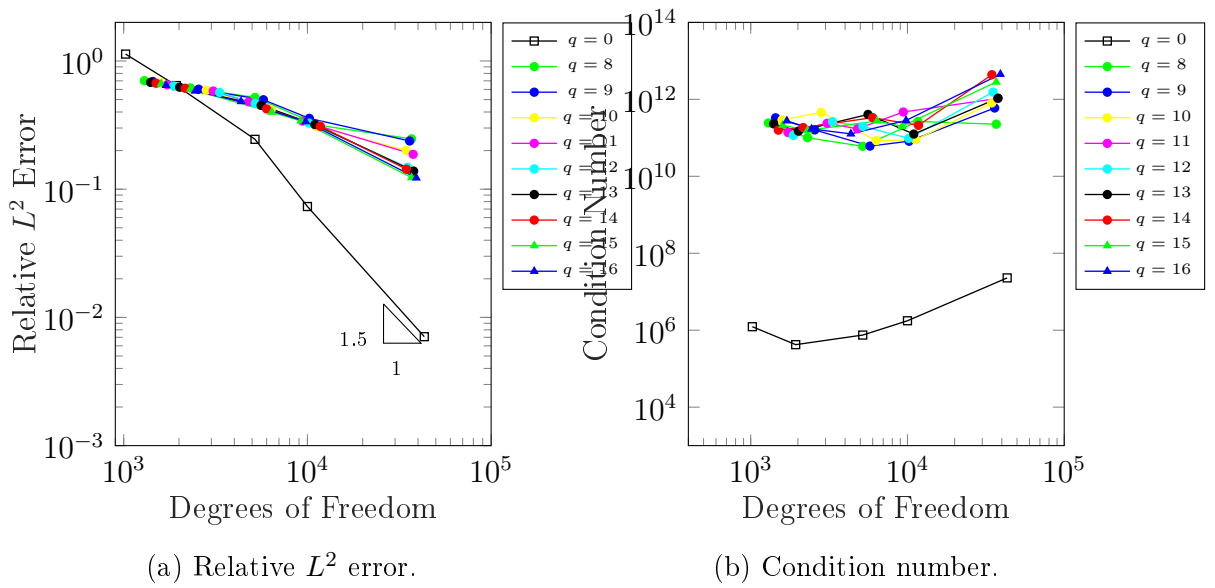


Figure 5.58: Cylinder scattered example: Relative  $L^2$  error norm and condition number study for  $p = 3$ ,  $k = 40$ . Comparison between collocation and GHP enriched collocation.

## 5.6. Star geometry

As a final example, we studied the numerical results for the Helmholtz equation on a star-shaped geometry with a prescribed analytical solution. A five-patch mesh is employed for this example, using the same patch coupling method explained in subsection 4.3.4. The control points and knot vector of each patch are given in table A.4 taken from table A.4 of [78].

The following boundary value problem is considered

Find  $u$  such that

$$\Delta u + k^2 u = 0, \quad \text{in } \Omega \quad (5.20)$$

$$\frac{\partial u}{\partial n} = f_1, \quad \text{on } \Gamma_N \quad (5.21)$$

$$\frac{\partial u}{\partial n} - iku = f_2, \quad \text{on } \Gamma_R \quad (5.22)$$

Like in [79], the prescribed analytical solution is given by:

$$u^{\text{exact}}(\mathbf{x}) = H_0^{(1)}(kr_1(\mathbf{x})) + H_0^{(1)}(kr_2(\mathbf{x})), \quad (5.23)$$

where  $r_1 = |\mathbf{x} - \mathbf{x}_1|$  and  $r_2 = |\mathbf{x} - \mathbf{x}_2|$ , with  $\mathbf{x}_1$  and  $\mathbf{x}_2$  inside the interior of the star. In this paper, we used  $\mathbf{x}_1 = (0, 1/2)$  and  $\mathbf{x}_2 = (0, -1/2)$ . Functions  $f_1$  and  $f_2$  are calculated from the analytical solution. The real and the imaginary parts of the analytical solution for  $k = 20$  are shown in figure 5.59.

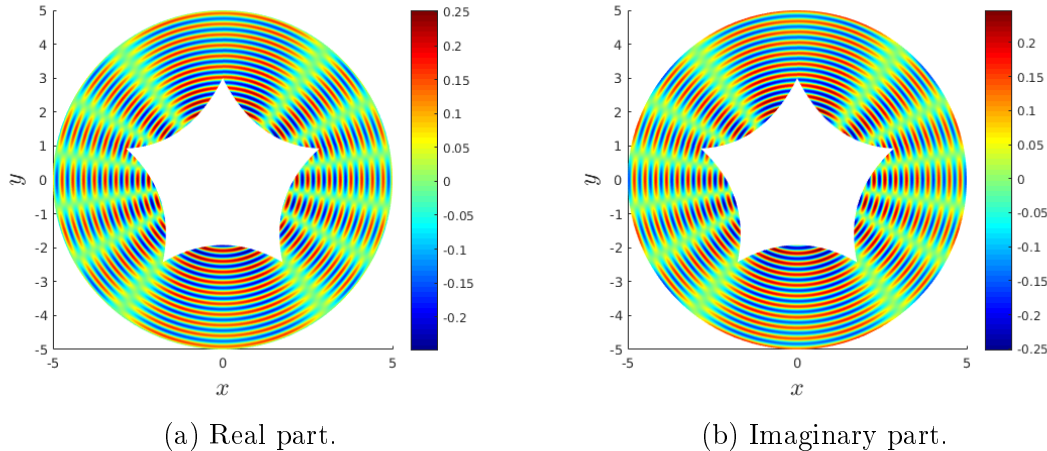


Figure 5.59: Analytical solution of sound hard star problem with  $k = 20$ .

Figure 5.60 shows the convergence study in terms of the DOF for both the  $L^2$  error norm and the condition number, using  $p = 3$  and  $q$  from 8 to 16. In all the simulations, plane-wave enrichment is employed.

In Figure 5.61 the same study is repeated with the GHP-enrichment. Both types of enrichment bring significant improvement in the error compared to the non-enriched IGA-C.

Interestingly, the condition number in the PW-enriched IGA-C is smaller than in the non-enriched case, while GHP-enrichment leads to much worse conditioning of the system matrix. Large condition number in the GHP-enriched IGA-C case seems to affect the error curves in Figure 5.60a, where the error does not decrease below the order of  $10^{-3}$ . Additionally, error curves for  $q \geq 8$  in Figure 5.60a are close to each other, indicating that adding more GHP-functions in the enriched basis does not bring any improvement, while dependence of the PW-enriched IGA-C error on the number of PW-functions is more pronounced in Figure 5.60a.

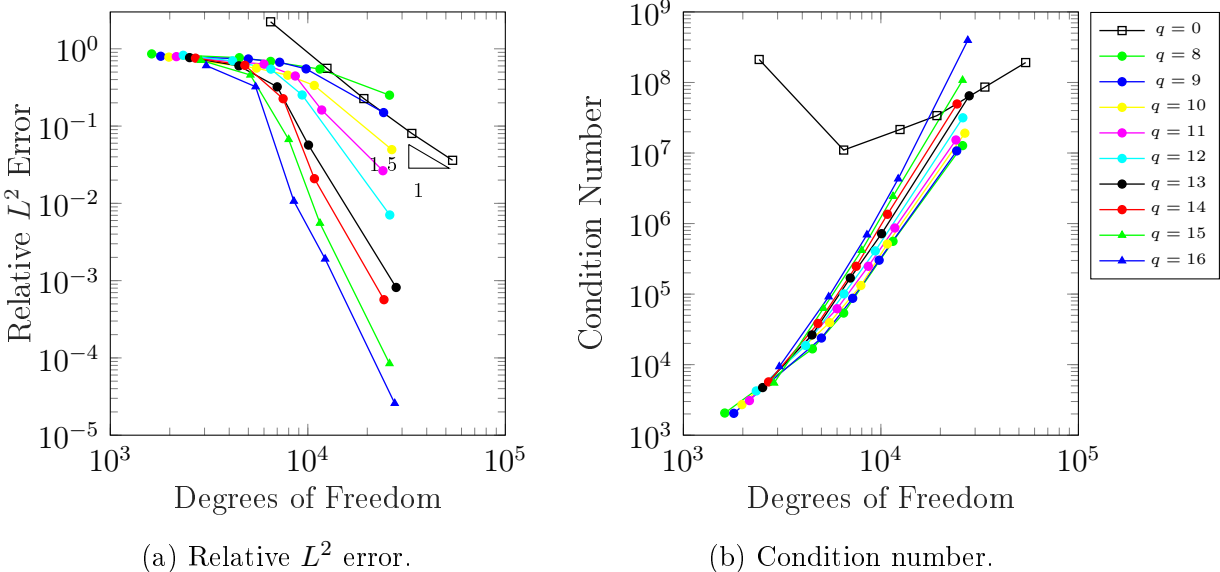


Figure 5.60: Star shape example, PW-enrichment: Relative  $L^2$  error norm and condition number study for  $p = 3$ ,  $k = 20$ , varying number of enrichment functions.

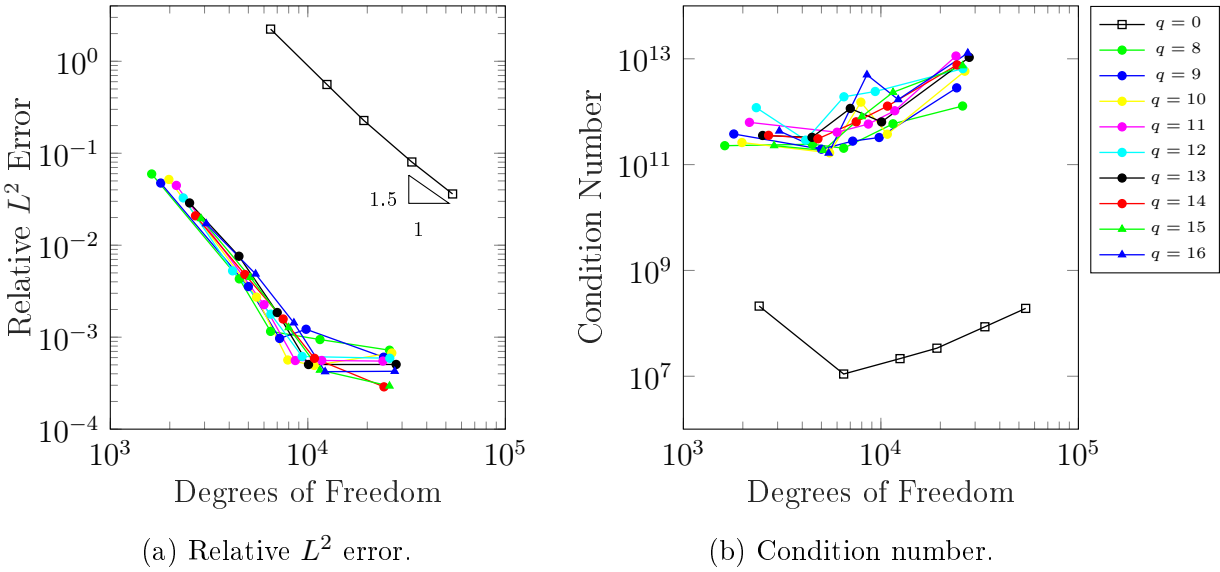


Figure 5.61: Star shape example, GHP-enrichment: Relative  $L^2$  error norm and condition number study for  $p = 3$ ,  $k = 20$ , varying number of enrichment functions.



# Chapter 6

## Conclusion

In this work, we showed the application of the Isogeometric Collocation (IGA-C), and Enriched Isogeometric Collocation method to 2D problems for the Helmholtz equation.

First, different collocation schemes were tested for the non-enriched IGA-C, namely, Greville abscissae (GA), Approximated Cauchy-Galerkin (ACG) and Superconvergent points (SC), showing that ACG collocations points are the best choice in terms of the error norm, convergence rate and ease of solving the resulting linear system. Still, in terms of the error per DOF, Galerkin IGA outperforms all of the collocation methods that were tested.

Two types of enrichment, namely Plane Wave (PW-) enrichment and Generalized Harmonic Polynomial (GHP-) enrichment, derived from the general form of the solution of the Helmholtz equation, were tested. In both cases, it was found that in order to achieve maximum efficiency of the method, the number of collocation points needs to be increased beyond the number of unknown degrees of freedom. The most efficient collocation strategy is to add  $q + 1$  points for PW-enrichment and  $q$  for GHP-enrichment, equidistantly between the Cauchy-Galerkin points (where  $q$  is the number of enrichment functions). The resulting non-square matrix must be solved in a least-square sense. In some cases, both types of enrichment improve the overall error by a few orders of magnitude.

The approximation with PW-enrichment is in general superior to that of GHP-enrichment and the condition number is also smaller, particularly when a large number of enrichments are used. However, for moderately small wave numbers, increasing the number of enrichments does not improve the approximation significantly. On the other hand, if the mesh (i.e. the number of NURBS in the basis before enrichment) is fixed, then the efficiency of enrichment deteriorates if the wave number  $k$  is increased. This result means that for larger values of  $k$ , more enrichment functions are needed to achieve the same accuracy.

Several multi-patch examples were solved successfully, for both, the standard IGA-C and enriched IGA-C. A simple and effective penalty factor technique was employed on the linear equation system, in order to solve in a least-square sense. However, finding precisely the optimal location of the collocation points for a given number and type of enrichment remains an open problem that can be addressed in a future work.

# Bibliography

- [1] Peter Risby Andersen, Vicente Cutanda Henríquez, and Niels Aage. Shape optimization of micro-acoustic devices including viscous and thermal losses. *Journal of Sound and Vibration*, 447:120 – 136, 2019.
- [2] Cosmin Anitescu, Yue Jia, Yongjie Jessica Zhang, and Timon Rabczuk. An isogeometric collocation method using superconvergent points. *Computer Methods in Applied Mechanics and Engineering*, 284:1073–1097, 2015.
- [3] Elena Atroshchenko, Satyendra Tomar, Gang Xu, and Stéphane P.A. Bordas. Weakening the tight coupling between geometry and simulation in isogeometric analysis: From sub- and super-geometric analysis to Geometry-Independent Field approximation (GIFT). *International Journal for Numerical Methods in Engineering*, 114(10):1131–1159, 2018.
- [4] F Auricchio, L Beirão Da Veiga, Thomas JR Hughes, A Reali, and G Sangalli. Isogeometric collocation for elastostatics and explicit dynamics. *Computer Methods in Applied Mechanics and Engineering*, 249:2–14, 2012.
- [5] F Auricchio, L Beirao Da Veiga, TJR Hughes, A\_ Reali, and G Sangalli. Isogeometric collocation methods. *Mathematical Models and Methods in Applied Sciences*, 20(11):2075–2107, 2010.
- [6] F Auricchio, L Beirao da Veiga, J Kiendl, C Lovadina, and A Reali. Locking-free isogeometric collocation methods for spatial Timoshenko rods. *Computer Methods in Applied Mechanics and Engineering*, 263:113–126, 2013.
- [7] I.M. Babuška and S. Sauter. Is the pollution effect of the FEM avoidable for the Helmholtz equation considering high wave numbers? *SIAM Journal on Numerical Analysis*, 34(6):2392–2423, 1997.
- [8] Ivo Babuška and Jens M Melenk. The partition of unity method. *International Journal for Numerical Methods in Engineering*, 40(4):727–758, 1997.
- [9] Subhajit Banerjee and N Sukumar. Exact integration scheme for planewave-enriched partition of unity finite element method to solve the Helmholtz problem. *Computer Methods in Applied Mechanics and Engineering*, 317:619–648, 2017.
- [10] Gang Bao and Jun Lai. Radar cross section reduction of a cavity in the ground plane:

TE polarization. *Discrete & Continuous Dynamical Systems-S*, 8(3):419, 2014.

- [11] Alvin Bayliss, Max Gunzburger, and Eli Turkel. Boundary conditions for the numerical solution of elliptic equations in exterior regions. *SIAM Journal on Applied Mathematics*, 42(2):430–451, 1982.
- [12] Y. Bazilevs, V.M. Calo, T.J.R. Hughes, and Y. Zhang. Isogeometric fluid-structure interaction: theory, algorithms, and computations. *Computational Mechanics*, 43(1):3–37, 2008.
- [13] Y. Bazilevs, V.M. Calo, Y. Zhang, and T.J.R. Hughes. Isogeometric fluid–structure interaction analysis with applications to arterial blood flow. *Computational Mechanics*, 38(4-5):310–322, 2006.
- [14] Y. Bazilevs, M.-C. Hsu, and M.A. Scott. Isogeometric fluid–structure interaction analysis with emphasis on non-matching discretizations, and with application to wind turbines. *Computer Methods in Applied Mechanics and Engineering*, 249:28–41, 2012.
- [15] Gernot Beer, Stéphane Bordas, et al. *Isogeometric Methods for Numerical Simulation*, volume 240. Springer, 2015.
- [16] David J Benson, Yuri Bazilevs, Emmanuel De Luycker, M-C Hsu, M Scott, TJR Hughes, and Ted Belytschko. A generalized finite element formulation for arbitrary basis functions: from isogeometric analysis to XFEM. *International Journal for Numerical Methods in Engineering*, 83(6):765–785, 2010.
- [17] D.J. Benson, Y. Bazilevs, M.-C. Hsu, and T.J.R. Hughes. Isogeometric shell analysis: the Reissner–Mindlin shell. *Computer Methods in Applied Mechanics and Engineering*, 199(5-8):276–289, 2010.
- [18] LM Bernal, Victor M Calo, Nathan Collier, GA Espinosa, F Fuentes, and JC Mahecha. Isogeometric analysis of hyperelastic materials using PetIGA. *Procedia Computer Science*, 2013.
- [19] P. Bettess, O. Laghrouche, E. Perrey-Debain, E. Perrey-Debain, O. Laghrouche, P. Bettess, and J. Trevelyan. Plane-wave basis finite elements and boundary elements for three-dimensional wave scattering. *Philosophical Transactions of the Royal Society of London. Series A: Mathematical, Physical and Engineering Sciences*, 362(1816):561–577, 2004.
- [20] A. Buffa, G. Sangalli, and R. Vázquez. Isogeometric analysis in electromagnetics: B-splines approximation. *Computer Methods in Applied Mechanics and Engineering*, 199(17):1143 – 1152, 2010.
- [21] Annalisa Buffa and Rafael Vázquez. Isogeometric analysis for electromagnetic scattering problems. In *2014 International Conference on Numerical Electromagnetic Modeling and Optimization for RF, Microwave, and Terahertz Applications (NEMO)*, pages 1–3. IEEE, 2014.

- [22] Hadrien Bériot, Albert Prinn, and Gwénaél Gabard. Efficient implementation of high-order finite elements for Helmholtz problems. *International Journal for Numerical Methods in Engineering*, 106(3):213–240, 2016.
- [23] L.L. Chen, H. Lian, Z. Liu, H.B. Chen, E. Atroshchenko, and S.P.A. Bordas. Structural shape optimization of three dimensional acoustic problems with isogeometric boundary element methods. *Computer Methods in Applied Mechanics and Engineering*, 355:926 – 951, 2019.
- [24] K. Christodoulou, O. Laghrouche, M.S. Mohamed, and J. Trevelyan. High-order finite elements for the solution of Helmholtz problems. *Computers & Structures*, 191:129 – 139, 2017.
- [25] L. Coox, E. Deckers, D. Vandepitte, and W. Desmet. A performance study of NURBS-based isogeometric analysis for interior two-dimensional time-harmonic acoustics. *Computer Methods in Applied Mechanics and Engineering*, 305(Supplement C):441 – 467, 2016.
- [26] J Austin Cottrell, Thomas JR Hughes, and Yuri Bazilevs. *Isogeometric analysis: toward integration of CAD and FEA*. John Wiley & Sons, 2009.
- [27] J.A. Cottrell, A. Reali, Y. Bazilevs, and T.J.R. Hughes. Isogeometric analysis of structural vibrations. *Computer Methods in Applied Mechanics and Engineering*, 195(41-43):5257–5296, 2006.
- [28] L Beirao da Veiga, C Lovadina, and A Reali. Avoiding shear locking for the Timoshenko beam problem via isogeometric collocation methods. *Computer Methods in Applied Mechanics and Engineering*, 241:38–51, 2012.
- [29] E. De Luycker, D.J. Benson, T. Belytschko, Y. Bazilevs, and M.C. Hsu. X-FEM in isogeometric analysis for linear fracture mechanics. *International Journal for Numerical Methods in Engineering*, 87(6):541–565, 2011.
- [30] M. Dinachandra and Sethuraman Raju. Plane wave enriched Partition of Unity Isogeometric Analysis (PUIGA) for 2D-Helmholtz problems. *Computer Methods in Applied Mechanics and Engineering*, 335:380 – 402, 2018.
- [31] Ganesh C. Diwan and M. Shadi Mohamed. Pollution studies for high order isogeometric analysis and finite element for acoustic problems. *Computer Methods in Applied Mechanics and Engineering*, 350:701 – 718, 2019.
- [32] M. Droliá, M.S. Mohamed, O. Laghrouche, M. Seaid, and J. Trevelyan. Enriched finite elements for initial-value problem of transverse electromagnetic waves in time domain. *Computers & Structures*, 182:354 – 367, 2017.
- [33] A. El Kacimi and O. Laghrouche. Improvement of pufem for the numerical solution of high-frequency elastic wave scattering on unstructured triangular mesh grids. *International Journal for Numerical Methods in Engineering*, 84(3):330–350, 2010.

- [34] T. Elguedj and T.J.R. Hughes. Isogeometric analysis of nearly incompressible large strain plasticity. *Computer Methods in Applied Mechanics and Engineering*, 268:388–416, 2014.
- [35] Mathias Fink, Gabriel Montaldo, and Mickael Tanter. Time-reversal acoustics in biomedical engineering. *Annual review of biomedical engineering*, 5(1):465–497, 2003.
- [36] S. Sh Ghorashi, N. Valizadeh, S. Mohammadi, and Timon Rabczuk. Extended isogeometric analysis of plates with curved cracks. In *Civil-Comp Proceedings*, volume 100, 12 2012.
- [37] S.Sh. Ghorashi, N. Valizadeh, and S. Mohammadi. Extended isogeometric analysis for simulation of stationary and propagating cracks. *International Journal for Numerical Methods in Engineering*, 89(9):1069–1101, 2012.
- [38] Hector Gomez and Laura De Lorenzis. The variational collocation method. *Computer Methods in Applied Mechanics and Engineering*, 309:152–181, 2016.
- [39] Behrooz Hassani, S Mehdi Tavakkoli, and NZ Moghadam. Application of isogeometric analysis in structural shape optimization. *Scientia Iranica*, 18(4):846–852, 2011.
- [40] Austin J Herrema, Josef Kiendl, and Ming-Chen Hsu. A framework for isogeometric-analysis-based optimization of wind turbine blade structures. *Wind Energy*, 22(2):153–170, 2019.
- [41] Ralf Hiptmair, Andrea Moiola, and Ilaria Perugia. A Survey of Trefftz Methods for the Helmholtz Equation. In Gabriel R. Barrenechea, Franco Brezzi, Andrea Cangiani, and Emmanuil H. Georgoulis, editors, *Building Bridges: Connections and Challenges in Modern Approaches to Numerical Partial Differential Equations*, pages 237–279. Springer International Publishing, Cham, 2016.
- [42] Thomas JR Hughes, John A Cottrell, and Yuri Bazilevs. Isogeometric analysis: CAD, finite elements, NURBS, exact geometry and mesh refinement. *Computer Methods in Applied Mechanics and Engineering*, 194(39):4135–4195, 2005.
- [43] F. Ihlenburg and I.M. Babuška. Finite Element Solution of the Helmholtz Equation with High Wave Number Part I: The h-Version of the FEM. *Computers & Mathematics with Applications*, 30(9):9 – 37, 1995.
- [44] F. Ihlenburg and I.M. Babuška. Finite Element Solution of the Helmholtz Equation with High Wave Number Part II: The h-p Version of the FEM. *SIAM Journal on Numerical Analysis*, 34(1):315 – 358, 1997.
- [45] Yue Jia, Cosmin Anitescu, Yongjie Jessica Zhang, and Timon Rabczuk. An adaptive isogeometric analysis collocation method with a recovery-based error estimator. *Computer Methods in Applied Mechanics and Engineering*, 345:52–74, 2019.
- [46] Richard W. Johnson. Higher order B-spline collocation at the Greville abscissae. *Applied Numerical Mathematics*, 52(1):63 – 75, 2005.

- [47] A. El Kacimi, O. Laghrouche, M.S. Mohamed, and J. Trevelyan. Bernstein–bézier based finite elements for efficient solution of short wave problems. *Computer Methods in Applied Mechanics and Engineering*, 343:166 – 185, 2019.
- [48] Tahsin Khajah, Xavier Antoine, and Stéphane PA Bordas. B-Spline FEM for Time-Harmonic Acoustic Scattering and Propagation. *Journal of Theoretical and Computational Acoustics*, page 1850059, 2019.
- [49] J Kiendl, F Auricchio, L Beirao da Veiga, C Lovadina, and A Reali. Isogeometric collocation methods for the Reissner–Mindlin plate problem. *Computer Methods in Applied Mechanics and Engineering*, 284:489–507, 2015.
- [50] J. Kiendl, K.-U. Bletzinger, J. Linhard, and R. Wüchner. Isogeometric shell analysis with Kirchhoff–Love elements. *Computer Methods in Applied Mechanics and Engineering*, 198(49-52):3902–3914, 2009.
- [51] J. Kiendl, M.-C. Hsu, Michael CH Wu, and A. Reali. Isogeometric Kirchhoff–Love shell formulations for general hyperelastic materials. *Computer Methods in Applied Mechanics and Engineering*, 291:280–303, 2015.
- [52] Alice Lieu, Gwénaél Gabard, and Hadrien Bériot. A comparison of high-order polynomial and wave-based methods for Helmholtz problems. *Journal of Computational Physics*, 321:105 – 125, 2016.
- [53] Hongwei Lin, Qianqian Hu, and Yunyang Xiong. Consistency and convergence properties of the isogeometric collocation method. *Computer Methods in Applied Mechanics and Engineering*, 267:471–486, 2013.
- [54] M.S. Mahmood, O. Laghrouche, J. Trevelyan, and A. El Kacimi. Implementation and computational aspects of a 3D elastic wave modelling by PUFEM. *Applied Mathematical Modelling*, 49:568 – 586, 2017.
- [55] M. Medvinsky and E. Turkel. On surface radiation conditions for an ellipse. *Journal of Computational and Applied Mathematics*, 234(6):1647 – 1655, 2010. Eighth International Conference on Mathematical and Numerical Aspects of Waves (Waves 2007).
- [56] J.M. Melenk and I.M. Babuška. The partition of unity finite element method: basic theory and applications. *Computer Methods in Applied Mechanics and Engineering*, 139(1-4):289–314, 1996.
- [57] MS Mohamed, O Laghrouche, and A El-Kacimi. Some numerical aspects of the PUFEM for efficient solution of 2D Helmholtz problems. *Computers & Structures*, 88(23-24):1484–1491, 2010.
- [58] Monica Montardini, Giancarlo Sangalli, and Lorenzo Tamellini. Optimal-order isogeometric collocation at Galerkin superconvergent points. *Computer Methods in Applied Mechanics and Engineering*, 316:741–757, 2017.
- [59] Nicolas Moës, John Dolbow, and Ted Belytschko. A finite element method for crack

- growth without remeshing. *International Journal for Numerical Methods in Engineering*, 46(1):131–150, 1999.
- [60] Vinh Phu Nguyen, Cosmin Anitescu, Stéphane PA Bordas, and Timon Rabczuk. Isogeometric analysis: an overview and computer implementation aspects. *Mathematics and Computers in Simulation*, 117:89–116, 2015.
- [61] Nhon Nguyen-Thanh, Weidong Li, Jiazhao Huang, Narasimalu Srikanth, and Kun Zhou. An adaptive isogeometric analysis meshfree collocation method for elasticity and frictional contact problems. *International Journal for Numerical Methods in Engineering*, 6 2019.
- [62] Michael J Peake, Jon Trevelyan, and Graham Coates. Extended isogeometric boundary element method (XIBEM) for two-dimensional Helmholtz problems. *Computer Methods in Applied Mechanics and Engineering*, 259:93–102, 2013.
- [63] MJ Peake, J Trevelyan, and G Coates. Extended isogeometric boundary element method (XIBEM) for three-dimensional medium-wave acoustic scattering problems. *Computer Methods in Applied Mechanics and Engineering*, 284:762–780, 2015.
- [64] Xuan Peng, Elena Atroshchenko, Pierre Kerfriden, and SPA Bordas. Isogeometric boundary element methods for three dimensional static fracture and fatigue crack growth. *Computer Methods in Applied Mechanics and Engineering*, 316:151–185, 2017.
- [65] Les Piegl and Wayne Tiller. *The NURBS book*. Springer Science & Business Media, 2012.
- [66] A. Reali. An isogeometric analysis approach for the study of structural vibrations. *Journal of Earthquake Engineering*, 10(spec01):1–30, 2006.
- [67] Alessandro Reali and Hector Gomez. An isogeometric collocation approach for Bernoulli–Euler beams and Kirchhoff plates. *Computer Methods in Applied Mechanics and Engineering*, 284:623–636, 2015.
- [68] Dominik Schillinger, Michael J. Borden, and Henryk K. Stolarski. Isogeometric collocation for phase-field fracture models. *Computer Methods in Applied Mechanics and Engineering*, 284:583 – 610, 2015. Isogeometric Analysis Special Issue.
- [69] Dominik Schillinger, John A Evans, Alessandro Reali, Michael A Scott, and Thomas JR Hughes. Isogeometric collocation: Cost comparison with Galerkin methods and extension to adaptive hierarchical NURBS discretizations. *Computer Methods in Applied Mechanics and Engineering*, 267:170–232, 2013.
- [70] Steven H Schot. Eighty years of Sommerfeld’s radiation condition. *Historia Mathematica*, 19(4):385 – 401, 1992.
- [71] Yu-Deok Seo, Hyun-Jung Kim, and Sung-Kie Youn. Shape optimization and its extension to topological design based on isogeometric analysis. *International Journal of Solids and Structures*, 47(11-12):1618–1640, 2010.

- [72] S. Shojaee, E. Izadpanah, N. Valizadeh, and J. Kiendl. Free vibration analysis of thin plates by using a NURBS-based isogeometric approach. *Finite Elements in Analysis and Design*, 61:23–34, 2012.
- [73] R.N. Simpson, M.A. Scott, M. Taus, D.C. Thomas, and H. Lian. Acoustic isogeometric boundary element analysis. *Computer Methods in Applied Mechanics and Engineering*, 269:265 – 290, 2014.
- [74] Theofanis Strouboulis, Ivo Babuška, and Realino Hidajat. The generalized finite element method for Helmholtz equation: theory, computation, and open problems. *Computer Methods in Applied Mechanics and Engineering*, 195(37-40):4711–4731, 2006.
- [75] Theofanis Strouboulis, Realino Hidajat, and Ivo Babuška. The generalized finite element method for Helmholtz equation. Part II: Effect of choice of handbook functions, error due to absorbing boundary conditions and its assessment. *Computer Methods in Applied Mechanics and Engineering*, 197(5):364–380, 2008.
- [76] Yi Sun, Jon Trevelyan, Gabriel Hattori, and Chihua Lu. Discontinuous isogeometric boundary element (IGABEM) formulations in 3D automotive acoustics. *Engineering Analysis with Boundary Elements*, 105:303 – 311, 2019.
- [77] J. Videla, F. Contreras, H.X. Nguyen, and E. Atroshchenko. Application of PHT-splines in bending and vibration analysis of cracked Kirchhoff-Love Plates. *Computer Methods in Applied Mechanics and Engineering*, in press.
- [78] Javier Videla, Cosmin Anitescu, Tahsin Khajah, Stéphane P.A. Bordas, and Elena Atroshchenko. h- and p-adaptivity driven by recovery and residual-based error estimators for PHT-splines applied to time-harmonic acoustics. *Computers & Mathematics with Applications*, 77(9):2369 – 2395, 2019.
- [79] Vianey Villamizar, Sebastian Acosta, and Blake Dastrup. High order local absorbing boundary conditions for acoustic waves in terms of farfield expansions. *Journal of Computational Physics*, 333:331–351, 2017.
- [80] Wolfgang A Wall, Moritz A Frenzel, and Christian Cyron. Isogeometric structural shape optimization. *Computer Methods in Applied Mechanics and Engineering*, 197(33-40):2976–2988, 2008.
- [81] H. Wu, W. Ye, and W. Jiang. Isogeometric finite element analysis of interior acoustic problems. *Applied Acoustics*, 100(Supplement C):63 – 73, 2015.
- [82] P. Yu, C. Anitescu, S. Tomar, S.P.A. Bordas, and P. Kerfriden. Adaptive isogeometric analysis for plate vibrations: An efficient approach of local refinement based on hierarchical a posteriori error estimation. *Computer Methods in Applied Mechanics and Engineering*, 342:251–286, 2018.
- [83] Xiangkui Zhang, Chunning Jin, Ping Hu, Xuefeng Zhu, Wenbin Hou, Jinting Xu, Changsheng Wang, Yuewei Zhang, Zheng-Dong Ma, and Holly Smith. NURBS modeling and isogeometric shell analysis for complex tubular engineering structures. *Computatio-*



*nal and Applied Mathematics*, 36(4):1659–1679, 2017.

- [84] Olgierd Cecil Zienkiewicz and Jian Zhong Zhu. The superconvergent patch recovery and a posteriori error estimates. part 1: The recovery technique. *International Journal for Numerical Methods in Engineering*, 33(7):1331–1364, 1992.
- [85] Olgierd Cecil Zienkiewicz and Jian Zhong Zhu. The superconvergent patch recovery and a posteriori error estimates. part 2: Error estimates and adaptivity. *International Journal for Numerical Methods in Engineering*, 33(7):1365–1382, 1992.

# Appendix A

## Geometry Parameterization employed in the Numerical Examples

Patch	Knot Vector		Control Points		
	U	V	x	y	w
1	[0,0,1,1]	[0,0,1,1]	-1.0000	-1.0000	1.0000
			1.0000	-1.0000	1.0000
			1.0000	1.0000	1.0000
			-1.0000	1.0000	1.0000

Table A.1: Geometry Information for the duct domain

Patch	Knot Vector		Control Points		
	U	V	x	y	w
1	[0,0,1,1]	[0,0,1,1]	0.0000	2.0000	1.0000
			2.0000	0.0000	1.0000
			2.0000	1.0000	1.0000
			0.0000	1.0000	1.0000

Table A.2: Geometry Information for the duct domain

Patch	Knot Vector		Control Points		
	U	V	x	y	w
1	[0,0,1,1]	[0,0,0,1,1,1]	$r$	0	1
			$r\frac{\sqrt{2}}{2}$	$r\frac{\sqrt{2}}{2}$	$\frac{\sqrt{2}}{2}$
			0	$r$	1
			$R$	0	1
			$R\frac{\sqrt{2}}{2}$	$R\frac{\sqrt{2}}{2}$	$\frac{\sqrt{2}}{2}$
			0	$R$	1
2	[0,0,1,1]	[0,0,0,1,1,1]	0	$r$	1
			$-r\frac{\sqrt{2}}{2}$	$r\frac{\sqrt{2}}{2}$	$\frac{\sqrt{2}}{2}$
			$-r$	0	1
			0	$R$	1
			$-R\frac{\sqrt{2}}{2}$	$R\frac{\sqrt{2}}{2}$	$\frac{\sqrt{2}}{2}$
			$-R$	0	1
3	[0,0,1,1]	[0,0,0,1,1,1]	$r$	0	1
			$-r\frac{\sqrt{2}}{2}$	$-r\frac{\sqrt{2}}{2}$	$\frac{\sqrt{2}}{2}$
			0	$-r$	1
			$-R$	0	1
			$-R\frac{\sqrt{2}}{2}$	$-R\frac{\sqrt{2}}{2}$	$\frac{\sqrt{2}}{2}$
			0	$-R$	1
4	[0,0,1,1]	[0,0,0,1,1,1]	0	$-r$	1
			$r\frac{\sqrt{2}}{2}$	$-r\frac{\sqrt{2}}{2}$	$\frac{\sqrt{2}}{2}$
			$r$	0	1
			0	$-R$	1
			$R\frac{\sqrt{2}}{2}$	$-R\frac{\sqrt{2}}{2}$	$\frac{\sqrt{2}}{2}$
			$R$	0	1

Table A.3: Geometry Information for the annular geometry

Patch	Knot Vector		Control Points		
	U	V	x	y	w
1	[0,0,1,1]	[0,0,0,1,1,1]	2.8532	0.9271	1.0000
			4.7553	1.5451	1.0000
			1.0000	1.0000	1.0000
			3.6327	5.0000	0.8090
			0.0000	3.0000	1.0000
			0.0000	5.0000	1.0000
2	[0,0,1,1]	[0,0,0,1,1,1]	0.0000	3.0000	1.0000
			0.0000	5.0000	1.0000
			-1.0000	1.0000	1.0000
			-3.6327	5.0000	0.8090
			-2.8532	0.9271	1.0000
			-4.7553	1.5451	1.0000
3	[0,0,1,1]	[0,0,0,1,1,1]	-2.8532	0.9271	1.0000
			-4.7553	1.5451	1.0000
			-1.3450	-0.4370	1.0000
			-5.8779	-1.9098	0.8090
			-1.7634	-2.4271	1.0000
			-2.9389	-4.0451	1.0000
4	[0,0,1,1]	[0,0,0,1,1,1]	-1.7634	-2.4271	1.0000
			-2.9389	-4.0451	1.0000
			0.0000	-1.4142	1.0000
			0.0000	-6.1803	0.8090
			1.7634	-2.4271	1.0000
			2.9389	-4.0451	1.0000
5	[0,0,1,1]	[0,0,0,1,1,1]	1.7634	-2.4271	1.0000
			2.9389	-4.0451	1.0000
			1.3450	-0.4370	1.0000
			5.8779	-1.9098	0.8090
			2.8532	0.9271	1.0000
			4.7553	1.5451	1.0000

Table A.4: Geometry Information for the Star-shaped problem